DEGRADATION MECHANISM OF PEROVSKITE SOLAR CELLS

BY

Ryan Taoran Wang, B.Eng.

A Thesis Submitted to the Department of Materials Science and Engineering and the School of Graduate Studies of McMaster University in Partial Fulfilment of the Requirements for the Degree of Doctor of Philosophy.

Doctor of Philosophy (2020) **McMaster University**

(Materials Science and Engineering) **Hamilton, Ontario, Canada**

TITLE: **Degradation mechanism of Perovskite Solar Cells**

AUTHOR: **Ryan Taoran Wang, B.Eng.**

SUPERVISOR: **Prof. Gu Xu, Ph.D., FCAE, P.Eng.**

NUMBER OF PAGES: xiv, 142

Abstract

The perovskite solar cells have attracted much attention recently due to their low fabrication cost and high power conversion efficiency. However, the instability of such devices remained a serious challenge, which is yet to be resolved despite many attempts. In this thesis, the moisture degradation mechanism has been uncovered. It was found that the perovskite structure can be reconstructed when annealed at around 90°C, which leads to a reversible device of a much higher device lifetime. Following the experimental explorations, modelling work has also been conducted to simulate the water diffusion during the degradation and recovery. It was found that the moisture diffusion was initiated at the surface imperfection, where the activation energy for diffusion can be reduced. Based on these discoveries, a fresh structural negotiation method has been proposed to obtain a stable $FAPbI_3$ phase of a suitable bandgap for photovoltaics, which showed a reduced Gibbs free energy of 0.12eV compared with the δ phase. In addition, the activation energy for such phase transition was calculated to be 0.45eV, meaning that the discovered phase is protected by both thermodynamics and kinetics. All this opens an unprecedented avenue in perovskite research, which will hopefully be of intrinsic interest to the broad materials research community as well.

Declaration of Academic Achievements

The major research results during my Ph.D. study (from Sep. 2018 to Aug. 2021) have been published or submitted to peer reviewed journals, which are listed as follows:

As first/co-first author:

1. **Wang, R. T.**, Xu, A. F., Li, W., Li, Y., & Xu, G. (2021). Moisture-Stable FAPbI3 Perovskite Achieved by Atomic Structure Negotiation. The Journal of Physical Chemistry Letters, 12, 5332-5338.

2. **Wang, R.T.**, et al. "Magnetic-field-induced energy bandgap reduction of perovskite KMnF3." Journal of Materials Chemistry C (2020).

3. Xu, K. J. and **Wang, R. T.** (co-first author with the summer student), et al. (2020). Hysteresis and Instability Predicted in Moisture Degradation of Perovskite Solar Cells. ACS Applied Materials & Interfaces, 12(43), 48882-48889.

4. **Wang, R.T.**, et al. "Achieving Nonenzymatic Blood Glucose Sensing by Uprooting Saturation." Analytical Chemistry 92.15 (2020): 10777-10782.

5. **Wang, R.T.**, et al. "Ethylammonium Lead Iodide Formation in MAPbI3 Precursor Solutions by DMF Decomposition and Organic Cation Exchange Reaction." Crystals 10.3 (2020): 162.

6. **Wang, R. T.**, Xu, A. F., Chen, J. Y., Yang, L. W., Xu, G., Jarvis, V., & Britten, J. F. (2019). Reversing Organic–Inorganic Hybrid Perovskite Degradation in Water via pH and Hydrogen Bonds. The journal of physical chemistry letters, 10(22), 7245-7250.

7. **Wang, R.T.**, Tai, E.G., Chen, J.Y., Xu, G., LaPierre, R., Goktas, N.I. and Hu, N., 2019. A KMnF3 perovskite structure with improved stability, low bandgap and high transport

properties. Ceramics International, 45(1), pp.64-68.

As co-author:

8. Xu, A. F., **Wang, R. T.**, Yang, L. W., Liu, E. E., & Xu, G. (2020). An Environmentally Stable Organic–Inorganic Hybrid Perovskite Containing Py Cation with Low Trap-State Density. Crystals, 10(4), 272.

9. Xu, A.F., **Wang, R.T.**, Yang, L.W., Jarvis, V., Britten, J.F. and Xu, G., 2019. Pyrrolidinium lead iodide from crystallography: a new perovskite with low bandgap and good water resistance. Chemical Communications, 55(22), pp.3251-3253.

10. Xu, A. F., Wang, R. T., Yang, L. W., Liu, N., Chen, Q., LaPierre, R., ... & Xu, G. (2019). Pyrrolidinium containing perovskites with thermal stability and water resistance for photovoltaics. Journal of Materials Chemistry C, 7(36), 11104-11108.

11. Tai, E.G., **Wang, R.T.**, Chen, J.Y. and Xu, G., 2019. A Water-Stable Organic-Inorganic Hybrid Perovskite for Solar Cells by Inorganic Passivation. Crystals, 9(2), p.83.

12. Chen, J.Y., Zhou, Q., Xu, G., **Wang, R.T.**, Tai, E.G., Xie, L., Zhang, Q., Guan, Y. and Huang, X., 2019. Non-invasive blood glucose measurement of 95% certainty by pressure regulated Mid-IR. Talanta, 197, pp.211-217.

13. Zhou, J., Roshanmanesh, S., Hayati, F., Junior, V.J., **Wang, T.**, Hajiabady, S., Li, X.Y., Basoalto, H., Dong, H. and Papaelias, M., 2017. Improving the reliability of industrial multi-MW wind turbines. Insight-Non-Destructive Testing and Condition Monitoring, 59(4), pp.189-195.

Acknowledgement

First, I would like to express my gratitude to my supervisor, Prof. Gu Xu, for his constant training and guiding in my academic research, without which I cannot possibly achieve what I have achieved today. I really appreciate Prof. Gu Xu for offering me the chance to transfer from M.A.Sc. to Ph.D. degree at McMaster University. During the past few years, I received countless help from Prof. Gu Xu in both research and personal life. I have grown from a naive undergraduate to a much more sophisticated person all thanks to him, which is definitely a valuable experience.

I would also like to thank my supervisory committee member: Prof. Joey Kish and Prof. Adrian Kitai. Thank you for making sure I was on the right track and giving me valuable advice to my research topics. I would like to acknowledge our co-authors and collaborators, Dr. Nan-Xing Hu from Xerox Research Center of Canada, Prof. Yuning Li from University of Waterloo, Victoria Jarvis from McMaster Analytical X-Ray Diffraction Lab and Travis Casagrande from Canadian Center for Electron Microscopy, for their help, guidance, and experimental support. I really appreciate Dr. James Britten from MAX Diffraction Facility at McMaster University for his constant support and insightful discussion on single crystal XRD and time-resolved XRD techniques.

I am grateful for everyday life and discussion on academics with my colleagues, including Alex Fan Xu, Jason Yuanzhe Chen, Edward Guangqing Tai, Weiwei Zhang, and Lory Wenjuan Yang. Last, I appreciate the unconditional love and support from my parents and many other friends.

Contents

List of Figures

List of Tables

Chapter 1 Introduction

1.1 Solar energy

The solar energy is one of the most abundant source of renewable energy, which is about 5.4×10^{24}J/year [1,2]. Such amount of energy is a hundred times larger than other known reserves of fossil fuels such as oil, coal, and gas combined, which are 6.3×10^{21}J, 5×10^{21}J, and 20×10^{21}J/year, respectively [1]. Solar cells are the most suitable devices for the direct transformation of sunlight into electric power [3], which is basically a PN junction, as shown in Fig. 1.1. Despite the availability of several solar devices, the cost of cell fabrication must be substantially reduced so that solar energy can become an economical competitor to oil, coal, or gas[4–8].
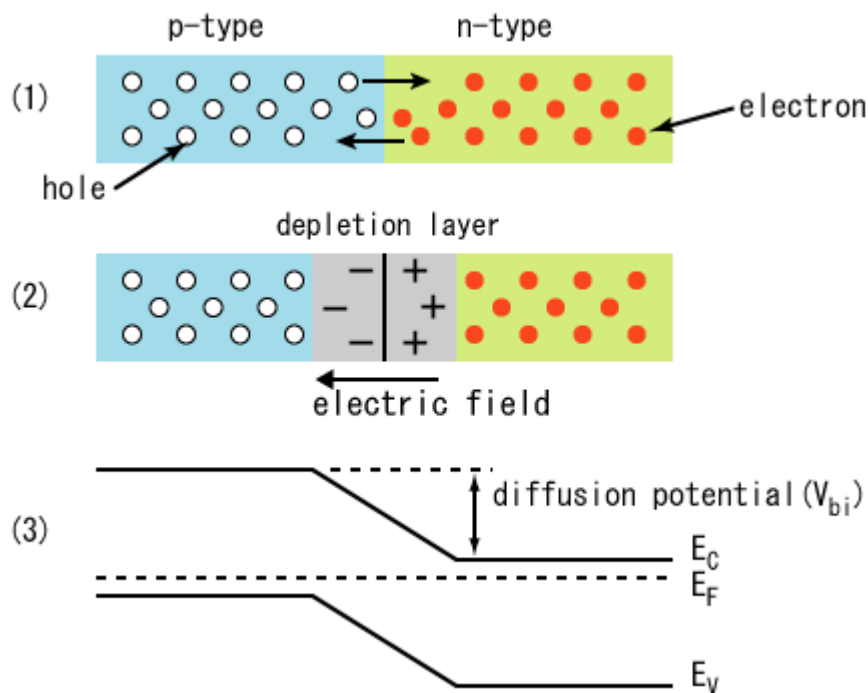
Figure 1. 1. PN junction structure.

1.2. Perovskite Solar Cell

Among all those solar cells, perovskite solar cells (PSCs) have attracted much attention

recently [9]. Perovskite, named after the Russian mineralogist Perovski, has a specific crystal structure with the same type of crystal structure as calcium titanium oxide [10], as shown in Fig. 1.2. And in PSC, the perovskite materials have an ABX_3 composition, where cation B is usually Pb or Sn [11], A is the organic/inorganic monovalent cations such as methylamine MA^+ ($CH_3NH_3^+$) and formamidinium FA^+ ($HC(NH_2)_2^+$) [12], and the X is the halide ion [13]. The $MAPbI_3$ perovskite solar cell was firstly reported in 2009 by Miyasaka et al, which showed a power conversion efficiency (PCE) of only 3.8% [14]. During the past decade, such efficiency has increased to over 25%, making them comparable to the commercially available Si solar panel, as shown by the NREL Best Research-Cell Efficiency Chart. Such remarkable performance was attributed to the magical characteristics of the perovskite structure, including favorable light absorption bandgap, long carrier lifetime and diffusion length, and low binding energy between the carriers [15].
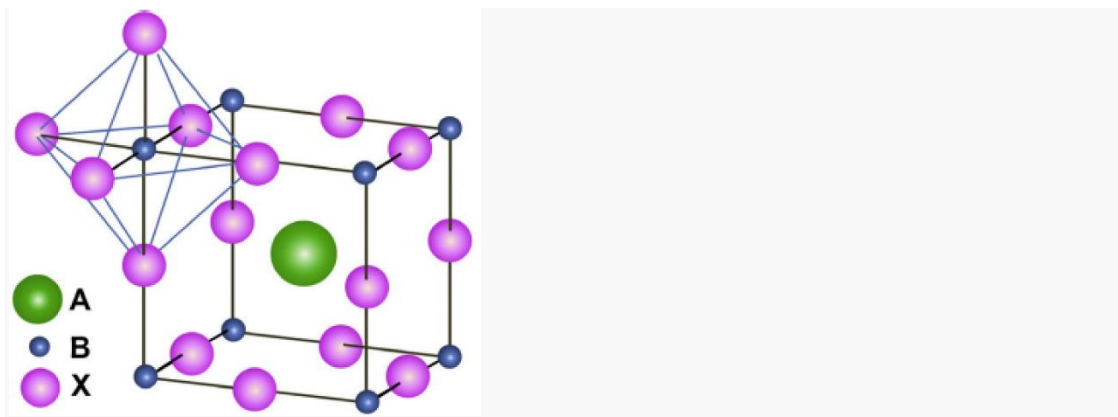
Figure 1. 2. Crystal structure of perovskite materials.
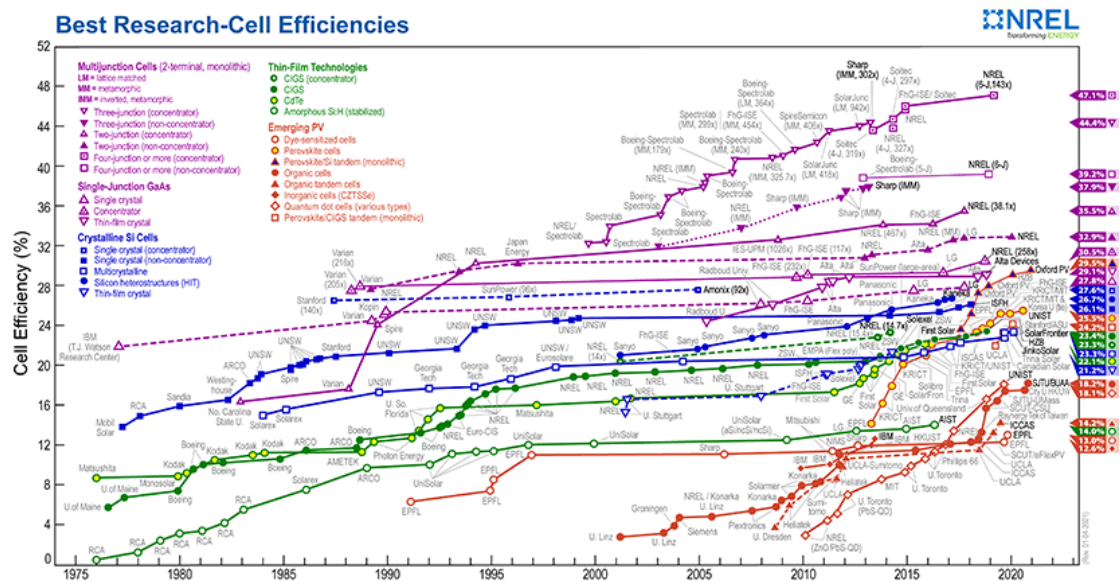
Figure 1. 3. Best Research-Cell Efficiency Chart produced by the NREL website [16].

The PSCs are constructed by several layers, which include cathode electrode (fluorinated tin oxide glass), electron transport layer (ETL), perovskite layer, hole transport layer (HTL), and metal anode (Au or Ag) [17]. The perovskite layer acts as the active layer to absorb sunlight and generate charge carriers. The ETL and HTL extract electrons and holes from perovskites, transporting them to the cathode and anode, which are connected with the external circuit.

The PSC device is commonly fabricated using two different structures, n–i–p structure and planar n–i–p structure [17,18], as shown in Figure 1.5. A typical n–i–p structure involves a fluorinated tin oxide (FTO) substrate, an ETL of mesoporous and compact titanium oxide (mesoporous-TiO_2, around 100–300 nm; compact-TiO_2, $\approx$20–50 nm), perovskite layer, then an HTL layer of several hundred nanometers (typically made of

Spiro-MeOTAD or PCBM), and finally the metal anode (Au or Ag, 50–100 nm). This structure was firstly reported by Grätzel et al in 2012, which then became a classic design [17]. An inverted p–i–n design has the opposite arrangement in the layer deposition sequence as opposed to the n–i–p structures. The HTL was deposited on the surface of the FTO substrate first, which was then followed by the perovskite layer and an ETL. Eventually, the anode was deposited on the ETL. Such a structure was proposed by Jeng et al in 2013, which showed a PCE of more than 20% [17,19].
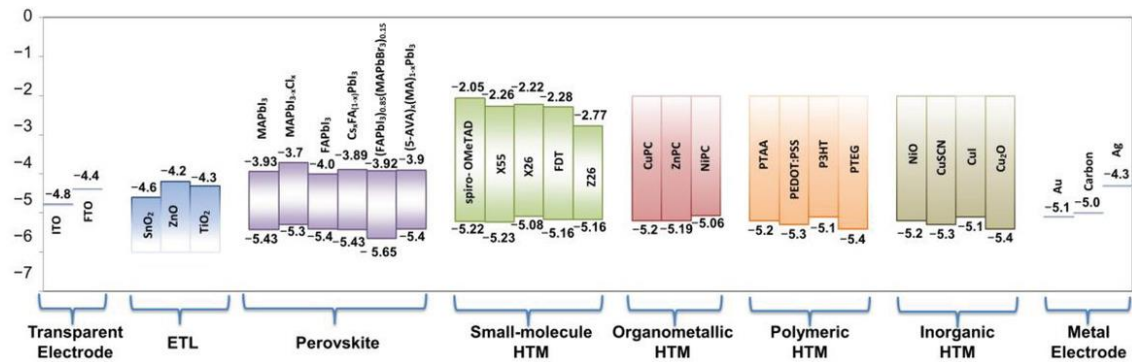
Figure 1. 4. Energy-level diagram of the PSC layers [17].
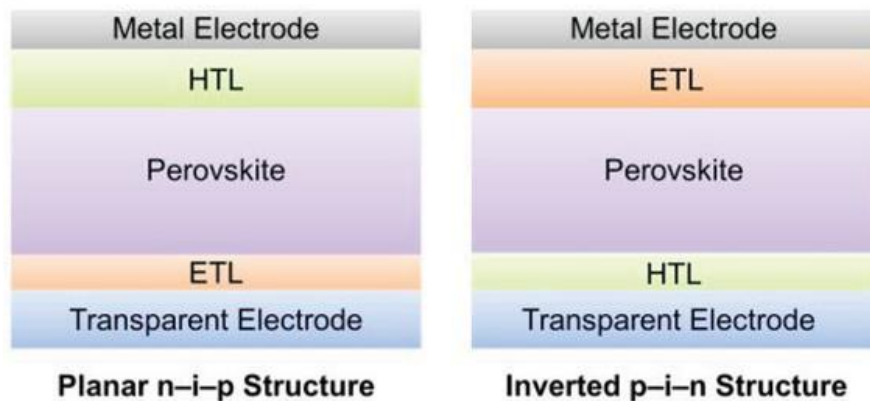
Figure 1. 5. PSC device structures [17].

The perovskite layer plays the most important role in the device performance, which is influenced significantly by the film morphology. Thus, $MAPbI_3$ and $FAPbI_3$ have been

commonly adopted as photovoltaic materials for large-scale perovskite films, due not only to the suitable bandgap, but also the ease of preparation and crystal growth [20,21]. These structures showed excellent optoelectronic properties, such as high absorption coefficient, wide absorption spectrum, high carrier concentration, and low exciton binding energy. Nowadays, the PCE of the PSCs based on those organic materials has been elevated to more than 25%, making them completely comparable to the commercial Si solar cells [22]. On the other hand, all-inorganic perovskite materials have attracted constant attention in recent years, as they demonstrated much better stability than the organic materials in the air. This perovskite family has a formula of $CsPbX_3$, where X represents halide ions. Compared with their organic counterparts, all-inorganic perovskite structure displayed a larger bandgap of around 2.7eV, making them a better choice for the application in tandem cells [19].

1.3 Degradation problem & previous attempts

The perovskite solar cells have experienced the instability problem since the first day of their birth. Due to the high reaction activity of the organic part, the lifetime of PSCs in the air is only a few hours without encapsulation. Even under the protection of pure N_2, such lifespan could only increase to several thousand hours, which made the instability issue one of the largest challenges in this field [12]. The pure inorganic counterparts, on the other hand, showed great stability in the air, the $CsPbI_3/CsPbBr_3$ perovskite could remain stable in the air for more than 2500 hours [23]. Unfortunately, they do not have a suitable bandgap at the working temperature, which is detrimental

5

to the efficiency. It is thus necessary to try to resolve the instability problem of the

organic perovskite.
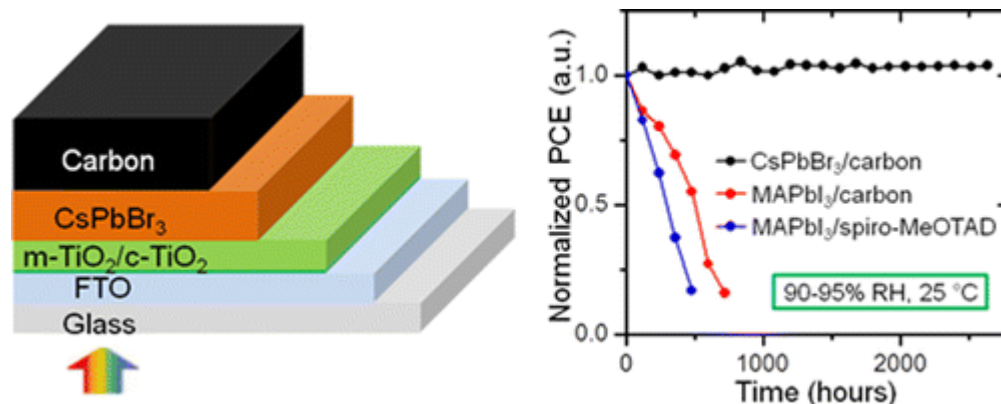
Figure 1. 6. The PSC device made of all inorganic perovskite, which exhibited much

better stability compared to the organic ones [23].
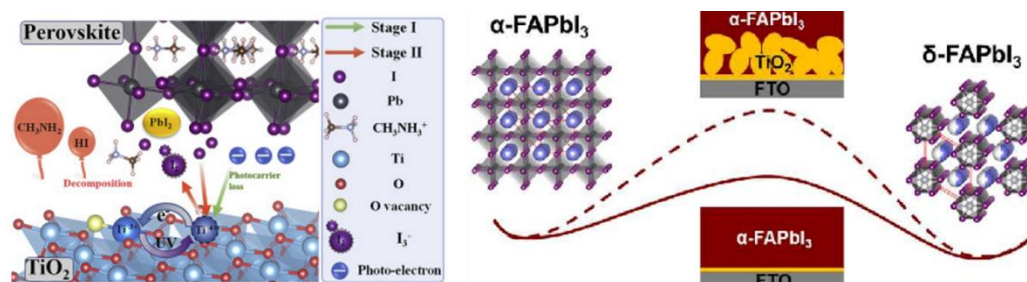
Figure 1. 7. The schematic illustration of the degradation of $MAPbI_3$ and phase

transition of $FAPbI_3$.

In order to enhance the stability of the organic-inorganic perovskite solar cells, a huge

amount of effect has been devoted to this field [24–26]. Researchers first tried to replace

the A site ions to stabilize the perovskite. Jin Lee et al. proposed the formula of

$FA_{0.9}Cs_{0.1}PbI_3$, which enhanced the stability of perovskite to several hundred hours,

leading to an average PCE of 16.5% [27]. Additionally, replacing the B site ions has also

been believed to be an alternative approach to enhance humidity stability. Nevertheless, limited enhancement has been achieved due to the ease of oxidation of other candidates, such as Sn [28].

In addition, interface engineering methods have also been investigated to optimize the device stability [12]. The HTL and ETL materials have attracted much attention [23–27,29–32]. Currently, Spiro-OMeTAD is the most successful HTL material, which decomposes very quickly in the air. Thus, extensive research has been conducted to replace it. Many alternatives have been discovered [23–27,29–34], including PEDOT: PSS, OMeTPA-FA, P3HT, PTAA, TBPC, and PYR17, etc., which showed better stability. Modifications at the ETL interface have also been studied. Zheng et al. have tried to insert NH_4I as a modifier into the TiO_2 ETL layer and the perovskite layer, resulting in a better perovskite film [35]. More importantly, the I^- provided by NH_4I could hinder the hydrolysis of perovskite, leading to a much-enhanced device lifetime of 700h at 80% relative humidity. SnO_2 has also been introduced to replace the TiO_2 as an ETL, which demonstrated higher electron mobility and better band alignment, ensuring a faster electron extraction [33,34]. Unfortunately, it is evident that those attempts are far from enough for the requirements of commercialization, which needs a lifetime of at least 10000 hours.

In fact, these attempts are destined to be less than successful, when the organic-inorganic perovskite structures are intrinsically reactive [13,36]. Thus, it is of great

significance to reveal the degradation mechanism so that better solutions can be proposed to eradicate the instability from the root. Despite a great amount of effort, the degradation mechanism, in particular, still remains a matter of much debate [37–40]. It has been found that the stability of MAPbI$_3$ can be affected by many environmental factors, such as temperature, oxygen level, UV light, and especially humid levels [15,41]. In the moisture, such structure could decompose into CH$_3$NH$_2$, CH$_3$NH$_2$, and PbI$_2$ [3], as shown in equation (1) and (2).

MAPbI$_3$ + H$_2$O → MAI + PbI$_2$ (equation 1)

MAI → CH$_3$NH$_2$ (g) + HI (g)   (equation 2)
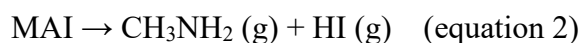
Others, however, believed that one water molecule is able to trigger a chain reaction and cause the collapse of the perovskite structure. In the follow-up study, some intermedia states of MAPbI$_3$ were also revealed, including CH$_3$NH$_3$PbI$_3$·H$_2$O and (CH$_3$NH$_3$)$_4$PbI$_6$·2H$_2$O, which was synthesized by adding water to the perovskite single crystals [30]. Interestingly, it was also discovered that the cell stability maximized at the humidity of 0% or 50%, which is counter-intuitive to what was discovered before [42]. Thus, Li et al conducted simulation work on the degradation mechanism using the first-principles method, which uncovered that the adsorption energy per water molecule would be enhanced from 0.3eV to 0.58eV after eight water molecules [3]. They believe this is caused by the H-bonding whose interaction is conducive, meaning that the hydrolysis process of the perovskite would be accelerated by the increasing number of water molecules adsorbed on the structure. Such a seemingly ideal explanation was,

however, soon declined by Ahn et al. (2016), who found that, $CH_3NH_3PbI_3$ would not irreversibly decompose in a humid environment, instead, it only decomposes with the presence of ions such as N^+ or H^- in the humid environment [40]. In addition, they assumed that N^+, H^- ions introduce a "local electric field" to distort the $CH_3NH_3PbI_3$ structure electrostatically. However, N^+ and H^- ions could hardly exist in water in reality, as they would react with water vigorously [43,44]. All this aggravates the controversy, making $CH_3NH_3PbI_3$ stability even more debatable.
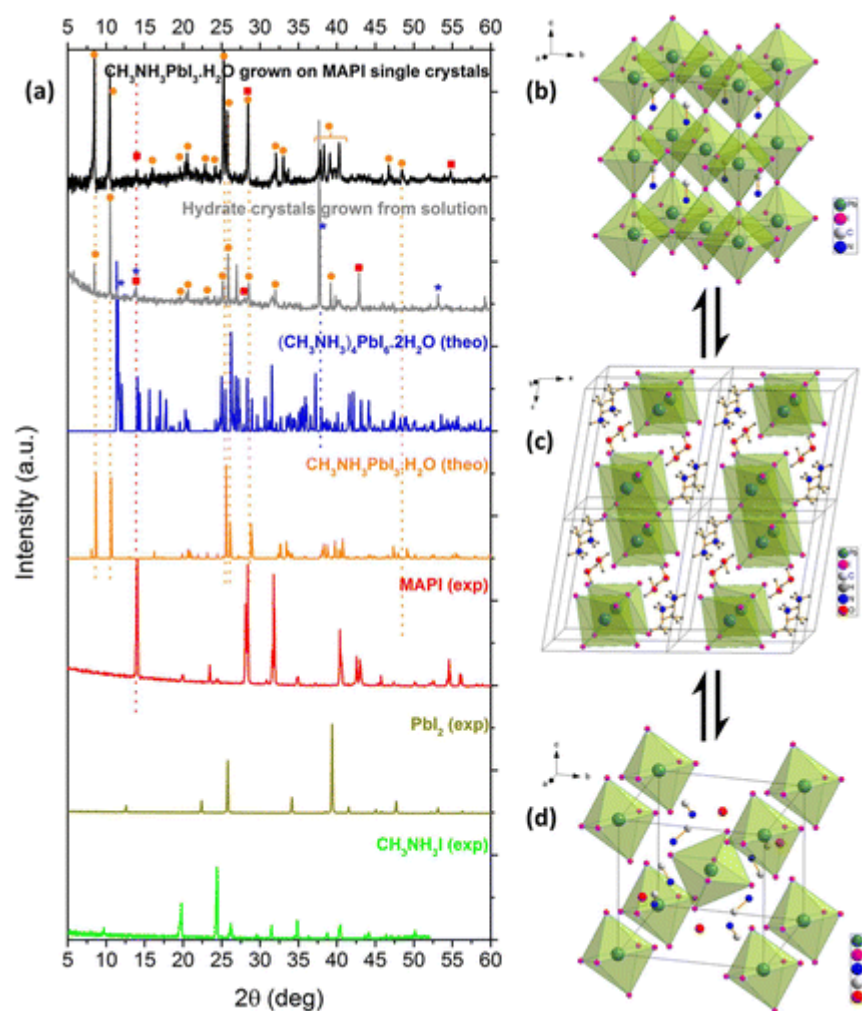
Figure 1. 8. (a) The XRD measurement that confirmed the formation of $CH_3NH_3PbI_3 \cdot H_2O$ and $(CH_3NH_3)_4PbI_6 \cdot 2H_2O$ (b) (c) & (d) indicated the unit cell of

9

these new phases and the transition process [30].

1.4 Our discoveries

It is, therefore, the purpose of this thesis to not only neutralize these conflicts, but also

advance the understanding of perovskite degradation. In chapter 2, it was reported that

hydrogen bonding between the A site organic ions and halides supported the perovskite

structure, which was destroyed when the water attacks the structure, causing the

breakdown. In particular, it is discovered that CH_3NH_3I formed after structure

breakdown showed limited degree of hydrolysis in water due to its ionic bonding energy.

The decomposition of $CH_3NH_3PbI_3$ was reversed by annealing at around 90 °C after

the decomposition. These discoveries on $MAPbI_3$ degradation inspired us to resolve the

phase transition challenge of $FAPbI_3$ in chapter 3. We proposed a totally opposite

strategy, more specifically, by embracing the moisture instead of eliminating it. Based

on our previous discovery of the hydrogen bond theory, it is discovered that $FAPbI_3$ is

capable of forming 3 intermolecular H-bonds, one of which can be replaced by the

water molecule to enhance the stability of the structure, as has been done in their

counterparts of $MAPbI_3$. Thus, a stable structure of a similar bandgap of α-$FAPbI_3$ is

synthesized by adding one water molecule to the perovskite unit cell. From the single

crystal measurements and thermodynamic/kinetics calculation, it has been revealed that

the internal strain of α-$FAPbI_3$, which was believed to be the root cause of the phase

transition, has been removed by the enlarged unit cell of the novel structure. In addition,

we also proposed a method to purify the $MAPbI_3$ during the synthesizing process in

chapter 4 by uncovering the mysterious impurities that have been widely reported. It was discovered that N, N-Dimethylformamide (DMF) would decompose at a higher temperature, which enabled the organic cation exchange reaction and lead to the formation of $CH_3CH_2NH_3I$ (EAI). Subsequently, EAI would react with PbI_2 to form $EAPbI_3$, leading to a compromised film morphology, which lowers the PCE. Next, we conducted the modelling work in chapter 5, which quantitatively simulated the diffusion process of water molecules to the perovskite structure. We revealed the kinetic details of the perovskite grain degradation and reconstruction under the influence of water molecule diffusion. It was found that the moisture diffusion is initiated at the surface imperfection, where the activation energy for diffusion was compensated by the surface energy. The structure recovery has to follow the reverse diffusion, which presents a non-linear diffusional profile, and is accompanied by hysteresis.

Additionally, we also tried to lower the bandgap of all-inorganic perovskite solar cells, which was believed to be the largest challenge of such devices. In chapter 6, a fresh all-inorganic perovskite structure was proposed based on the tolerance factor (t) and octahedral factor (μ) of the crystal structure, which is reported to be the golden standard to evaluate the perovskite stability and bandgap value. An optimal inorganic perovskite of reduced bandgap, $KMnF_3$, was developed and investigated, which presented great stability and a good bandgap of 1.7eV. The transport properties tests reveal surprisingly excellent carrier density and mobility. Following this work, we explored the magnetic response of $KMnF_3$ under the low to moderate magnetic field, which is shown in

chapter 7. We unexpectedly discovered that, under the presence of modest magnetic field strength of 0.4T, $KMnF_3$ perovskite exhibits both bandgap reduction from 1.77eV to 1.54eV as well as electrical conductivity enhancement by a factor of 10. Similar but less dramatic results were also obtained in other perovskites, such as $MAPbI_3$ and $CsPbBr_3$.

References

(1)   Musa, A.; Danyou, Y.; Ampaw, E. *Analysis of Solar Radiation Data in Northern Ghana*; LAP Lambert Academic, 2012.

(2)   Adaramola, M. S.; Agelin-Chaab, M.; Paul, S. S. Analysis of Hybrid Energy Systems for Application in Southern Ghana. *Energy Convers. Manag.* **2014**. https://doi.org/10.1016/j.enconman.2014.08.029.

(3)   Li, M.; Li, H.; Fu, J.; Liang, T.; Ma, W. Recent Progress on the Stability of Perovskite Solar Cells in a Humid Environment. *J. Phys. Chem. C* **2020**, *124* (50), 27251–27266.

(4)   Teodorescu, C. M.; Lungu, G. A. Band Ferromagnetism in Systems of Variable Dimensionality. *J. Optoelectron. Adv. Mater.* **2008**, *10* (11), 3058–3068.

(5)   Griffiths, D. J.; Reeves, A. Electrodynamics. *Introd. to Electrodyn. 3rd ed., Prentice Hall, Up. Saddle River, New Jersey* **2005**, *301*, 574–574.

(6)   Ajiki, H.; Ando, T. Electronic States of Carbon Nano Tubes. *J. Phys. Soc. Japan* **1993**, *62* (4), 1255–1266. https://doi.org/10.1143/JPSJ.62.1255.

(7)   Gulyamov, G.; Erkaboev, U. I.; Majidova, G. N.; Qosimova, M. O.; Davlatov, A.

B. New Method of Determining the Landau Levels in Narrow-Gap Semiconductors. *Open J. Appl. Sci.* **2015**, *05* (12), 771–775. https://doi.org/10.4236/ojapps.2015.512073.

(8)   Fedorov, G.; Barbara, P.; Smirnov, D.; Jiḿnez, D.; Roche, S. Tuning the Band Gap of Semiconducting Carbon Nanotube by an Axial Magnetic Field. *Appl. Phys. Lett.* **2010**, *96* (13), 132101. https://doi.org/10.1063/1.3360214.

(9)   Hardin, B. E.; Snaith, H. J.; McGehee, M. D. The Renaissance of Dye-Sensitized Solar Cells. *Nat. Photonics* **2012**, *6* (3), 162–169.

(10)   Wu, Z.; Bai, S.; Xiang, J.; Yuan, Z.; Yang, Y.; Cui, W.; Gao, X.; Liu, Z.; Jin, Y.; Sun, B. Efficient Planar Heterojunction Perovskite Solar Cells Employing Graphene Oxide as Hole Conductor. *Nanoscale* **2014**, *6* (18), 10505–10510.

(11)   Eperon, G. E.; Burlakov, V. M.; Docampo, P.; Goriely, A.; Snaith, H. J. Morphological Control for High Performance, Solution-processed Planar Heterojunction Perovskite Solar Cells. *Adv. Funct. Mater.* **2014**, *24* (1), 151–157.

(12)   Zhou, H.; Chen, Q.; Li, G.; Luo, S.; Song, T.; Duan, H.-S.; Hong, Z.; You, J.; Liu, Y.; Yang, Y. Interface Engineering of Highly Efficient Perovskite Solar Cells. *Science (80-.).* **2014**, *345* (6196), 542–546.

(13)   Wang, R. T.; Tai, E. G.; Chen, J. Y.; Xu, G.; LaPierre, R.; Goktas, N. I.; Hu, N. A KMnF3 Perovskite Structure with Improved Stability, Low Bandgap and High Transport Properties. *Ceram. Int.* **2019**, *45* (1), 64–68.

(14)   Kojima, A.; Teshima, K.; Shirai, Y.; Miyasaka, T. Organometal Halide Perovskites as Visible-Light Sensitizers for Photovoltaic Cells. *J. Am. Chem. Soc.*

2009, *131* (17), 6050–6051. https://doi.org/10.1021/ja809598r.

(15) Lee, M. M.; Teuscher, J.; Miyasaka, T.; Murakami, T. N.; Snaith, H. J. Efficient Hybrid Solar Cells Based on Meso-Superstructured Organometal Halide Perovskites. *Science (80-.).* **2012**, *338* (6107), 643–647.

(16) Yan, Y.; Lin, X.; Yang, S.; Blake, A. J.; Dailly, A.; Champness, N. R.; Hubberstey, P.; Schröder, M.; Koo, J. Y.; Yakiyama, Y.; et al. Best Research-Cell Efficiency Chart | Photovoltaic Research | NREL. *J. Am. Chem. Soc.* **2020**.

(17) Wang, F.; Cao, Y.; Chen, C.; Chen, Q.; Wu, X.; Li, X.; Qin, T.; Huang, W. Materials toward the Upscaling of Perovskite Solar Cells: Progress, Challenges, and Strategies. *Advanced Functional Materials*. 2018. https://doi.org/10.1002/adfm.201803753.

(18) Wang, P.; Wu, Y.; Cai, B.; Ma, Q.; Zheng, X.; Zhang, W. H. Solution-Processable Perovskite Solar Cells toward Commercialization: Progress and Challenges. *Advanced Functional Materials*. 2019. https://doi.org/10.1002/adfm.201807661.

(19) Tian, J.; Xue, Q.; Yao, Q.; Li, N.; Brabec, C. J.; Yip, H. L. Inorganic Halide Perovskite Solar Cells: Progress and Challenges. *Advanced Energy Materials*. 2020. https://doi.org/10.1002/aenm.202000183.

(20) Akman, E.; Shalan, A. E.; Sadegh, F.; Akin, S. Moisture-Resistant FAPbI3 Perovskite Solar Cell with 22.25 % Power Conversion Efficiency through Pentafluorobenzyl Phosphonic Acid Passivation. *ChemSusChem* **2021**, *14* (4), 1176–1183. https://doi.org/10.1002/cssc.202002707.

(21) Christians, J. A.; Miranda Herrera, P. A.; Kamat, P. V. Transformation of the

Excited State and Photovoltaic Efficiency of CH3NH3PbI3 Perovskite upon Controlled Exposure to Humidified Air. *J. Am. Chem. Soc.* **2015**. https://doi.org/10.1021/ja511132a.

(22) Niu, G.; Guo, X.; Wang, L. Review of Recent Progress in Chemical Stability of Perovskite Solar Cells. *J. Mater. Chem. A* **2015**. https://doi.org/10.1039/c4ta04994b.

(23) Liang, J.; Wang, C.; Wang, Y.; Xu, Z.; Lu, Z.; Ma, Y.; Zhu, H.; Hu, Y.; Xiao, C.; Yi, X. All-Inorganic Perovskite Solar Cells. *J. Am. Chem. Soc.* **2016**, *138* (49), 15829–15832.

(24) Hu, L.; Li, M.; Yang, K.; Xiong, Z.; Yang, B.; Wang, M.; Tang, X.; Zang, Z.; Liu, X.; Li, B. PEDOT: PSS Monolayers to Enhance the Hole Extraction and Stability of Perovskite Solar Cells. *J. Mater. Chem. A* **2018**, *6* (34), 16583–16589.

(25) Xu, K. J.; Wang, R. T.; Xu, A. F.; Chen, J. Y.; Xu, G. Hysteresis and Instability Predicted in Moisture Degradation of Perovskite Solar Cells. *ACS Appl. Mater. Interfaces* **2020**, *12* (43), 48882–48889.

(26) Wang, R. T.; Xu, A. F.; Yang, L. W.; Chen, J. Y.; Kitai, A.; Xu, G. Magnetic-Field-Induced Energy Bandgap Reduction of Perovskite KMnF 3. *J. Mater. Chem. C* **2020**, *8* (12), 4164–4168.

(27) Lee, J.; Kim, D.; Kim, H.; Seo, S.; Cho, S. M.; Park, N. Formamidinium and Cesium Hybridization for Photo-and Moisture-stable Perovskite Solar Cell. *Adv. Energy Mater.* **2015**, *5* (20), 1501310.

(28) Jiang, Q.; Zhang, X.; You, J. SnO2: A Wonderful Electron Transport Layer for

Perovskite Solar Cells. *Small*. 2018. https://doi.org/10.1002/smll.201801154.

(29) Choi, H.; Mai, C.-K.; Kim, H.-B.; Jeong, J.; Song, S.; Bazan, G. C.; Kim, J. Y.; Heeger, A. J. Conjugated Polyelectrolyte Hole Transport Layer for Inverted-Type Perovskite Solar Cells. *Nat. Commun.* **2015**, *6* (1), 1–6.

(30) Leguy, A. M. A.; Hu, Y.; Campoy-Quiles, M.; Alonso, M. I.; Weber, O. J.; Azarhoosh, P.; Van Schilfgaarde, M.; Weller, M. T.; Bein, T.; Nelson, J. Reversible Hydration of CH3NH3PbI3 in Films, Single Crystals, and Solar Cells. *Chem. Mater.* **2015**, *27* (9), 3397–3407.

(31) Yang, L. W.; Liu, E. E.; Xu, A. F.; Chen, J. Y.; Wang, R. T.; Xu, G. Improving Linear Range Limitation of Non-Enzymatic Glucose Sensor by OH− Concentration. *Crystals* **2020**, *10* (3), 186.

(32) Wang, R. T.; Yang, L. W.; Xu, A. F.; Liu, E. E.; Xu, G. Achieving Nonenzymatic Blood Glucose Sensing by Uprooting Saturation. *Anal. Chem.* **2020**, *92* (15), 10777–10782.

(33) Bao, Q.; Liu, X.; Braun, S.; Fahlman, M. Oxygen-and Water-based Degradation in [6, 6]-phenyl-C61-butyric Acid Methyl Ester (PCBM) Films. *Adv. Energy Mater.* **2014**, *4* (6), 1301272.

(34) Wu, W.; Chen, D.; Cheng, Y.; Caruso, R. A. Thin Films of Tin Oxide Nanosheets Used as the Electron Transporting Layer for Improved Performance and Ambient Stability of Perovskite Photovoltaics. *Sol. Rrl* **2017**, *1* (11), 1700117.

(35) Zheng, H.; Liu, G.; Zhu, L.; Ye, J.; Zhang, X.; Alsaedi, A.; Hayat, T.; Pan, X.; Dai, S. Enhanced Performance and Stability of Perovskite Solar Cells Using

NH4I Interfacial Modifier. *ACS Appl. Mater. Interfaces* **2017**, *9* (46), 41006–41013.

(36)   Wang, R.; Mujahid, M.; Duan, Y.; Wang, Z. K.; Xue, J.; Yang, Y. A Review of Perovskites Solar Cell Stability. *Advanced Functional Materials*. 2019, p 1808843. https://doi.org/10.1002/adfm.201808843.

(37)   Yang, J.; Siempelkamp, B. D.; Liu, D.; Kelly, T. L. Investigation of CH3NH3PbI3degradation Rates and Mechanisms in Controlled Humidity Environments Using in Situ Techniques. *ACS Nano* **2015**. https://doi.org/10.1021/nn506864k.

(38)   Leguy, A. M. A.; Hu, Y.; Campoy-Quiles, M.; Alonso, M. I.; Weber, O. J.; Azarhoosh, P.; van Schilfgaarde, M.; Weller, M. T.; Bein, T.; Nelson, J.; et al. Reversible Hydration of CH3NH3PbI3 in Films, Single Crystals, and Solar Cells. *Chem. Mater.* **2014**. https://doi.org/10.1021/acs.chemmater.5b00660.

(39)   Zhu, Z.; Hadjiev, V. G.; Rong, Y.; Guo, R.; Cao, B.; Tang, Z.; Qin, F.; Li, Y.; Wang, Y.; Hao, F.; et al. Interaction of Organic Cation with Water Molecule in Perovskite MAPbI3: From Dynamic Orientational Disorder to Hydrogen Bonding. *Chem. Mater.* **2016**. https://doi.org/10.1021/acs.chemmater.6b02883.

(40)   Ahn, N.; Kwak, K.; Jang, M. S.; Yoon, H.; Lee, B. Y.; Lee, J. K.; Pikhitsa, P. V.; Byun, J.; Choi, M. Trapped Charge-Driven Degradation of Perovskite Solar Cells. *Nat. Commun.* **2016**. https://doi.org/10.1038/ncomms13422.

(41)   Liu, M.; Johnston, M. B.; Snaith, H. J. Efficient Planar Heterojunction Perovskite Solar Cells by Vapour Deposition. *Nature* **2013**.

https://doi.org/10.1038/nature12509.

(42)   Li, D.; Liao, P.; Shai, X.; Huang, W.; Liu, S.; Li, H.; Shen, Y.; Wang, M. Recent Progress on Stability Issues of Organic–Inorganic Hybrid Lead Perovskite-Based Solar Cells. *RSC Adv.* **2016**, *6* (92), 89356–89366.

(43)   Rau, A. R. P. The Negative Ion of Hydrogen. *Journal of Astrophysics and Astronomy*. 1996. https://doi.org/10.1007/BF02702300.

(44)   Christe, K. O.; Wilson, W. W.; Sheehy, J. A.; Boatz, J. A. N5+: A Novel Homoleptic Polynitrogen Ion as a High Energy Density Material. *Angew. Chemie - Int. Ed.* **1999**. https://doi.org/10.1002/(SICI)1521-3773(19990712)38:13/14<2004::AID-ANIE2004>3.0.CO;2-7.

Chapter 2 Reversing Organic-inorganic Hybrid Perovskite Degradation in Water via pH and Hydrogen Bonds

The moisture instability of organic-inorganic hybrid perovskite solar cells has been a major obstacle to the commercialization, calling for the mechanistic understanding of the degradation process, which has been under debate. Here we present a surprising discovery that the degradation is actually reversible, via in-situ observation of X-ray diffraction, supported by FTIR and SEM. To isolate the hydrogen bond effect, water was replaced by methanol during the in-situ experiment, revealing the decomposition to be initiated by the breakdown of N-H-I hydrogen bonds. This is followed by the step of organic iodide hydrolyzing, which can be inhibited in the neutral environment, making the whole process reversible under variable pH.

TOC GRAPHICS
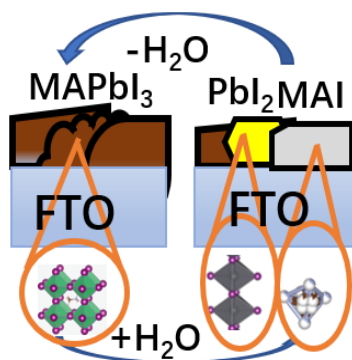
Introduction

Great progress has been achieved in the energy efficiency of the $CH_3NH_3PbI_3$ (MAPbI$_3$) and $CH_5N_2PbI_3$ (FAPbI$_3$) perovskite solar cells since their first report, when the power conversion efficiency increased from 3.8% to 25.2% within the last decade [1,2]. While such record performance seems to inspire a new era for clean energy

development, the stability of such perovskites, especially the moisture stability, remains a challenge, which prevents the commercialization of the perovskite solar cells. The unpacked devices decompose usually within a day [3,4], and with encapsulation the highest lifetime reported is still under 4000 hours, nowhere near the threshold of commercialization [5–7].

Although various attempts have been made, such as replacing A, B and X ions [8,9], morphology engineering [8–10], or employing hydrophobic hole transport layer [11], none resolves the stability issue. This is obviously caused by the nature of blind trials without the mechanistic understanding behind the degradation. As an example, preventing H_2O molecules from contacting the perovskites such as $MAPbI_3$ or $FAPbI_3$, could only delay the problem, rather than eliminate it completely, especially when they are intrinsically unstable [12]. It is thus necessary to unravel the root cause, and to uncover the scientific basis of the decomposition, in order to acquire effective strategies.

Despite a great amount of effort, the degradation mechanism, in particular, still remains a matter of much debate [13–16]. For example, although the decomposition process of $CH_3NH_3PbI_3$ perovskites in a humid environment has been studied by many groups [11-16], contradictory observations have been reported [11,13], and the degradation mechanism has remained unclear with respect to the conflicts. It was found that $CH_3NH_3PbI_3$ is prone to hydrolyze in the presence of water, resulting in degradation products CH_3NH_2, HI, and PbI_2. For example, Niu et al. (2014) proposed that water

dissolves $CH_3NH_3PbI_3$ and deprotonates $CH_3NH_3^+$, leading to the formation of CH_3NH_2, HI, and PbI_2. Such explanation was later questioned by others, as it could not explain the phase change detected during the decomposition [18,19].

In the meantime, this phase change seemed to be accounted for by Leguy et al. (2014), who discovered the $CH_3NH_3PbI_3$ hydrate. They believed that $CH_3NH_3PbI_3$ forms a monohydrate first and a dihydrate next under a humid environment, which breaks the perovskite structure and causes the formation of CH_3NH_3I and PbI_2, and eventually, the CH_3NH_3I reacts with H_2O and the decomposition is no longer reversible. In other words, the structural collapse is attributed to the hydrogen bond breakdown [14]. Their discoveries were also supported by others [19], who believed that only the formation of the monohydrate is reversible, instead of the whole process. Such a seemingly ideal explanation was, however, soon declined by Ahn et al. (2016), who found that, $CH_3NH_3PbI_3$ would not irreversibly decompose in humid condition, instead, it only decomposes with the presence of ions such as N^+ or H^- in the humid environment [16]. In addition, they assumed N^+, H^- ions introduce a "local electric field" to distort the $CH_3NH_3PbI_3$ structure electrostatically. However, N^+ and H^- ions could hardly exist in water in reality, as they would react with water vigorously [20,21]. All this aggravates the controversy, making $CH_3NH_3PbI_3$ stability even more debatable. Numerical simulations of the decomposition process [3,22-26] have also been added to the debate, where the atomic level perceptions are often inconsistent, and the interpretations are usually hypothetical.

It is therefore the purpose of the current letter, to try to end this long dispute and expose the root cause of the organic-inorganic hybrid perovskite decomposition process using $CH_3NH_3PbI_3$ as an example. Employing in-situ X-ray diffraction (XRD), Fourier-transform infrared spectroscopy (FTIR)，and scanning electron microscopy (SEM), we were able to reveal the influence of hydrogen bonds on the structural stability, and to uncover for the first time the root cause of the degradation. In particular, we discovered by surprise that CH_3NH_3I is stable in water. This is one factor which allows the decomposition of $CH_3NH_3PbI_3$ to be reversible when annealed at around 90 °C after the decomposition in water. By the addition of acid or base into the water, we revealed the real culprit of $CH_3NH_3PbI_3$ degradation, which not only advances the conceptual understanding of $CH_3NH_3PbI_3$ instability successfully, but also differentiates various hypotheses and conflicts.

Results & Discussion

To identify the true cause of the degradation, the in-situ XRD measurement was first adopted by creating a methanol environment, rather than that of moisture, to isolate the effect of hydrogen bonds, which allows for a better controlled observation of the $CH_3NH_3PbI_3$ decomposition. Although similar in-situ experiments have been conducted before using water vapor, H_2O would affect $CH_3NH_3PbI_3$ in many ways, including hydrogen bonds, hydration reaction or dissolution [17], which may overshadow the effect of hydrogen bonds. Hence in our case, H_2O was replaced by methanol, which

19

is also capable of forming intermolecular hydrogen bonds with the perovskite. It is thus necessary to use CH_3OH, instead of water in the first place, to isolate the effect of hydrogen bonds and eliminate the possibility of hydration reaction.

Preliminary experiment was conducted in the ex-situ environment beforehand to determine the scan range of the in-situ measurement. As shown in Figure (2. 1a), while the ex-situ results proved the decomposition of $CH_3NH_3PbI_3$ in methanol liquid, further in-situ measurement was necessary to study the decomposition process, not only because the ex-situ experiment was unable to detect the compositional change with time, but also because the characteristic peaks of $CH_3NH_3PbI_3$ and CH_3NH_3I are too close to be separated in high theta range measurement. Two theta range of 36.3-41.5° were selected to conduct the in-situ measurement, as this range contains characteristic peaks of $CH_3NH_3PbI_3$, CH_3NH_3I and PbI_2. As demonstrated in Figure (2. 1b), the peak at 37.2° was weakening over time in methanol-enriched environment, while peaks at 36.8° and 40° were strengthened over time, which displayed a live phase change from $CH_3NH_3PbI_3$ to CH_3NH_3I and PbI_2. This degradation can be attributed to the -OH group in methanol, which disrupted the interaction between $CH_3NH_3^+$ and PbI_6^- octahedral via hydrogen bonding.
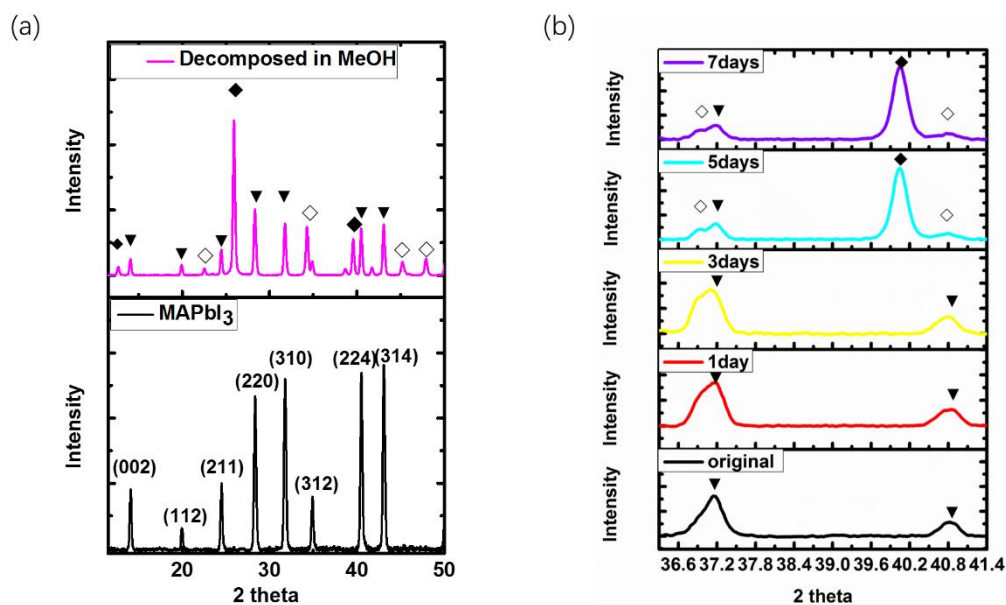
Figure 2. 1. (a)XRD results (WL=1.54Å) of $CH_3NH_3PbI_3$ before and after immersion in liquid methanol, $CH_3NH_3PbI_3$ gradually reformed as methanol evaporates; (b) In-situ XRD monitoring of $CH_3NH_3PbI_3$ decomposition in methanol for 7 days (WL=1.78Å); ▼: $MAPbI_3$; ◆: PbI_2; ◇: MAI.

Further evidence was obtained by FTIR spectroscopy. As shown in Figure 2. 2, the peaks of fresh $CH_3NH_3PbI_3$, as well as that after the methanol degradation were displayed. The methyl group produces rocking absorption at 910 cm^{-1}, and scissoring at 1470 cm^{-1}, whereas the ammonium functional groups are rocking at 1000 cm^{-1} and 1250 cm^{-1}, bending at 1650 cm^{-1}, and stretching at 3100 cm^{-1} [27]. Conspicuous signal strength and width increase in all the ammonium functional group related peaks were observed along the black curve, attributed to the hydrogen bonding interaction in N-H-I [28].
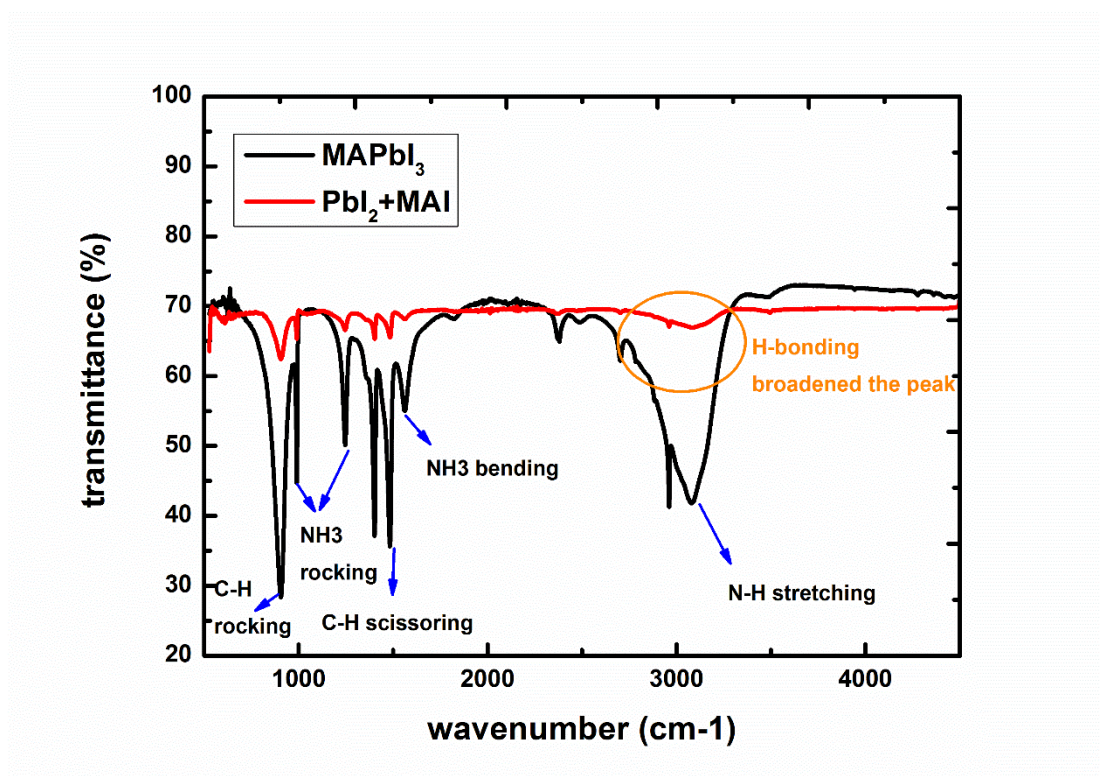
Figure 2. 2. FTIR results of $CH_3NH_3PbI_3$ before and after decomposition in methanol.

In a subsequent analysis, SEM was employed before and after the decomposition by methanol. Significant differences were observed. Before the degradation, clear $CH_3NH_3PbI_3$ grain boundaries were visible, with grain sizes of ca. 1 μm, as shown in Figure (2. 3a). Such morphology changed completely after the decomposition, as can be viewed in Figure (2. 3b), where large cubes were surrounded by needle-like fibers, indicating that $CH_3NH_3PbI_3$ has now been decomposed by CH_3OH, and CH_3NH_3I is surrounded by PbI_2 fibers [29]. This was further verified by the EDS results (Figure S2.3), which showed no CH_3NH_3I in needle-shaped areas, as no nitrogen element was detected.
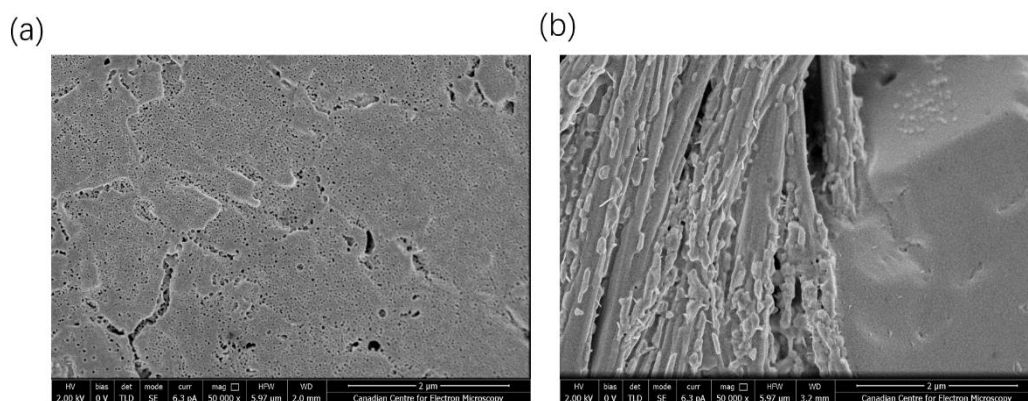
Figure 2. 3. SEM results of $CH_3NH_3PbI_3$ (a) before and (b) after decomposition in methanol.

A critical step has been achieved by the results of these experiments, viz., it was indeed the hydrogen bonds, which initiated the structural breakdown. This could otherwise not be verified by the similar experiments involving H_2O vapor.

Beyond the initiation of structure breakdown by hydrogen bonds, the next stage of degradation of the remaining substance in moisture condition may also be investigated by XRD, such as the possible hydrolysis of CH_3NH_3I, leading to the complete decomposition of $CH_3NH_3PbI_3$. By wetting $CH_3NH_3PbI_3$ thin film sample in water, it was found that, the degradation products changed back to $CH_3NH_3PbI_3$ after annealing, which was believed to be impossible before [14–18]. As can be found in Figure (2. 4a), after immersion in water the $CH_3NH_3PbI_3$ (black) sample became yellow within 30s, which was confirmed by XRD, showing CH_3NH_3I, PbI_2 and $(CH3NH_3)_4PbI_6 \cdot 2H_2O$. The yellow sample was changed back to black color by annealing at 90 °C for 25 min,

as illustrated in Figure (2. 4b). There was no residual water on the reannealed film, as no hydrate was detected by XRD. Such reversibility could be maintained even after several decomposition-regeneration cycles, which has never been reported before. It proves that degree of hydrolysis of CH₃NH₃I is relatively low in water, otherwise it would be consumed completely.
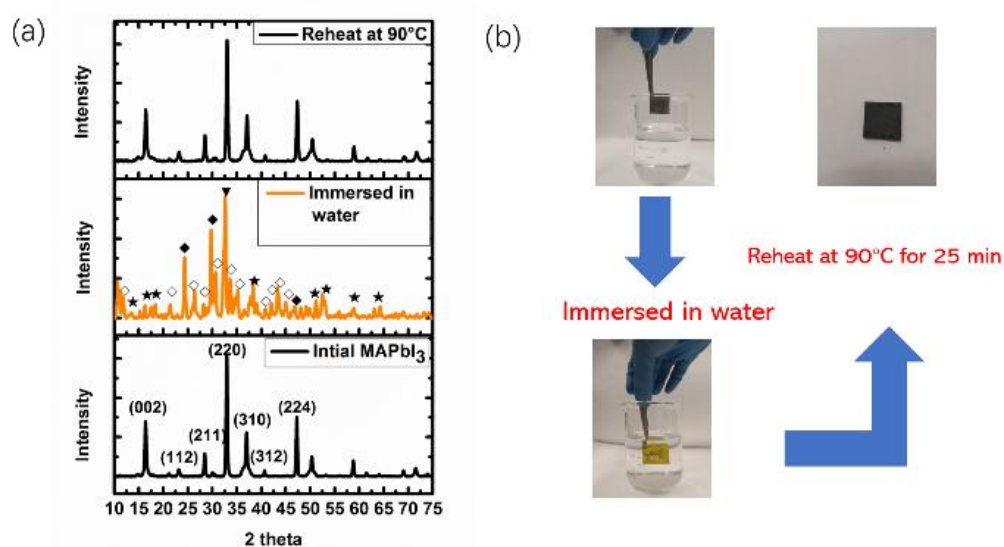
Figure 2. 4. (a) XRD results of CH₃NH₃PbI₃ before and after wetting in water; (b)the pictures of the film before and after it's immersed in water, as well as the reheated film. ★: MAPbI₃ dihydrate, ◆: PbI₂, ▼: MAPbI₃, ◇: MAI.

Last but not least, it was found that, although CH₃NH₃I hydrolysis is inhibited in water, and CH₃NH₃PbI₃ degradation is completely reversible, such stability and reversibility cannot be maintained if the pH is increased to the alkaline realm. To investigate the influence of H⁺ and OH⁻, the CH₃NH₃PbI₃ samples were measured after immersion in 1 mol/L HCl and NaOH, respectively, and followed by annealing at 90 °C

for 25 min. According to the XRD results, shown in Figure (2. 5a), under alkaline condition, after the initiation of breakdown by hydrogen bonds, i.e., $CH_3NH_3PbI_3$ into CH_3NH_3I and PbI_2, the hydrolysis of CH_3NH_3I did happen when facilitated by hydroxide ions, and $CH_3NH_3PbI_3$ was completely decomposed (scheme 1). At high OH^- concentrations, PbI_2 reacted with OH^- to become $Pb_2O(OH)I$ (scheme 2). While in the acidic environment, $CH_3NH_3PbI_3$ turned black by heating. The reversibility is maintained, leaving only a small amount of untransformed PbI_2. A schematic illustration of the reaction path in acid and base is shown in Figure (4. 5b).

$$CH_3NH_3I + OH^- \rightarrow CH_3NH_2 \uparrow + H_2O + I^- \qquad \text{Scheme (1)}$$

$$PbI_2 + OH^- \rightarrow Pb_2O(OH)I \qquad \text{Scheme (2)}$$
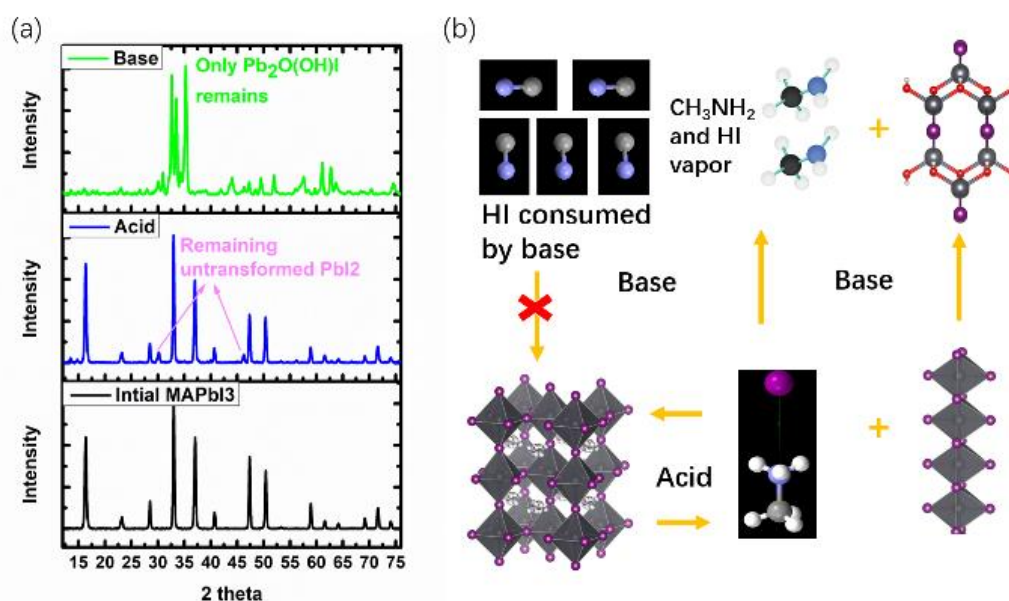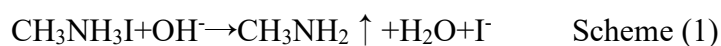
Figure 2. 5. (a) XRD results of fresh $CH_3NH_3PbI_3$ and decomposed $CH_3NH_3PbI_3$ in acid and base; (b) the schematic illustration of the reaction path in acid and base, respectively.

A clearer picture can now be established by the above experiments, in comparison to the literature, where the influence of hydrogen bonds could be masked, and reversible reaction overlooked, especially the influence of pH neglected [13,14]. Although the influence of coexisting N^+/H^- and water has been probed, and $CH_3NH_3PbI_3$ was believed to degrade irreversibly under the presence of both ions and water [16], the N^+ and H^- ions are highly active and prone to react with water [20,21], which implies N^+/H^- and water may not coexist. The actual influence of ions was found to be on the hydrolysis of CH_3NH_3I, as indicated by the results here, which is accelerated in basic environment.

With our new findings, the degradation process at the atomic level can now be uncovered by the solution synthesis mechanism of $CH_3NH_3PbI_3$ perovskite. As shown in Figure 2. 6, during the solution synthesis process, a 2-D sheet of PbI_2 crystal converts to a 1-D strips when dissolved in polar solvent. Next, the CH_3NH_3I intercalates into those strips and connects them to form a 3-D perovskite structure by Pb-I-Pb interaction and H-I hydrogen bonds. When both hydrogen bonds are destroyed; the Pb-I-Pb interaction is vulnerable to the substitution by the lone pair electron in oxygen from water, which enables $CH_3NH_3^+$ and I^- to move and breaks the 3-D structure. Reversible reaction is only possible if the 2 components are activated to form those bonds again.
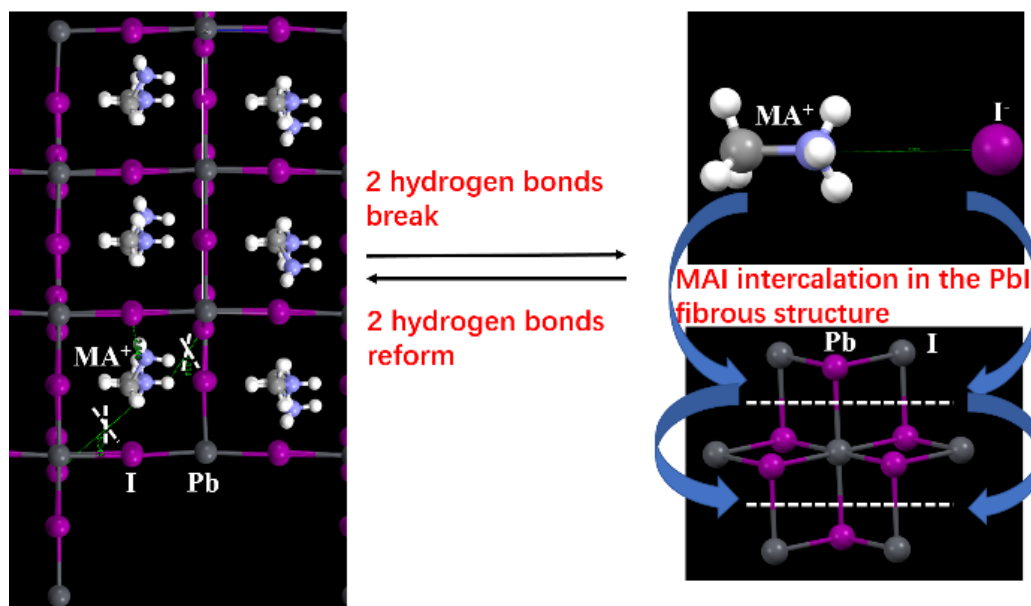
Figure 2. 6. Schematic illustration of $CH_3NH_3PbI_3$ reversible decomposition.

Moreover, the inhibition of CH_3NH_3I hydrolysis in water may now be explained by our pH results and single crystal XRD, giving that the CH_3NH_3I hydrolysis will be influenced by the concentration of hydroxide ions. In the neutral environment, the OH^- concentration is low, thus the hydrolysis reaction is inhibited. While in basic condition, OH^- accelerates the hydrolysis reaction, which is why only PbI_2 remains eventually. In addition, CH_3NH_3I is connected by ionic bonds, a type of bond with large bonding energy. Thus, single crystal XRD on CH_3NH_3I may be conducted to estimate its ionic bonding energy a priori. The result shows that the distance between I^- and H attached to nitrogen is 3.97 Å. From the calculation of Chem3D Pro [30], the bonding energy between $CH_3NH_3^+$ and I^- was found to be 1.5 eV, which closely resembles that from the modelling results (1eV) [31].

To summarize, the moisture decomposition of $CH_3NH_3PbI_3$ may be separated into two steps. In the first step, H_2O molecules get inside the $CH_3NH_3PbI_3$ layer, to start the interaction of H_2O with $CH_3NH_3^+$, as the latter is more likely to form hydrogen bonds with H_2O. This relocation of the hydrogen bonds removes the support inside the $CH_3NH_3PbI_3$ to maintain its 3D structure, which in turn collapses into PbI_2 fibrous intermediate and CH_3NH_3I. In the second step, CH_3NH_3I reacts with OH^- in water, forming CH_3NH_2 and HI gas, making the water slightly acidic. However, the hydrolysis reaction of CH_3NH_3I is inhibited by the low concentration of OH^- and the ionic bonding energy of CH_3NH_3I, allowing the degradation process of $CH_3NH_3PbI_3$ to be reversible.

Conclusion

In conclusion, the degradation process of organic-inorganic hybrid perovskite in humid environment has been successfully elucidated through $CH_3NH_3PbI_3$, and such degradation is found to be completely reversible. This pleasant surprise may offer new hope for the commercialization of perovskite solar cells. Given the fact that perovskite solar cells effective operational temperature could range from -40 °C to $+85$ °C [32], it is possible to recover the device performance if the unstable Spiro-MeOTAD hole transport layer is replaced by other stable structures such as NiO_x or mesoporous carbon, which may result in a longer device lifetime. Based on the regeneration of the perovskite at 90 °C, similar results can be anticipated at slightly lower temperature of 85 °C or even 80 °C, which could certainly become part of the follow-up studies. Hopefully, these findings would give conceptual advance in understanding or

methodology that will be of immediate help to other researchers.

Experimental

N, N-Dimethylformamide (>99%), Methanol (anhydrous, 99.8%), NaOH (BioXtra, $\geq$98%) and hydrochloric acid (ACS reagent, 37%) were purchased from Sigma-Aldrich. CH_3NH_3I (>99.98%, anhydrous) and PbI_2 (>99.98%) were purchased from Xi'an Polymer Light Technology Corp.

The thin film sample was made by drop casting. CH_3NH_3I and PbI_2 (1mmol) were dissolved in N, N-Dimethylformamide (1ml). The solution was drop-casted on Fluorine-doped-Tin-Oxide glass substrate (composition: SiO_2/F; film thickness: 500 nm; purchased from Huanan-Xiangcheng Tech Ltd). Following the previous report, the annealing temperature of 90 °C was adopted [17].

In-situ measurement was conducted on a special chamber with vent tubes by Bruker D8 ADVANCE diffractometer. The thin film sample was mounted in a fully enclosed chamber. The methanol vapor was sent to the chamber via dry nitrogen; $CaSO_4$ (98% $CaSO_4$, 2% $CoCl_2$, anhydrous, purchased from McMaster chemical store) was also added in the chamber as desiccant, the lid was tightly closed to ensure the saturation vapor pressure of methanol, diagram of in-situ chamber can be found in support information Figure S1. In the in-situ XRD, measurement region of 36.3-41.5° was selected since the whole 2 theta range requires several hours for a single scan. The XRD measurement was repeated every 30 minutes for 7 days.

Powder XRD was conducted with a Bruker D8 DISCOVER diffractometer; measurements were taken in the 2θ range of 10 to 76°. CH_3NH_3I was purchased from Xi'an Polymer Light Technology Corp., and a single crystal of 0.2*0.2*0.2 cm in size was chosen for analysis on a Bruker APEX-II diffractometer; data was processed in APEX2 V2014.9.0, structure solution, and refinement in SHELXT and SHELXL (Sheldrick, 2015). FTIR spectroscopy was conducted on a Nicolet 6700 FT-IR Spectrometer. SEM was measured by FEI Magellan 400 XHRSEM, and the sample was transferred in air to the apparatus, when some pinholes were generated in the morphology, which could be eliminated by conducting the measurement in a glovebox. All diagrams were drawn in Origin9.0.

Support information in the appendix

Lists of the contents of material supplied
Figure S4. 1. (a)Schematic illustration of the in-situ XRD measurement chamber; (b) the actual picture of the in-situ XRD chamber.
Figure S4. 2. (a)Crystal structure of CH_3NH_3I; (b) calculated powder XRD pattern of CH_3NH_3I based on single crystal data.

Figure S4. 3. (a)Fibrous (spectrum 1) and cubic area (spectrum 2) chosen for EDS analysis; (b) EDS peaks for spectrum 1; (c) EDS peaks for spectrum 2; (d) weight percent distribution of elements in spectrum 1&2, carbon in spectrum 1 comes from the surface carbon coating instead of CH_3NH_3I as no nitrogen was detected (the EDS is useful as a qualitative analysis, but certainly not for a quantitative one, as its accuracy is limited).

Table S1. Crystal data and structure refinement for CH_3NH_3I.

Reference

1 Kojima, A.; Teshima, K.; Shirai, Y.; Miyasaka, T. Organometal Halide Perovskites as Visible-Light Sensitizers for Photovoltaic Cells. J. Am. Chem. Soc. 2009, 131 (17), 6050– 6051, DOI: 10.1021/ja809598r

2 Kim, H.-S.; Hagfeldt, A.; Park, N.-G. Morphological and Compositional Progress in Halide Perovskite Solar Cells. Chem. Commun. 2019, 55, 1192, DOI: 10.1039/C8CC08653B

3 Tong, C. J.; Geng, W.; Tang, Z. K.; Yam, C. Y.; Fan, X. L.; Liu, J.; Lau, W. M.; Liu, L. M. Uncovering the Veil of the Degradation in Perovskite CH3NH3PbI3 upon Humidity Exposure: A First-Principles Study. J. Phys. Chem. Lett. 2015, 6, 3289, DOI: 10.1021/acs.jpclett.5b01544

4 Boix, P. P.; Agarwala, S.; Koh, T. M.; Mathews, N.; Mhaisalkar, S. G. Perovskite Solar Cells: Beyond Methylammonium Lead Iodide. J. Phys. Chem. Lett. 2015, 6, 898, DOI: 10.1021/jz502547f

5 Barnea-Nehoshtan, L.; Kirmayer, S.; Edri, E.; Hodes, G.; Cahen, D. Surface Photovoltage Spectroscopy Study of Organo-Lead Perovskite Solar Cells. J. Phys. Chem. Lett. 2014, 5, 2408, DOI: 10.1021/jz501163r

6 Gao, W.; Ran, C.; Li, J.; Dong, H.; Jiao, B.; Zhang, L.; Lan, X.; Hou, X.; Wu, Z. Robust Stability of Efficient Lead-Free Formamidinium Tin Iodide Perovskite Solar

Cells Realized by Structural Regulation. J. Phys. Chem. Lett. 2018, 9, 6999, DOI: 10.1021/acs.jpclett.8b03194

7 Xu, A. F.; Wang, R. T.; Yang, L. W.; Liu, N.; Chen, Q.; LaPierre, R.; Isik Goktas, N.; Xu, G. Pyrrolidinium Containing Perovskites with Thermal Stability and Water Resistance for Photovoltaics. J. Mater. Chem. C 2019, 7, 11104, DOI: 10.1039/C9TC02800E

8 Huang, J.; Gu, Z.; Zuo, L.; Ye, T.; Chen, H. Morphology Control of Planar Heterojunction Perovskite Solar Cells with Fluorinated PDI Films as Organic Electron Transport Layer. Sol. Energy 2016, 133, 331, DOI: 10.1016/j.solener.2016.04.017

9 Tai, E. G.; Wang, R. T.; Chen, J. Y.; Xu, G. A Water-Stable Organic-Inorganic Hybrid Perovskite for Solar Cells by Inorganic Passivation. Crystals 2019, 9 (2), 83, DOI: 10.3390/cryst9020083

10 Gao, Y.; Wu, Y.; Lu, H.; Chen, C.; Liu, Y.; Bai, X.; Yang, L.; Yu, W. W.; Dai, Q.; Zhang, Y. CsPbBr3 Perovskite Nanoparticles as Additive for Environmentally Stable Perovskite Solar Cells with 20.46% Efficiency. Nano Energy 2019, 59, 517– 526, DOI: 10.1016/j.nanoen.2019.02.070

11 Xiong, H.; Rui, Y.; Li, Y.; Zhang, Q.; Wang, H. Hydrophobic Coating over a CH3NH3PbI3 Absorbing Layer towards Air Stable Perovskite Solar Cells. J. Mater. Chem. C 2016, 4, 6848, DOI: 10.1039/C6TC02238C

12 Wang, R. T.; Tai, E. G.; Chen, J. Y.; Xu, G.; LaPierre, R.; Goktas, N. I.; Hu, N. A KMnF3 Perovskite Structure with Improved Stability, Low Bandgap and High Transport Properties. Ceram. Int. 2019, 45 (1), 64, DOI:

10.1016/j.ceramint.2018.09.134

13 Yang, J.; Siempelkamp, B. D.; Liu, D.; Kelly, T. L. Investigation of CH3NH3PbI3 Degradation Rates and Mechanisms in Controlled Humidity Environments Using in Situ Techniques. ACS Nano 2015, 9, 1955, DOI: 10.1021/nn506864k

14 Leguy, A. M. A.; Hu, Y.; Campoy-Quiles, M.; Alonso, M. I.; Weber, O. J.; Azarhoosh, P.; van Schilfgaarde, M.; Weller, M. T.; Bein, T.; Nelson, J. Reversible Hydration of CH3NH3PbI3 in Films, Single Crystals, and Solar Cells. Chem. Mater. 2015, 27, 3397, DOI: 10.1021/acs.chemmater.5b00660

15 Zhu, Z.; Hadjiev, V. G.; Rong, Y.; Guo, R.; Cao, B.; Tang, Z.; Qin, F.; Li, Y.; Wang, Y.; Hao, F. Interaction of Organic Cation with Water Molecule in Perovskite MAPbI3: From Dynamic Orientational Disorder to Hydrogen Bonding. Chem. Mater. 2016, 28, 7385, DOI: 10.1021/acs.chemmater.6b02883

16 Ahn, N.; Kwak, K.; Jang, M. S.; Yoon, H.; Lee, B. Y.; Lee, J. K.; Pikhitsa, P. V.; Byun, J.; Choi, M. Trapped Charge-Driven Degradation of Perovskite Solar Cells. Nat. Commun. 2016, DOI: 10.1038/ncomms13422

17 Niu, G.; Guo, X.; Wang, L. Review of Recent Progress in Chemical Stability of Perovskite Solar Cells. J. Mater. Chem. A 2015, 3, 8970, DOI: 10.1039/C4TA04994B

18 Niu, G.; Li, W.; Meng, F.; Wang, L.; Dong, H.; Qiu, Y. Study on the Stability of CH3NH3PbI3 Films and the Effect of Post-Modification by Aluminum Oxide in All-Solid-State Hybrid Solar Cells. J. Mater. Chem. A 2014, 2, 705, DOI: 10.1039/C3TA13606J

19 Christians, J. A.; Miranda Herrera, P. A.; Kamat, P. V. Transformation of the Excited

State and Photovoltaic Efficiency of CH3NH3PbI3 Perovskite upon Controlled Exposure to Humidified Air. J. Am. Chem. Soc. 2015, 137, 1530,   DOI: 10.1021/ja511132a

20 Rau, A. R. P. The Negative Ion of Hydrogen. J. Astrophys. Astron. 1996, 17, 113, DOI: 10.1007/BF02702300

21 Christe, K. O.; Wilson, W. W.; Sheehy, J. A.; Boatz, J. A. N5+: A Novel Homoleptic Polynitrogen Ion as a High Energy Density Material. Angew. Chem., Int. Ed. 1999, 38, 2004

22 Jong, U. G.; Yu, C. J.; Ri, G. C.; McMahon, A. P.; Harrison, N. M.; Barnes, P. R. F.; Walsh, A. Influence of Water Intercalation and Hydration on Chemical Decomposition and Ion Transport in Methylammonium Lead Halide Perovskites. J. Mater. Chem. A 2018, 6, 1067,   DOI: 10.1039/C7TA09112E

23 Eames, C.; Frost, J. M.; Barnes, P. R. F.; O'Regan, B. C.; Walsh, A.; Islam, M. S. Ionic Transport in Hybrid Lead Iodide Perovskite Solar Cells. Nat. Commun. 2015, DOI: 10.1038/ncomms8497

24 Zhang, L.; Sit, P. H.-L. Ab Initio Study of Interaction of Water, Hydroxyl Radicals, and Hydroxide Ions with CH3NH3PbI3 and CH3NH3PbBr3 Surfaces. J. Phys. Chem. C 2015, 119, 22370,   DOI: 10.1021/acs.jpcc.5b07000

25 Evans, H. A.; Fabini, D. H.; Andrews, J. L.; Koerner, M.; Preefer, M. B.; Wu, G.; Wudl, F.; Cheetham, A. K.; Seshadri, R. Hydrogen Bonding Controls the Structural Evolution in Perovskite-Related Hybrid Platinum(IV) Iodides. Inorg. Chem. 2018, 57, 10375,   DOI: 10.1021/acs.inorgchem.8b01597

26 Mosconi, E.; Azpiroz, J. M.; De Angelis, F. Ab Initio Molecular Dynamics Simulations of Methylammonium Lead Iodide Perovskite Degradation by Water. Chem. Mater. 2015, 27, 4885, DOI: 10.1021/acs.chemmater.5b01991

27 Abdelmageed, G.; Jewell, L.; Hellier, K.; Seymour, L.; Luo, B.; Bridges, F.; Zhang, J. Z.; Carter, S. Mechanisms for Light Induced Degradation in MAPbI3 Perovskite Thin Films and Solar Cells. Appl. Phys. Lett. 2016, 109, 233905, DOI: 10.1063/1.4967840

28 de Vries, M. S.; Hobza, P. Gas-Phase Spectroscopy of Biomolecular Building Blocks. Annu. Rev. Phys. Chem. 2007, 58, 585, DOI: 10.1146/annurev.physchem.57.032905.104722

29 Guo, Y.; Shoyama, K.; Sato, W.; Matsuo, Y.; Inoue, K.; Harano, K.; Liu, C.; Tanaka, H.; Nakamura, E. Chemical Pathways Connecting Lead(II) Iodide and Perovskite via Polymeric Plumbate(II) Fiber. J. Am. Chem. Soc. 2015, 137, 15907, DOI: 10.1021/jacs.5b10599

30 Gundertofte, K.; Liljefors, T.; Norrby, P. O.; Pettersson, I. A Comparison of Conformational Energies Calculated by Several Molecular Mechanics Methods. J. Comput. Chem. 1996, 17, 429

31 Caddeo, C.; Saba, M. I.; Meloni, S.; Filippetti, A.; Mattoni, A. Collective Molecular Mechanisms in the CH3NH3PbI3 Dissolution by Liquid Water. ACS Nano 2017, 11, 9183, DOI: 10.1021/acsnano.7b04116

32 Snaith, H. J.; Hacke, P. Enabling Reliability Assessments of Pre-Commercial Perovskite Photovoltaics with Lessons Learned from Industrial Standards. Nat. Energy 2018, 3, 459, DOI: 10.1038/s41560-018-0174-4.

Chapter 3 Moisture Stable FAPbI3 Perovskite Achieved By Atomic Structure Negotiation

Broad impact may be anticipated to the research community when the materials properties are capable of being manipulated artificially. Such possibility has been explored here by FAPbI$_3$ perovskite structure of the PSC solar cells, which involves undesirable phase transition at working temperature, despite many attempts to resolve the issue. Essential steps have been made here towards solving this problem by adopting opposite strategy to incorporate the water molecules into the perovskite structure, under the current materials framework by new structural physics maneuvering. The secondary bonding of the perovskite structure has been relocated, which altered the microstructure to remove the internal strain that caused the phase transition, resulting in not only a 10-fold enhancement in the moisture/structure stability, but also a comparable bandgap of the favorite α-FAPbI$_3$. All this opens unprecedented avenue in the perovskite research, which will hopefully be of intrinsic interest to the broad materials research community as well.

Introduction

Much progress has been achieved in the commercialization of perovskite solar cells since 2009 [1], especially the FAPbI$_3$ (Formamidinium lead iodide) based device [2,3], which showed a more promising energy bandgap than its counterpart, such as MAPbI$_3$ [4], or CsPbI$_3$ [5]. The power conversion efficiency (PCE) of such device has been enhanced from 3.8% to 25.2% [2], inspiring a new era for sustainable energy

development.

Despite the excellent PCE, the stability remained a major challenge [6]. Especially, the FAPbI₃ was found to undergo α-δ phase transformation at room temperature, which would complete within several hours even under the protection of the nitrogen [7–9]. Even worse, such transition can even be accelerated by moisture, which could complete within several minutes. This was devastating for the PCE as it could increase the bandgap to above 2.5eV [10]. As a result, a great deal of effort has since been devoted to trying to eliminate the water intrusion and impede the phase transition, such as strain engineering [11,12], interface engineering [13,14], or doping in the A/B/X sites in the ABX₃ structure of perovskite [15–20].

Unfortunately, these quick attempts didn't extend the perovskite lifetime to any appreciable level, due not least to the debatable phase transition mechanism [21,22], in particular, the influence of water molecules on the perovskite structure, in addition to the possible structural variations vis-a-vis the kinetics and thermodynamics. Therefore, such effects were destined to be less than successful. It is absolutely necessary to fill the critical gap and propose fresh strategies accordingly.

In fact, the attempts in the literature have largely been based more on blind trials, rather than on the phase transition physics. For example, most of the research about the phase transition has been focused on nitrogen atmosphere, ignoring the presence of moisture

in the actual operating environment. In addition, the current trials such as doping or interface engineering could only delay the problem, rather than eliminate it completely, when α phase is thermodynamically unstable at room temperature [3,7]. Nor could the encapsulation be the answer, especially when it was discovered that the presence of moisture could accelerate the phase transition [10,15,23]. All these discoveries just aggravated the challenge, making the entire understanding more elusive.

It is, therefore, the purpose of this report, to resolve the challenge by a totally opposite strategy, more specifically, by embracing the moisture instead of eliminating it. As has been confirmed in the previous results [24,25], H-bond is the pivotal force to maintain the perovskite structure. Based on the FTIR measurements, it is discovered that $FAPbI_3$ is capable of forming 3 intermolecular H-bonds, one of which can be replaced by the water molecule to enhance the stability of the structure, as has been done in their counterparts of $MAPbI_3$ [24].Thus, a stable structure of similar bandgap of α-$FAPbI_3$ is synthesized by adding one water molecule to the perovskite. From the single crystal measurements and thermodynamic/kinetics calculation, it has been revealed that the internal strain of α-$FAPbI_3$, which was believed to be the root cause of the phase transition, has been removed by the enlarged unit cell of the novel structure. This unprecedent technique of structural maneuvering opens a fresh channel to control the materials properties via chemical structure negotiation, delivering not only critical steps towards solving the challenge, but also possible inspiration for the wide materials research community.

Experimental

X-ray diffraction (XRD) patterns were obtained using a Rigaku D/Max 2,200 with Cu Kα as the X-ray source. The time-resolved XRD measurements was conducted by Bruker D8 ADVANCE diffractometer with CuKa1 radiation (λ= 1.79026 Å) in the range of 6-26° (2θ). The XRD measurement was repeated every 20 min for 7 days. SEM was measured by a FEI Magellan 400 XHRSEM. Nicolet 6700 FT-IR spectrometer was used to acquire the FTIR spectra in the wavenumber range of 400–4000 cm^{-1}, which has $0.09cm^{-1}$ resolution with continuous dynamic alignment and auto-tune function. UV-vis-NIR absorption spectroscopy were conducted by the Cary 5000 UV–vis–NIR Spectrophotometer, from 850 nm to 400 nm. The current density–voltage characteristics of photovoltaic devices were obtained using a Keithley 2400 source-measure system. The photocurrent was measured under AM 1.5 G illumination at 100 mW/cm^2 using a Newport Thermal Oriel 91192 1000 W solar simulator. The light intensity was calibrated using a KG-5 Si diode. The effective area of each cell was 0.102 cm^2 defined by masks for all the photovoltaic devices discussed in this work. Current density–voltage measurements were carried out at room temperature.

Results & Discussion

To obtain a more detailed understanding, the reaction between water molecules and $FAPbI_3$ have been investigated, which leads to a concealed phase map that varies as a function of geometrical parameters and water vapour pressure. Three new phases have

been discovered at high water pressure environment which has been confirmed by the XRD results. As shown in Fig. (5. 1a), the ε phase was generated when the molar ratio of water and FAPbI$_3$ reached 1:1. Some unidentified peaks were observed, which cannot be recognized by the database, proving the generation of a fresh structure. The unknown peaks of 2 theta at 9.68°, 13.2°, 16.9°, 22.7°, 37.2°, 49.4°, 51.3°, and 59.1° matched the calculated powder diffraction pattern by the single crystal XRD measurement of the ε needle, as shown in Fig. S5. 1. Next, such phase gradually transformed to θ and μ phases after the molar ratio of water and FAPbI$_3$ reached 1:2 and 1:3, respectively. Based on the XRD results, it can be shown that the formation of hydrates depends on the molar ratio of water and FAPbI$_3$, which introduced the relative stability of ε/θ/μ phases. When one proportion of water was added into the thin film, the molar ratio of water and FAPbI$_3$ in the surrounding area of the water droplet was much higher than 3:1, which should generate θ and μ phases in theory. In reality, however, only ε phase was detected in the XRD measurement, indicating θ and μ phases generated in the early stage have transformed back to the ε phase as time proceeds, proving the ε phase is the most thermodynamically stable.

More definitive evidence has also been found in the time-resolved XRD measurement results. As shown in Fig. (3. 1b), the α phase will be converted to μ phase at high water vapour pressure environment within half an hour, which was transformed into θ phase and eventually ε phase in 2 hours under the dryer environment. The ε phase, on the other hand, exhibited unexpected stability in such an environment, which remained

stable for more than 7 days. The transition path from α/δ to the hydrates is therefore unraveled: at first, water vaporized into water vapour molecules which assisted α/δ to be completely transformed into the ε phase; next, ε will be converted into θ and μ phase at higher water vapour pressure environment; in the following stage, some of the θ and μ phases will be transformed back to the ε phase as they are less stable. Eventually, an equilibrium will be attained. A single crystal of ε phase can thus be successfully synthesized, which exhibited a needle-like shape, as shown in Fig (3. 1d).

Furthermore, thermodynamic and kinetic calculations were preformed based on the XRD results. The Gibbs free energy difference between the δ phase and the hydrate phases can be obtained by the transformation fraction of the transition process, as shown in supporting information, which is determined by the relative peak heights of each phase in Fig. (3. 1a). Following the thermodynamics, the transition fraction should be equal to exp(-ΔG/RT) [3]. Hence, at 298K, the ΔG of (δ-ε) was calculated to be -0.12eV, the ΔG of (δ-θ) -0.015eV, and the ΔG of (δ-μ) -0.007eV, proving that the ε phase is indeed the most thermodynamically stable. Although kinetically, ΔG is the driving force for the phase transition, the rate-control parameter is determined by the activation energy Ea of each transition, which also decides the lifetime/stability of each phase. As shown in Fig. (3. 2a&b), the phase map provided not only the thermodynamic state of each phase, but also the activation energy Ea for each transition, which is obtainable by combining and analyzing the existing data and that of the literature [26,27]. As evidenced by Fig. (3. 1c), the hydration reaction involves water

vaporization, absorption of water vapour, and structural change. It was obvious that during the hydration process, absorption of water vapour contributed most of the entropy change due to its reduction of the degree of randomness. Water vaporization is thus the actual rate control process, which decides the value of activation energy for the hydration reaction to be similar to the latent heat of 0.45eV for water vaporization [28]. It has thus been quantitatively proved that all three hydrates are genuine phases instead of intermediate states, because they are more stable than α and δ phases. Our discovery of these new phases introduced profound engineering implications, not least of which is the surface engineering or bandgap engineering that can be verified by the following measurements.

In order to investigate the origin of the hydrate phase stability, FTIR measurements have been conducted to reveal the bonding details. As can be confirmed by Fig. (3. 3a), the stability of the hydrates was attributed to the hydrogen bond of the water molecule as evidenced at 2400-3000cm^{-1} and 3000-3600cm^{-1}, which were generated by the N-H groups and H-O-H groups, respectively [29,30]. The peak amplitude of the H-O-H groups at 3000-3600 cm^{-1} increased as the hydrate forms at the expense of the peak amplitude of the N-H groups at 2400-3000cm^{-1}, indicating the H-bonding in the N-H groups was diminishing while the H-bonding in the H-O-H groups was increasing. More quantitative information can be extracted from Fig. (3. 3b), where the FTIR signal of the α phase was used as the baseline to be subtracted by other phases. The most obvious peak can be found at 3370cm^{-1}, where the ϵ phase gives an absorption of

around 6%, θ~ 12%, and μ~15%. The ratio of FTIR absorption of these 3 phases matches closely to 1:2:3, revealing the number of the hydrogen bonds within each monohydrate, dihydrate and trihydrate to be 1, 2, and 3, respectively.

The relocation of the hydrogen bonds altered the crystal structure of the hydrates, as has been systematically investigated by single crystal XRD. Although ε phase showed a hexagonal structure and a space group of $P6_3mc$, similar to that of the δ phase, it demonstrated a larger unit cell, as can be confirmed in Fig. (3. 3e). The enlarged unit cell releases the strain energy generated by the large FA^+ ion, which is beneficial to a favourable bandgap, as can be evidenced by the previous bandgap engineering research [16,31,32] and the bandgap measurements in Fig. (3. 3c&d). The ε showed a bandgap value of around 1.6eV, much smaller than the 2.5eV of the δ phase, indicating a theoretical maximum efficiency of 25% [33]. This bandgap value is promising to the novel $FAPbI_3$ PSC design, which could not only act as a passivator to lower the thermodynamic energy of the system, but also as a new dopant to advance the photovoltaics, as has been done previously in their counterparts of $MAPbI_3$ [34].

The PCE measurements were thus conducted in the following step to explore the influence of the ε phase on the device performance. As shown in Fig. (3. 4a&b), the stability of the device has been increased by at least 10 times due to the ε phase. Under the 40RH% environment, the α dominated device lasted for 2 days, while the lifespan increased to more than 25 days after the conversion of the ε phase under the same

environment. Although the PCE dropped to 0.25% after the formation of the ε phase, it is attributed to the morphology change of the perovskite thin film, instead of the introduction of the ε phase. As demonstrated in Fig. (3. 4c&d), a large number of defects were generated after the conversion of the ε phase, which increased the resistance against the transfer of charge carriers, which may be avoided in the future extensive study by surface engineering or passivation method. Thus, the ε phase can be adopted as a powerful passivator or dopant [35–37], and the related surface/interface engineering details deserve expansion of the subject. Furthermore, the stability of the ε phase was maintained even in the vacuum when SEM was conducted, where the Gibbs free energy of such phase has been raised to a higher value by the environment, demonstrating that such phase is protected by kinetics as well. These findings indicate that the thermodynamic states could be manipulated by altering temperature and the water vapor pressure, which in return changes Ea of the phase transition. This means the α phase could directly be transformed into the ε phase at higher temperature and water vapor pressure, avoiding completely the formation of the undesirable δ phase, whose photovoltaic performance is less favorable. Moreover, the transition equilibrium among each phase could now be controlled, providing a new venue to fight against the instability issue and poor performance of the δ phase.

Summary

To summarize, a fresh structural maneuvering engineering method was proposed under the current materials framework by structural physics negotiation. The materials

properties have been successfully modified via relocating the secondary bonding of the perovskite, which altered the atomic structure. A unique strain engineering method has thus been developed based on the discovery, which tried to enlarge the unit cell of the FAPbI$_3$ perovskite to remove the internal strain to enhance the thermal/moisture stability, instead of controlling the annealing conditions that have been widely adopted previously. A novel structure of enhanced lifespan and comparable bandgap of the favorite α- FAPbI$_3$ has thus been synthesized, which provided not only thermodynamic but also kinetical warrant, extending the perovskite lifetime by more than 10-fold. Hopefully, these discoveries will be of help to the advance of the PSC design and materials research in general.

Reference

[1]   H. S. Kim, A. Hagfeldt, and N. G. Park, *Morphological and Compositional Progress in Halide Perovskite Solar Cells*, Chem. Commun. **55**, 1192 (2019).

[2]   National Renewable Energy Laboratory, *Best Research-Cell Efficiency Chart | Photovoltaic Research*, National Renewable Energy Laboratory.

[3]   A. F. Xu, N. Liu, F. Xie, T. Song, Y. Ma, P. Zhang, Y. Bai, Y. Li, Q. Chen, and G. Xu, *Promoting Thermodynamic and Kinetic Stabilities of Fa-Based Perovskite by an in Situ Bilayer Structure*, Nano Lett. **20**, 3864 (2020).

[4]   A. Kojima, K. Teshima, Y. Shirai, and T. Miyasaka, *Organometal Halide Perovskites as Visible-Light Sensitizers for Photovoltaic Cells*, J. Am. Chem. Soc. **131**, 6050 (2009).

[5]   J. Liang, C. Wang, Y. Wang, Z. Xu, Z. Lu, Y. Ma, H. Zhu, Y. Hu, C. Xiao, and X. Yi, *All-Inorganic Perovskite Solar Cells*, J. Am. Chem. Soc. **138**, 15829 (2016).

[6]   M. K. Assadi, S. Bakhoda, R. Saidur, and H. Hanaei, *Recent Progress in Perovskite Solar Cells*, Renewable and Sustainable Energy Reviews.

[7]   X. Zheng, C. Wu, S. K. Jha, Z. Li, K. Zhu, and S. Priya, *Improved Phase Stability of Formamidinium Lead Triiodide Perovskite by Strain Relaxation*, ACS Energy Lett. **1**, 1014 (2016).

[8]   M. T. Weller, O. J. Weber, J. M. Frost, and A. Walsh, *Cubic Perovskite Structure of Black Formamidinium Lead Iodide, α-[HC(NH2)2]PbI3, at 298 K*, J. Phys. Chem. Lett. **6**, 3209 (2015).

[9]   W. S. Yang, B. W. Park, E. H. Jung, N. J. Jeon, Y. C. Kim, D. U. Lee, S. S. Shin, J. Seo, E. K. Kim, J. H. Noh, and S. Il Seok, *Iodide Management in Formamidinium-Lead-Halide-Based Perovskite Layers for Efficient Solar Cells*, Science (80-.). **356**, 1376 (2017).

[10]   L. Gu, D. Zhang, M. Kam, Q. Zhang, S. Poddar, Y. Fu, X. Mo, and Z. Fan, *Significantly Improved Black Phase Stability of FAPbI3 Nanowires via Spatially Confined Vapor Phase Growth in Nanoporous Templates*, Nanoscale **10**, 15164 (2018).

[11]   H. Wang, C. Zhu, L. Liu, S. Ma, P. Liu, J. Wu, C. Shi, Q. Du, Y. Hao, S. Xiang, H. Chen, P. Chen, Y. Bai, H. Zhou, Y. Li, and Q. Chen, *Interfacial Residual Stress Relaxation in Perovskite Solar Cells with Improved Stability*, Adv. Mater. **31**, 1904408 (2019).

[12] C. Zhu, X. Niu, Y. Fu, N. Li, C. Hu, Y. Chen, X. He, G. Na, P. Liu, H. Zai, Y. Ge, Y. Lu, X. Ke, Y. Bai, S. Yang, P. Chen, Y. Li, M. Sui, L. Zhang, H. Zhou, and Q. Chen, *Strain Engineering in Perovskite Solar Cells and Its Impacts on Carrier Dynamics*, Nat. Commun. **10**, 1 (2019).

[13] J. Chen, J. Y. Seo, and N. G. Park, *Simultaneous Improvement of Photovoltaic Performance and Stability by In Situ Formation of 2D Perovskite at (FAPbI3)0.88(CsPbBr3)0.12/CuSCN Interface*, Adv. Energy Mater. **8**, 1702714 (2018).

[14] Z. Zhou, S. Pang, Z. Liu, H. Xu, and G. Cui, *Interface Engineering for High-Performance Perovskite Hybrid Solar Cells*, Journal of Materials Chemistry A.

[15] S. Wozny, M. Yang, A. M. Nardes, C. C. Mercado, S. Ferrere, M. O. Reese, W. Zhou, and K. Zhu, *Controlled Humidity Study on the Formation of Higher Efficiency Formamidinium Lead Triiodide-Based Solar Cells*, Chem. Mater. (2015).

[16] R. T. Wang, E. G. Tai, J. Y. Chen, G. Xu, R. LaPierre, N. I. Goktas, and N. Hu, *A KMnF3 Perovskite Structure with Improved Stability, Low Bandgap and High Transport Properties*, Ceram. Int. **45**, 64 (2019).

[17] R. T. Wang, A. F. Xu, L. W. Yang, J. Y. Chen, A. Kitai, and G. Xu, *Magnetic-Field-Induced Energy Bandgap Reduction of Perovskite KMnF3*, J. Mater. Chem. C **8**, 4164 (2020).

[18] A. F. Xu, R. T. Wang, L. W. Yang, V. Jarvis, J. F. Britten, and G. Xu, *Pyrrolidinium Lead Iodide from Crystallography: A New Perovskite with Low*

Bandgap and Good Water Resistance, Chem. Commun. **55**, 3251 (2019).

[19] A. F. Xu, R. T. Wang, L. W. Yang, N. Liu, Q. Chen, R. Lapierre, N. Isik Goktas, and G. Xu, *Pyrrolidinium Containing Perovskites with Thermal Stability and Water Resistance for Photovoltaics*, J. Mater. Chem. C **7**, 11104 (2019).

[20] A. D. Jodlowski, C. Roldán-Carmona, G. Grancini, M. Salado, M. Ralaiarisoa, S. Ahmad, N. Koch, L. Camacho, G. De Miguel, and M. K. Nazeeruddin, *Large Guanidinium Cation Mixed with Methylammonium in Lead Iodide Perovskites for 19% Efficient Solar Cells*, Nat. Energy **2**, 972 (2017).

[21] E. G. Tai, R. T. Wang, J. Y. Chen, and G. Xu, *A Water-Stable Organic-Inorganic Hybrid Perovskite for Solar Cells by Inorganic Passivation*, Crystals **9**, 83 (2019).

[22] R. T. Wang, E. E. Liu, A. F. Xu, L. W. Yang, J. Y. Chen, and G. Xu, *Ethylammonium Lead Iodide Formation in MAPbI3 Precursor Solutions by DMF Decomposition and Organic Cation Exchange Reaction*, Crystals **10**, 162 (2020).

[23] J. S. Yun, J. Kim, T. Young, R. J. Patterson, D. Kim, J. Seidel, S. Lim, M. A. Green, S. Huang, and A. Ho-Baillie, *Humidity-Induced Degradation via Grain Boundaries of HC(NH2)2PbI3 Planar Perovskite Solar Cells*, Adv. Funct. Mater. **28**, 1705363 (2018).

[24] A. M. A. Leguy, Y. Hu, M. Campoy-Quiles, M. I. Alonso, O. J. Weber, P. Azarhoosh, M. Van Schilfgaarde, M. T. Weller, T. Bein, J. Nelson, P. Docampo, and P. R. F. Barnes, *Reversible Hydration of CH3NH3PbI3 in Films, Single Crystals, and Solar Cells*, Chem. Mater. **27**, 3397 (2015).

[25] R. T. Wang, A. F. Xu, J. Y. Chen, L. W. Yang, G. Xu, V. Jarvis, and J. F. Britten, *Reversing Organic-Inorganic Hybrid Perovskite Degradation in Water via PH and Hydrogen Bonds*, J. Phys. Chem. Lett. **10**, 7245 (2019).

[26] T. Chen, B. J. Foley, C. Park, C. M. Brown, L. W. Harriger, J. Lee, J. Ruff, M. Yoon, J. J. Choi, and S. H. Lee, *Entropy-Driven Structural Transition and Kinetic Trapping in Formamidinium Lead Iodide Perovskite*, Sci. Adv. **2**, (2016).

[27] M. W. Chase, *NIST-JANEF Thermochemical Tables, Fourth Edition*, Journal of Physical Chemistry.

[28] L. Vinet and A. Zhedanov, *A "missing" Family of Classical Orthogonal Polynomials*, J. Phys. A Math. Theor. **44**, (2011).

[29] C. Berthomieu and R. Hienerwadel, *Fourier Transform Infrared (FTIR) Spectroscopy*, Photosynthesis Research.

[30] H. Buijs, *Infrared Spectroscopy*, in *Springer Handbooks* (2006), pp. 607–613.

[31] A. Sánchez-Coronilla, J. Navas, J. J. Gallardo, E. I. Martín, D. De Los Santos, N. C. Hernández, R. Alcántara, J. H. Toledo, and C. Fernández-Lorenzo, *Hybrid Perovskite, CH3NH3PbI3, for Solar Applications: An Experimental and Theoretical Analysis of Substitution in A and B Sites*, J. Nanomater. **2017**, (2017).

[32] A. Kaltzoglou, C. C. Stoumpos, A. G. Kontos, G. K. Manolis, K. Papadopoulos, K. G. Papadokostaki, V. Psycharis, C. C. Tang, Y. K. Jung, A. Walsh, M. G. Kanatzidis, and P. Falaras, *Trimethylsulfonium Lead Triiodide: An Air-Stable Hybrid Halide Perovskite*, Inorg. Chem. **56**, 6302 (2017).

[33] S. V. Boriskina and G. Chen, *Exceeding the Solar Cell Shockley-Queisser Limit*

via Thermal up-Conversion of Low-Energy Photons, Opt. Commun. **314**, 71 (2014).

[34] M. Li, H. Li, J. Fu, T. Liang, and W. Ma, *Recent Progress on the Stability of Perovskite Solar Cells in a Humid Environment*, J. Phys. Chem. C **124**, 27251 (2020).

[35] W. Luo, C. Wu, D. Wang, Y. Zhang, Z. Zhang, X. Qi, N. Zhu, X. Guo, B. Qu, L. Xiao, and Z. Chen, *Efficient and Stable Perovskite Solar Cell with High Open-Circuit Voltage by Dimensional Interface Modification*, ACS Appl. Mater. Interfaces **11**, 9149 (2019).

[36] L. Liu, S. Huang, Y. Lu, P. Liu, Y. Zhao, C. Shi, S. Zhang, J. Wu, H. Zhong, M. Sui, H. Zhou, H. Jin, Y. Li, and Q. Chen, *Grain-Boundary "Patches" by In Situ Conversion to Enhance Perovskite Solar Cells Stability*, Adv. Mater. **30**, (2018).

[37] L. Yangi, Y. Li, Y. Pei, J. Wang, H. Lin, and X. Li, *A Novel 2D Perovskite as Surface "Patches" for Efficient Flexible Perovskite Solar Cells*, J. Mater. Chem. A **8**, 7808 (2020).
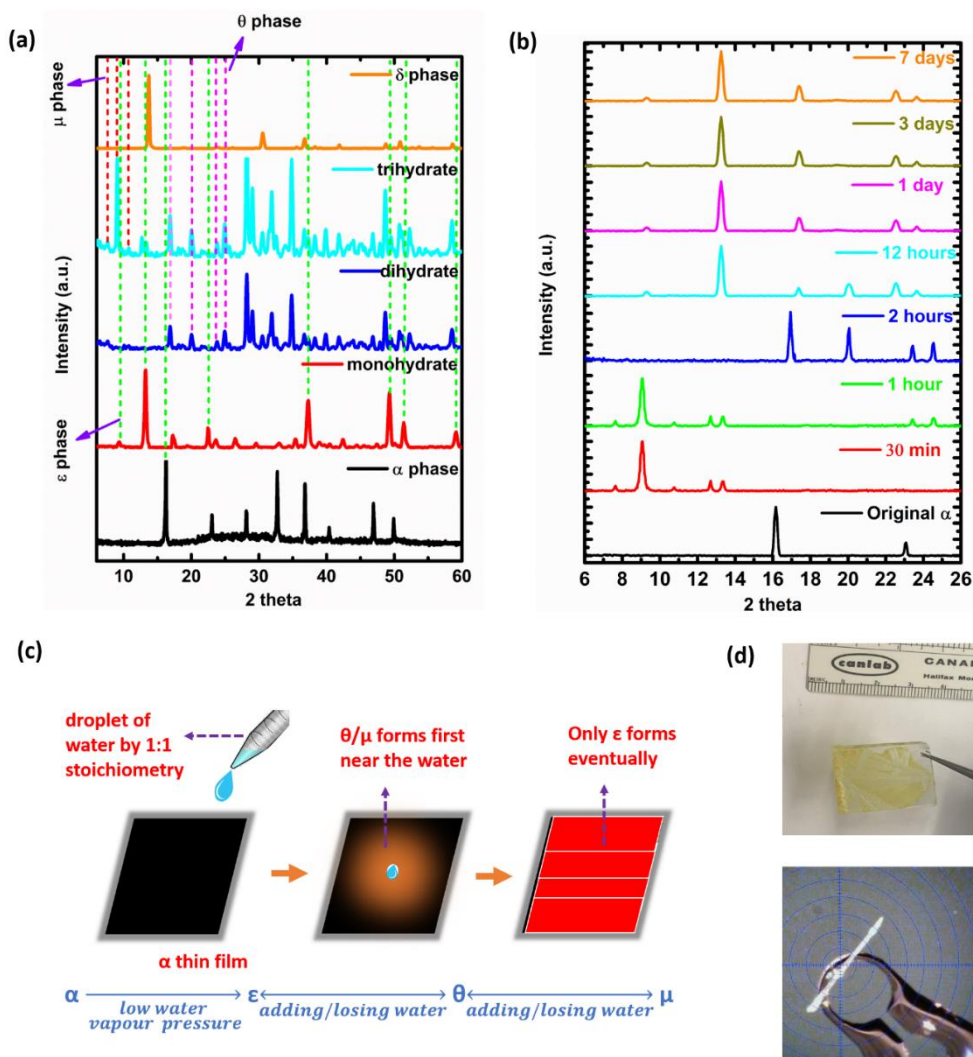
Figure 3. 1. (a) The XRD results of the ε/θ/μ phases. All the peaks of the ε phase are distinct and clear, unlike θ and μ phases. The θ and μ phases were synthesized by raising the molar ratio of water and FAPbI$_3$ to 2:1 and 3:1, respectively. Both phases would gradually lose water due to their thermodynamic states, leading to less distinct patterns. (b) the time-resolved XRD measurement results. (c) the schematic illustration of the conversion process of ε/θ/μ. (d) the real picture of the single crystal needle of ε.
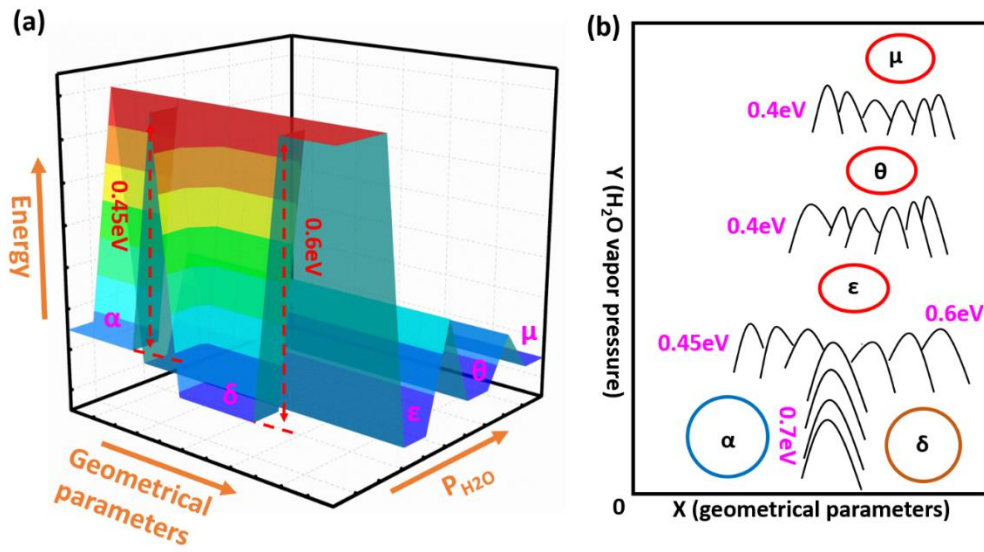
Figure 3. 2. (a) The 3D map that reveals the relationship of the thermodynamic and kinetic states of FAPbI₃ phases. (b) the corresponding 2D map.
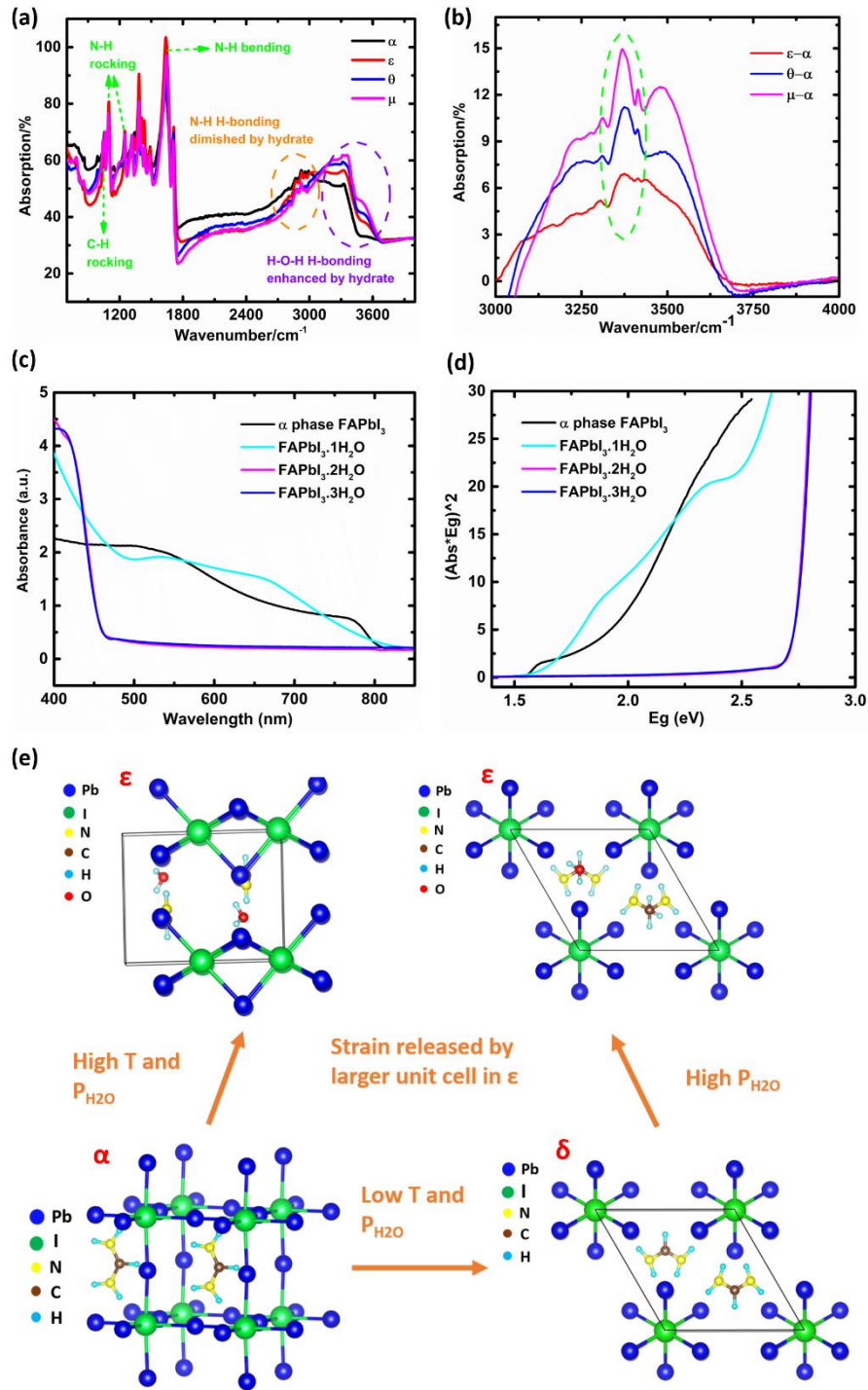
Figure 3. 3. (a) FTIR results of α and the hydrates. (b) FTIR signal of hydrates after baseline was extracted. (c&d) the bandgap measurement of α and the hydrates (determined by the Tauc plot). (e) the schematic illustration of the structural change caused by the phase transition.
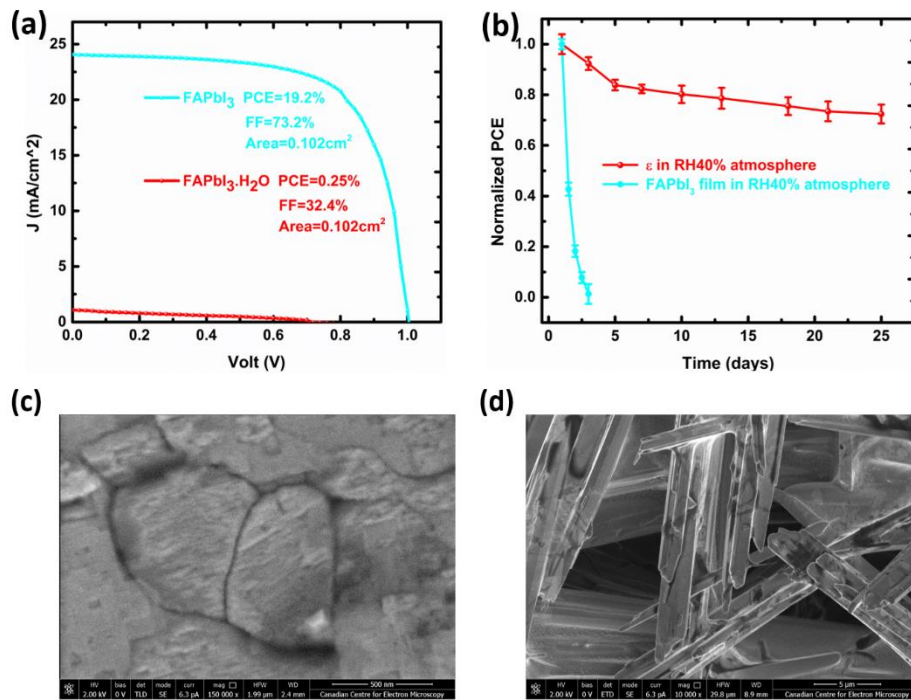
Figure 3. 4.   (a) the PCE measurements on α and ε based devices. (b) the stability measurements of the device in 40RH% environment. (c) the SEM morphology of α thin film, which showed little imperfection area and grain size of more than 500nm, ensuring the high PCE performance. (d) the SEM morphology of δ thin film, many defects were generated due to the enlarged unit cell size.

Chapter 4 EAPbI₃ formation in MAPbI₃ precursor solutions by DMF decomposition and organic cation exchange reaction

Author contributions: Ryan T. Wang conducted the experiments and wrote the manuscript. Elton E Liu, Alex F. Xu, and Lory W Yang conducted the SEM and XRD measurements. Jason Y Chen proofread the manuscript. Dr. Gu Xu provided the funding and overall supervision. All authors have read and agreed to the published version of the manuscript. This chapter has been published in Crystals, 2020.

Mysterious peaks have constantly been observed in the X-ray diffraction measurement for the $CH_3NH_3PbI_3$ film. Such mysteries have now been uncovered in this paper, where the powder X-ray diffraction, in-situ X-ray diffraction, and scanning electron microscopy measurements have been conducted, and these peaks were attributed to the ethylammonium lead iodide ($CH_3CH_2NH_3PbI_3$/$EAPbI_3$). It was found that the formation of $EAPbI_3$ was triggered by the breakdown of N, N-Dimethylformamide (DMF), which was adopted as the solvent in the preparation of the precursor solutions. $EAPbI_3$ was generated by the organic cation exchange reaction in the subsequent annealing process. A simple solution for this problem has been proposed in this paper as well, which would hopefully help the community to eradicate this impurity.

Introduction

The power conversion efficiency of $CH_3NH_3PbI_3$(MAPbI$_3$) and $HC(NH_2)_2PbI_3$ (FAPbI$_3$) perovskite solar cells has soared from 3.8 to 25.2% in the past decade [1,2], which now rivals that of other technologies such as silicon or cadmium telluride (CdTe) solar cells [3,4]. While such record performance seems to be inspiring for renewable energy development; the device lifetime, especially under moisture environment, remains at a low level, which prevents the commercialization. The devices usually degrade within a day unless an extra encapsulation layer is adopted [5,6] and even with the encapsulation layer the longest lifetime reported is still less than 4000 hours, which is far from enough for the commercialization [7–9].

Although various strategies have been proposed, such as doping at A, B, and X sites of the ABX_3 perovskite structure [10–12], grain boundary passivation [6,13,14], or replacing hydrophilic hole transport layer [15], none resolves the stability issue successfully. Therefore, uncovering the scientific mechanism of the decomposition is imperative to address this issue. Despite many mechanisms have been reported before [16–21]; they were often inconsistent and self-contradictory. Hopefully, some of the conflicts can be neutralized by our recently published work, where we revealed the importance of hydrogen bonding for the perovskite structural stability and discovered the true cause of the irreversible degradation [9]. However, there remains some mysterious substance detected during the synthesis of the $CH_3NH_3PbI_3$ thin film, which has yet to be identified by the perovskite solar cell community, despite similar phenomenon was also reported before elsewhere [22,23]. As the impurity could influence the device performance, and thus it calls for a systematic investigation.

It is, therefore, the purpose of the current article, to systematically investigate the mysterious substance, discovered in the perovskite thin film during the synthesis process, using powder X-ray diffraction (PXRD), in-situ X-ray diffraction, and scanning electron microscopy (SEM). We prepared various PbI_2 and CH_3NH_3I precursor solutions to investigate the influence of heating temperature and time on the $CH_3NH_3PbI_3$ thin film formation. It was discovered that N, N-Dimethylformamide (DMF) could decompose at a higher temperature, which enabled the organic cation

exchange reaction and lead to the formation of $CH_3CH_2NH_3I$ (EAI). Subsequently, EAI could react with PbI_2 and form $EAPbI_3$, which, as confirmed by the PXRD results, was identified to be the mysterious impurity presented in the $CH_3NH_3PbI_3$ perovskite film. The discovery is expected to help the community, to eliminate the $EAPbI_3$ impurities and to enhance the $CH_3NH_3PbI_3$ perovskite film morphology, thereby leading to a better device performance.

Experimental

Methanol (anhydrous, 99.8%) and N, N-Dimethylformamide (>99%) were purchased from Sigma-Aldrich. PbI_2 (>99.98%) and CH_3NH_3I (>99.98%, anhydrous) were purchased from Xi'an Polymer Light Technology Corp. PbI_2 and CH_3NH_3I precursor solutions were prepared by dissolving 1mmol CH_3NH_3I and PbI_2 in 1ml N, N-Dimethylformamide. Various dissolving temperature and stirring time were adopted, including 90°C/45min and 120°C/120min. $CH_3NH_3PbI_3$ was synthesized by spin-coating of CH_3NH_3I and PbI_2 solutions at 6000rpm on Fluorine-doped-Tin-Oxide glass substrate (composition: SiO_2/F; film thickness: 500 nm; bought from Huanan-Xiangcheng Tech Ltd), and next annealed at 90°C for 30min.

In-situ measurement was conducted on an enclosed chamber with vent tubes by Bruker D8 ADVANCE diffractometer. The thin film sample was mounted in a fully enclosed chamber. $CaSO_4$ (98% $CaSO_4$, 2% $CoCl_2$, anhydrous, purchased from McMaster chemical store) was also added in the chamber as desiccant, the lid was

tightly closed to ensure the saturation vapor pressure of methanol. In the in-situ XRD, measurement region of 24-26.5° was selected since the whole 2 theta range requires several hours for a single scan. The XRD measurement was repeated every 30 minutes for 3 days. Powder XRD was conducted with a Bruker D8 DISCOVER diffractometer; measurements were taken in the 2θ range of 10 to 76°. Diagram of the XRD chamber was shown in **Figure 4. 1**. SEM was done by FEI Magellan 400 XHRSEM. All diagrams were drawn in Origin9.0.
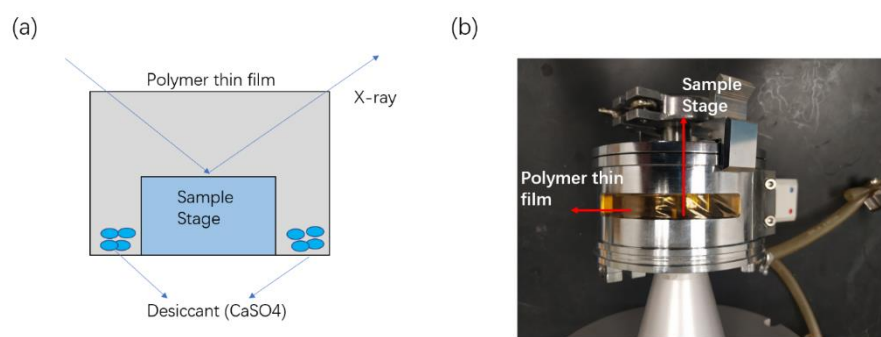
Figure 4. 1. (a)Schematic illustration of the XRD chamber; (b) photo of the chamber.

Results & Discussion

To identify the influence of the dissolving temperature and stirring time on the $CH_3NH_3PbI_3$ perovskite formation, both powder and in-situ XRD measurements were adopted in methanol and water environment. As circled in **Figure (4. 2a)**, $CH_3CH_2NH_3PbI_3$ (EAPbI$_3$) was detected when the precursor solutions were heated at 120°C for 2h; while such structure disappeared when the heating temperature and time were reduced to 90°C and 45min. The peaks for EAPbI$_3$ were also observed in the in-situ measurement, where a more controlled observation was conducted. As shown in

Figure (4. 2b), the peaks at 24.8° and 25.8° were attributed to EAPbI$_3$. This proved that

EAPbI$_3$ was generated gradually as time passing by, and we speculated that the solvent

(DMF) could be the cause of the EAPbI$_3$ formation as only DMF contains the structure

of ethylammonium.
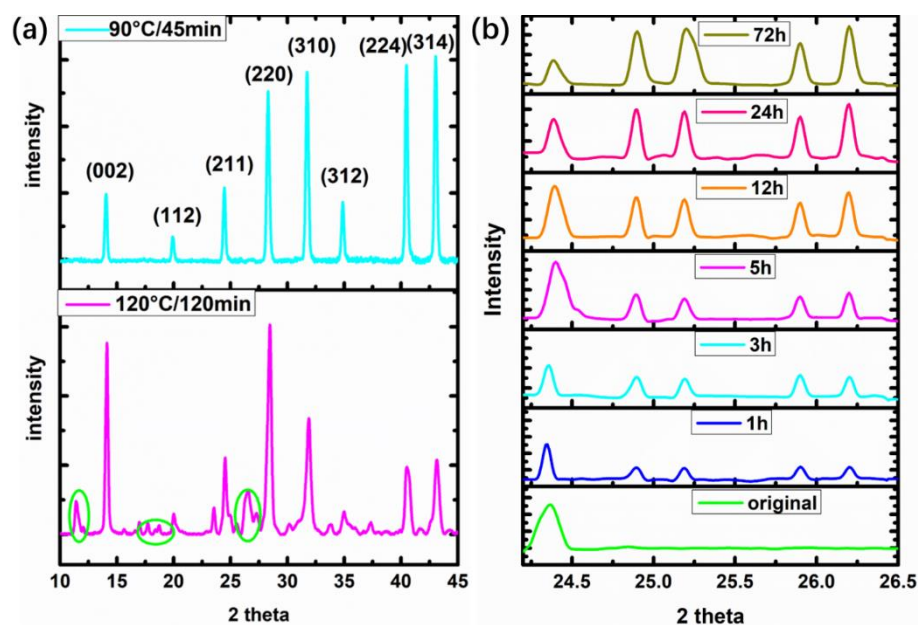
Figure 4. 2. (a)The results of XRD measurements for CH$_3$NH$_3$PbI$_3$ synthesized from

various precursor solutions, including 90°C/45min and 120°C/120min;(b) In-situ XRD

results of CH$_3$NH$_3$PbI$_3$ thin film under methanol environment.

In the subsequent analysis, we found the supporting evidence from the

literature, where the DMF was proved to be unstable at a temperature higher than 100°C

[24,25]. Therefore, DMF could be decomposed at higher heating temperature, starting

from the breakdown of the bond between the nitrogen atom and the carboxyl group,

generating ethylammonium ion intermediate, who reacted with CH$_3$NH$_3$I by organic

cation exchange reaction. Eventually, EAI was generated. In the following annealing

process, EAI reacted with PbI$_2$ to form EAPbI$_3$. Only weak peaks were observed for the first few hours in the XRD diagram, indicating a slow decomposition rate of DMF under heating. A schematic illustration of this process is shown in **Figure 4. 3**.
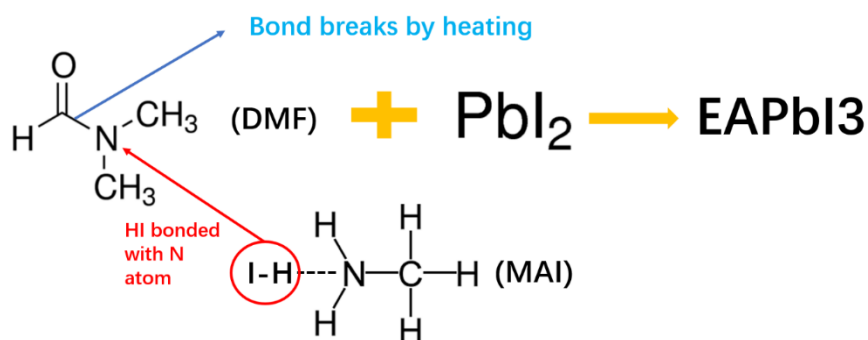
Figure 4. 3. Schematic illustration of EAPbI$_3$ formation process.

It is thus clear now, that the mysterious substance detected in the CH$_3$NH$_3$PbI$_3$ film is indeed EAPbI$_3$, which not only reduces the film purity, but also affects the film morphology, as can be confirmed in **Figure (4. 4a) & (4. 4b)**. When there was no EAPbI$_3$ present in the film, large CH$_3$NH$_3$PbI$_3$ grains could be observed with a size of several microns, as shown in **Figure (4. 4a)**; while such morphology changed greatly when EAPbI$_3$ was generated. In **Figure (4. 4b)**, the large grain was damaged, and voids were also generated, which proved that EAPbI$_3$ is detrimental for the CH$_3$NH$_3$PbI$_3$ film growth and device performance.
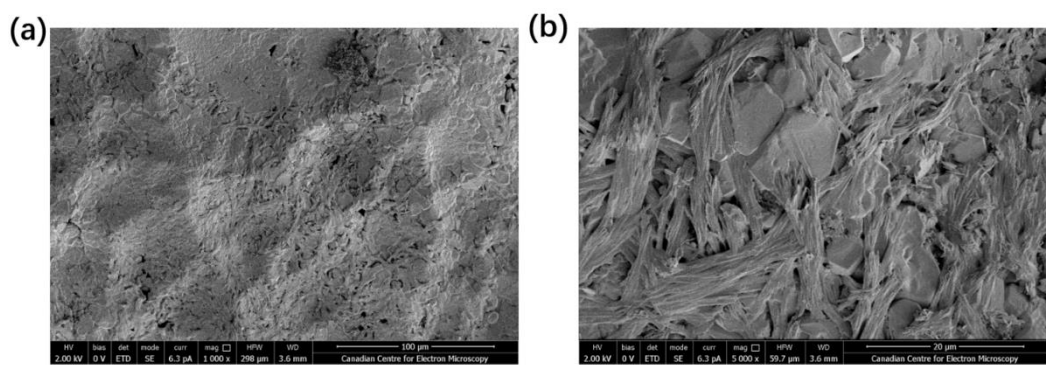
Figure 4. 4. (a) Morphology of $CH_3NH_3PbI_3$ film with no $EAPbI_3$; (b)Morphology of $CH_3NH_3PbI_3$ film with some $EAPbI_3$ impurities.

In summary, the formation of $EAPbI_3$ in the $CH_3NH_3PbI_3$ film is triggered by the degradation of DMF solvent, which is unstable at a higher temperature and decomposes into EA^+ intermediate. This is followed by an organic cation exchange reaction, where EA^+ switches position with MA^+, resulting in the formation of EAI, which subsequently reacts with PbI_2 in the following annealing process. Fortunately, the degradation rate of DMF is slow and the formation of $EAPbI_3$ can be avoided by reducing the heating time and temperature, during the preparation of the precursor solution.

Conclusion

In conclusion, the mysterious peaks detected by many others in the $CH_3NH_3PbI_3$ film have been successfully identified, and attributed to $EAPbI_3$, a perovskite that has a similar structure to $CH_3NH_3PbI_3$, which has been why it was so difficult to identify. The formation of $EAPbI_3$ in the $CH_3NH_3PbI_3$ film was found to be detrimental to the

grain growth, which could lower the power conversion efficiency. The $EAPbI_3$ could easily be eradicated by reducing the heating time and temperature when preparing the precursor solution. Hopefully, our discovery could be of immediate help to the community in the near future.

Reference

1. Matsui, T.; Yamamoto, T.; Nishihara, T.; Morisawa, R.; Yokoyama, T.; Sekiguchi, T.; Negami, T. Compositional Engineering for Thermally Stable, Highly Efficient Perovskite Solar Cells Exceeding 20% Power Conversion Efficiency with 85 °C/85% 1000 h Stability. Adv. Mater. 2019.

2. Kojima, A.; Teshima, K.; Shirai, Y.; Miyasaka, T. Organometal halide perovskites as visible-light sensitizers for photovoltaic cells. J. Am. Chem. Soc. 2009, 131, 6050–6051.

3. Wu, X. High-efficiency polycrystalline CdTe thin-film solar cells. Sol. Energy 2004.

4. Jellison, G.E.; Joshi, P.C. Crystalline silicon solar cells. In Springer Series in Optical Sciences; 2018.

5. Wang, R.T.; Tai, E.G.; Chen, J.Y.; Xu, G.; LaPierre, R.; Goktas, N.I.; Hu, N. A KMnF3 perovskite structure with improved stability, low bandgap and high transport properties. Ceram. Int. 2019, 45.

6. Tai, E.G.; Wang, R.T.; Chen, J.Y.; Xu, G. A Water-Stable Organic-Inorganic Hybrid

Perovskite for Solar Cells by Inorganic Passivation. Crystals 2019, 9, 83.

7. Xu, A.F.; Wang, R.T.; Yang, L.W.; Jarvis, V.; Britten, J.F.; Xu, G. Pyrrolidinium lead iodide from crystallography: A new perovskite with low bandgap and good water resistance. Chem. Commun. 2019, 55, 3251–3253.

8. Xu, A.F.; Wang, R.T.; Yang, W.; Xu, G.; Lapierre, R.; Isik Gaktas, N. Pyrrolidinium containing perovskites of thermal stability and water resistance for photovoltaics. J. Mater. Chem. C 2019.

9. Wang, R.T.; Xu, A.F.; Chen, J.Y.; Yang, L.W.; Xu, G.; Jarvis, V.; Britten, J.F. Reversing Organic-Inorganic Hybrid Perovskite Degradation in Water via pH and Hydrogen Bonds. J. Phys. Chem. Lett. 2019.

10. Ava, T.T.; Al Mamun, A.; Marsillac, S.; Namkoong, G. A review: thermal stability of methylammonium lead halide based perovskite solar cells. Appl. Sci. 2019, 9, 188.

11. Bai, X.; Zou, X.; Zhu, J.; Pei, Y.; Yang, Y.; Jin, W.; Chen, D. Effect of Rb doping on modulating grain shape and semiconductor properties of MAPbI3 perovskite layer. Mater. Lett. 2018, 211, 328–330.

12. Chang, J.; Chen, H.; Yuan, H.; Wang, B.; Chen, X. The mixing effect of organic cations on the structural, electronic and optical properties of FA x MA 1- x PbI 3 perovskites. Phys. Chem. Chem. Phys. 2018, 20, 941–950.

13. Huang, J.; Gu, Z.; Zuo, L.; Ye, T.; Chen, H. Morphology control of planar heterojunction perovskite solar cells with fluorinated PDI films as organic electron transport layer. Sol. Energy 2016.

14.   Gao, Y.; Wu, Y.; Lu, H.; Chen, C.; Liu, Y.; Bai, X.; Yang, L.; William, W.Y.; Dai, Q.; Zhang, Y. CsPbBr3 perovskite nanoparticles as additive for environmentally stable perovskite solar cells with 20.46% efficiency. Nano Energy 2019, 59, 517–526.

15.   Xiong, H.; Rui, Y.; Li, Y.; Zhang, Q.; Wang, H. Hydrophobic coating over a CH3NH3PbI3 absorbing layer towards air stable perovskite solar cells. J. Mater. Chem. C 2016.

16.   Yang, J.; Siempelkamp, B.D.; Liu, D.; Kelly, T.L. Investigation of CH3NH3PbI3degradation rates and mechanisms in controlled humidity environments using in situ techniques. ACS Nano 2015.

17.   Leguy, A.M.A.; Hu, Y.; Campoy-Quiles, M.; Alonso, M.I.; Weber, O.J.; Azarhoosh, P.; van Schilfgaarde, M.; Weller, M.T.; Bein, T.; Nelson, J.; et al. Reversible Hydration of CH3NH3PbI3 in Films, Single Crystals, and Solar Cells. Chem. Mater. 2014.

18.   Zhu, Z.; Hadjiev, V.G.; Rong, Y.; Guo, R.; Cao, B.; Tang, Z.; Qin, F.; Li, Y.; Wang, Y.; Hao, F.; et al. Interaction of Organic Cation with Water Molecule in Perovskite MAPbI3: From Dynamic Orientational Disorder to Hydrogen Bonding. Chem. Mater. 2016.

19.   Ahn, N.; Kwak, K.; Jang, M.S.; Yoon, H.; Lee, B.Y.; Lee, J.K.; Pikhitsa, P. V.; Byun, J.; Choi, M. Trapped charge-driven degradation of perovskite solar cells. Nat. Commun. 2016.

20.   Niu, G.; Li, W.; Meng, F.; Wang, L.; Dong, H.; Qiu, Y. Study on the stability of CH3NH3PbI3 films and the effect of post-modification by aluminum oxide in all-

solid-state hybrid solar cells. J. Mater. Chem. A 2014.

21.   Niu, G.; Guo, X.; Wang, L. Review of recent progress in chemical stability of perovskite solar cells. J. Mater. Chem. A 2015.

22.   Rajendra Kumar, G.; Dennyson Savariraj, A.; Karthick, S.N.; Selvam, S.; Balamuralitharan, B.; Kim, H.J.; Viswanathan, K.K.; Vijaykumar, M.; Prabakar, K. Phase transition kinetics and surface binding states of methylammonium lead iodide perovskite. Phys. Chem. Chem. Phys. 2016.

23.   Im, J.H.; Chung, J.; Kim, S.J.; Park, N.G. Synthesis, structure, and photovoltaic property of a nanocrystalline 2H perovskite-type novel sensitizer (CH3CH2NH3)PbI3. Nanoscale Res. Lett. 2012.

24.   Taft, R.W.; Abraham, M.H.; Doherty, R.M.; Kamlet, M.J. The molecular properties governing solubilities of organic nonelectrolytes in water. Nature 1985.

25.   Chadwick, S.S. Ullmann's Encyclopedia of Industrial Chemistry. Ref. Serv. Rev. 1988.

Chapter 5 Hysteresis and instability predicted in moisture degradation of perovskite solar cells

The degradation of perovskite solar cell structure was expected recently to be reversible, which opened a new gate to the enhancement of the device lifetime by the reversing process. However, the kinetic details of the structural collapse and recovery are still missing, without which the perovskite reversibility cannot be further explored. Due to the experimental difficulty, a purposeful numerical model was conducted in this report, to simulate the water diffusion process in the perovskite structure in both directions. It was found that the moisture diffusion needs to be initiated by a certain level of structural imperfection and is non-Fickian, as assisted by the collapse of the perovskite into the 1D chains. The reversibility was verified by the back diffusion, but accompanied by hysteresis, stagnancy, and even surprising instability, which initiated the water flow under initial equilibrium, due possibly to the imbalance during the reconstruction of the perovskite lattice. These observations offer new insight to form strategies of improvement, for example, via the possible self-healing perovskite devices.

Introduction

Perovskite solar cells have been hailed as a promising candidate to displace the existing energy harvesting technologies such as GaAs solar cells or Organic solar cells [1–3]. But the commercialization was held up by the fast degradation, especially under ubiquitous presence of moisture. The unencapsulated devices usually degraded within several hours [4–6]. Although such number can be enhanced to around 4000 hrs by encapsulation [7–9], it is still not enough to meet the requirement of practical applications [10,11].

Despite the extensive effort, the exact cause of moisture degradation of the perovskites remains debatable [12,13]. For example, $CH_3NH_3PbI_3$ was first found to be reactive in water, forming CH_3NH_2, HI, and PbI_2 after hydrolysis [12], but questioned by the discovery of the new phases detected during the degradation, which was attributed to the $CH_3NH_3PbI_3$ monohydrate and dihydrate [14]. The direct cause of the perovskite structural collapse was also predicted to the hydrogen bond breakdown [15,16]. The opposition party, on the other hand, believed that the whole $CH_3NH_3PbI_3$ degradation process was reversible in humid environment, except for the presence of ions such as N^+ or H^-, to distort the $CH_3NH_3PbI_3$ structure electrostatically [17], although, N^+ or H^- ions could hardly exist in water as they would react vigorously [18,19]. Eventually, a more complete description was offered recently, on what the real cause of the degradation might be [20]. It was discovered that CH_3NH_3I is stable in water and allows for the decomposition of $CH_3NH_3PbI_3$ to be reversible when annealed at higher temperature or drier condition. The finding not only confirms the importance of the hydration bonds to the perovskite structural stability, but also unravels that, the real cause of the irreversible degradation was OH^- in water, without which the perovskite structure could be reconstructed by thermal activation [20]. However, detailed kinetics is still missing [21,22], viz., questions remain, on the time evolution of the grain breakdown, as well as that of the possible recovery by the reverse transport of water molecules.

It is therefore the purpose of the current report, to elucidate the kinetic details of the perovskite grain degradation and reconstruction under the influence of water molecule

diffusion by modelling. As it is next to impossible to monitor the local variation of the hydrogen bonding status, it is necessary to construct a purposeful numerical model, to simulate the diffusion of water molecules and the resulting collapse of the hydrogen bonding of the perovskite lattice, which helps to understand the perovskite grain growth process involving lattice imperfection. The numerical simulation reveals that, the moisture diffusion need to be initiated by the structural imperfection above certain threshold, below which degradation happens slowly. But the diffusion is much accelerated as the perovskite structure opens up by the hydrogen debonding, leaving behind isolated pockets. On the other hand, the structure recovery has to follow the reverse diffusion, which presents a completely different profile, and accompanied by hysteresis and instability. It not only involves trapped areas by the collapsed structure, but also exhibits stagnancy due to imbalanced diffusion path. The latter could well be the cause of the astonishing observation of spontaneous flow of water molecules under initial equilibrium. The simulation results fill in the missing detail of the reversible degradation kinetics, which is not only of significance to the understanding of the recovery process, but also critical to the construction of stable perovskite solar cells.

Experimental

A two-dimensional lattice of 100x100 sites was employed throughout the simulation. The lattice size of the perovskite simulation work has been conveniently chosen, because various sample size has been investigated by the previous experimental works, where the results were found to be similar [23–27]. Each site represents the smallest

repeating part that constitutes grains or molecular sized part of perovskite single crystal. When one site collapses, it opens up diffusion path for water molecules, as opposed to the usual diffusion through vacancy or interstitials. The grain boundary has a similar function, which may be similarly described by this mechanism. To accommodate the unconventional diffusion, as the host lattice has been changing due to the structural degradation, which has been experimentally observed [28,29], and therefore it was built into the simulation axioms that, the connections are now assigned as variables (W) and will be updated, instead of an identical diffusivity bridging all the sites in the usual Fickian equation, each lattice point, which is associated with a value of water level, $P(x,y)$, has been connected by the probable paths to its left, right, upper and down, represented by $W(x,y,d=1\sim4)$, whose values will be updated during the actual moisture diffusion process. The P value of a given point is calculated with the master formula which incorporates the P and W values of its 4 neighbors (equation 1) [30]. The formula should show the relationships between all these values and how they contribute to the newly updated P for that point. The number of water molecule is increasing as time passing by as water molecules from the outside is constantly diffusing into the system. For example, 65% of the $W(x,y,d)$ may randomly be assigned initially by a value of 0.45, allowing the moisture diffusion to occur, due presumably to the existence of imperfection of the perovskite structure under variable temperature. The percentage can also be varied, to make comparison between the current study and the usual percolation threshold in two dimensions. The water level at site i (coordinate number (x,y)) is represented by P_i, which can be governed by the first-order rate equation:

$$\frac{dP_i}{dt} = \sum_j (P_j W_{ji} - P_i W_{ij}) \quad \text{(equation 1)}$$

The $W(x,y,d)$ will then be updated as the diffusion proceeds; when any $P(x,y)$ reaches 0.3 from zero of the beginning, its $W(left)$ or $W(right)$, with a 50/50 chance, is changed to 1.0, or 100% probable, simulating the partial breakdown of the perovskite; and when this $P(x,y)$ increases to 0.6, its $W(right)$ or $W(left)$ also becomes 1.0, leaving only $W(upper)$ and $W(down)$ to be intact, forming a vertically oriented 1D chain of PbI_2, simulating a collapsed perovskite, although in reality the diffusion may be more favourable along the chain direction. To show the possible directional effect, a boxed area was chosen near the centre of the lattice, in which the above update of the $W(left)/W(right)$, is switched to $W(upper)/W(down)$, such that the 1D PbI_2 chains are horizontally oriented within the boxed area.

To investigate the reversibility of the perovskite degradation, back diffusion of the water molecules is simulated by re-setting the boundary conditions. While the forward diffusion was driven by the zero initial $P(x,y)$, fixed boundary of $P(0,y) = P_0$ (e.g., 1.0), the reverse diffusion occurs when $P(x,y) = P_0$, and $P(0,y) = 0$, all under free boundary of $P(99,y) = P(100,y)$, and periodic boundary of $P(x,100) = P(x,0)$. In the meantime, the possible existence of the intermediate states, viz., when P stays in between the two extreme cases (e.g., 0.3~0.6) will be revealed by the coloured snapshots taken during the iterations from time to time.

Based on the scheme, a block diagram of the programming can be presented as scheme

1.

Results & Discussion

Following the recent discovery of the reversible water degradation by Wang et al [20], the

MAPbI$_3$ variation under moisture attack has been numerically simulated by a 2D lattice,

when a number of surprising observations were made, all originated from the fact that,

the diffusion paths have been kept changing by the water level of the site, represented

by the W(x,y,d) matrix variations as described in the programming above.

The results were best demonstrated by the time evolution of the water diffusion front,

as has been depicted by the snapshots of the whole lattice (**Figure. 5. 1**), where three

scenarios were compared; (**Figure. 5. 1a**), the W values were updated every time when

the P changes, which were also randomly assigned by nonzero values initially, where

the diffusion front was pushed towards the right hand side, but becoming more and

more irregular. In the meantime, there are pockets of unfilled blue left behind, and the

overall diffusion is not affected by the orientation of the 1D PbI$_2$ chains, as indicated

by the orange box in the middle; (**Figure. 5. 1b**) the usual Fickian diffusion, where all

W values were fixed by unity throughout the entire process, and a uniform diffusion

front can be obtained, although the central box is still highlighted by pink; (**Figure. 5.
1c**) a similar process to a), but without the W update, when the diffusion becomes much

slower, where some unusual behaviour can be found in the last frame, which will be

further explored below. To quantitatively describe the diffusion, the x coordinates were

averaged by P(x,y), via $<x^2>$, which is then plotted against the time steps (**Figure. 5. 1d**). The non Fickian diffusion of (1a) was displayed by the red curve, which is in sharp contrast to the normal Fickian diffusion of (1b) in black, where the path connecting the neighbouring sites are fixed by W= 1.0, as well as to the absence of W renewal of (1c) by blue line. The difference in nominal diffusivity can be obtained by the slope of the curves in the beginning, although it is due entirely to the choice of the diffusion path W, rather than the variation of the actual diffusion coefficients.

Since the W-update opens the moisture diffusion path when P reaches certain level, the initial random assignment of the non-zero W's was seemingly unnecessary. To our surprise, the diffusion could not even be executed without the random assignment, which is obviously related to the temperature influence (**Figure. 5. 2**), especially when the percentage is below 25% (**Figure. 5. 2a**), or 50% (**Figure. 5. 2b**). While the latter gives some advances, the former does not show any evidence of the water transport. As predicted by the general percolation theory, when the occupation probability below approximately 50% in 2D, or 30% in 3D [31,32], there is no way for water diffusion. However, the diffusion becomes possible once the initial non-zero W exceeds 50% (**Figure. 5. 2c, 5. 2d**), which reminds us of the well documented percolation threshold in 2D [33–35]. Such discoveries could also be echoed by the experimental observations, where perovskite stability was enhanced in the presence of moisture when the ion diffusion channel was suppressed [36], despite the fragile nature of $MAPbI_3$ in the presence of water [37]. Combining the results of (**Figure. 5. 1c**), it is apparent that, the

W-update, or collapse of the perovskite, only accelerates the diffusion, whereas the initial random assignment makes the continuous diffusion possible. This implies, the moisture degradation of the perovskite would not be originated, had there been no structural imperfection, which could also be proved by the stability of MAPbI$_3$ single crystals, which remained intact in the humid air for months [24]. From thermodynamics, diffusion takes energy, and the ratio of molecules meets the criteria is given by exp(-Ea/RT), where Ea represents the activation energy for water diffusion. Structural imperfection in general gives more free space for the water molecules to move, which reduces the activation energy, as opposed to a perfect crystal. However, once the diffusion path is established beyond the percolation threshold, it would cause phase transition to hexagonal structure, which enlarges the unit cell of perovskite [14], resulting in the formation of the 1D PbI$_2$ chains. This mismatch of the unit cell generates strains in the film and creates many structural imperfections, which created extra water paths. The degradation is thus accelerated, as can be confirmed by our modelling results and previous experimental observations [25,38].

As suggested by the recently discovery, the moisture degradation of the perovskite may be reversible [20], therefore the possibility of water back diffusion has to be simulated, when the left boundary of the lattice was set to zero, after the complete saturation of all the Ps (=1.0). The same W with initialization and P updates were implemented throughout the time iteration (**Figure. 5. 3a**). This is in sharp contrast to the second set of panels displaying the standard Fickian backward diffusion when all W are fixed at 1

(**Figure. 5. 3b**), and the final set showing the process nearly identical to the first, but

without the W update (**Figure. 5. 3c**). To analyze quantitatively, the usual graphic of

the $<x^2>$ is plotted against the iteration count (**Figure. 5. 3d**). However, in order to

make the comparison with that of the forward diffusion, the $<x^2>$ should be averaged

by (1-P), instead of P itself. This is due simply to the fact that, both P and (1-P) satisfy

the same 2nd order differential equation of the diffusion. Therefore, when the P becomes

the solution for the boundaries of the forward diffusion, (1-P) will be for the reverse

boundaries, which can be verified by the perfect match between the red and black lines,

representing the forward and backward processes of the Fickian diffusion, viz., when

W is fixed by unity. The flip side of this procedure is that, the $<x^2>$ is seemingly going

forward to become larger, rather than going backwards, as it should be. Surprisingly,

the resulting blue line is almost stagnant for the back-diffusion when W is updated,

although the water levels kept reducing, until most of the sites drop down to be less

than 0.3 (**Figure. 5. 3a**). In the meantime, within some area the diffusion seems to be

localized, or even become trapped in the area far away from the draining boundary

(**Figure. 5. 3c**), which is in total agreement with the experimental observations in the

literature [14], where the dehydration process is many times slower than the hydration.

Inspired by this stagnancy, more surprising results were obtained, when the diffusion

starts spontaneously even from complete equilibrium, viz., where all the P values were

initialized to 1, including the boundaries. All the W values were then assigned by either

0 or 1, to mimic the potential instabilities under the presence of 1D PbI_2 chains.

Astonishingly the water molecules start to move, when the iteration begins with W being updated (**Figure. 5. 4**). The water molecules gradually diffuse out even under equilibrium, without any driving force originated from the concentration gradient or difference, except for the possible imbalance of the diffusion paths in random fashion (**Figure. 5. 4a**). And the water molecules seem to stay, on the other hand, should such imbalance be regulated towards a certain orientation (**Figure. 5. 4b**).   While all this needs to be explored further, the overall process does not seem to be affected by the choice of the overall diffusion rate. This instability may also lead to the existence of intermediate states, the partial breakdown of the structure, when the moisture diffusion is halfway in between the beginning and saturation (0.3~0.6) and designated by green colour during the iterations. From nearly all the snapshots, especially of **Figure. 5. 3**, the green dotted areas were indeed observed in both forward **(Figure. 5. 4c left)** and back diffusion **(Figure. 5. 4c right)** process, indicating the possible intermediate states, which could not be shown otherwise.

Conclusion

To summarize, the well circulated perovskite solar cell structure has been numerically simulated to investigate its moisture degradation, an obstacle to the commercialization. Introducing the non-Fickian diffusion process, where the diffusion paths are updated constantly by the water level at each lattice site, we are able to show that, although the diffusion is much accelerated by the path updating, due possibly to the collapse of the 3D perovskite into the 1D PbI_2 chains, whose orientation is almost irrelevant, it

becomes impossible without the initial imperfection, represented by the random assignment of possible percolating route, below the threshold of which there would be no transport of water molecules. These discoveries proved the importance to reduce imperfection areas in the perovskite thin film, which helps to fight against the instability issue, as has been tested in the initial experiments [26,27,39]. More importantly, it uncovered the importance to consider the initial imperfections before conducting any simulation work, without which the result may become less reliable. Moreover, the moisture degradation is indeed reversible, when the lattice is exposed to the reversed boundary, but following a very different pattern from that of the forward diffusion. The result of stagnancy found in the back diffusion, has led to the discovery of possible spontaneous flow under equilibrium conditions, due to the distributed imbalance of the diffusion paths, which may become the source of the instability. Finally, these observations plus the evidence of intermediate states, may be extended to other diffusion processes, when the media is constantly influenced by the species transported.

FIGURES:
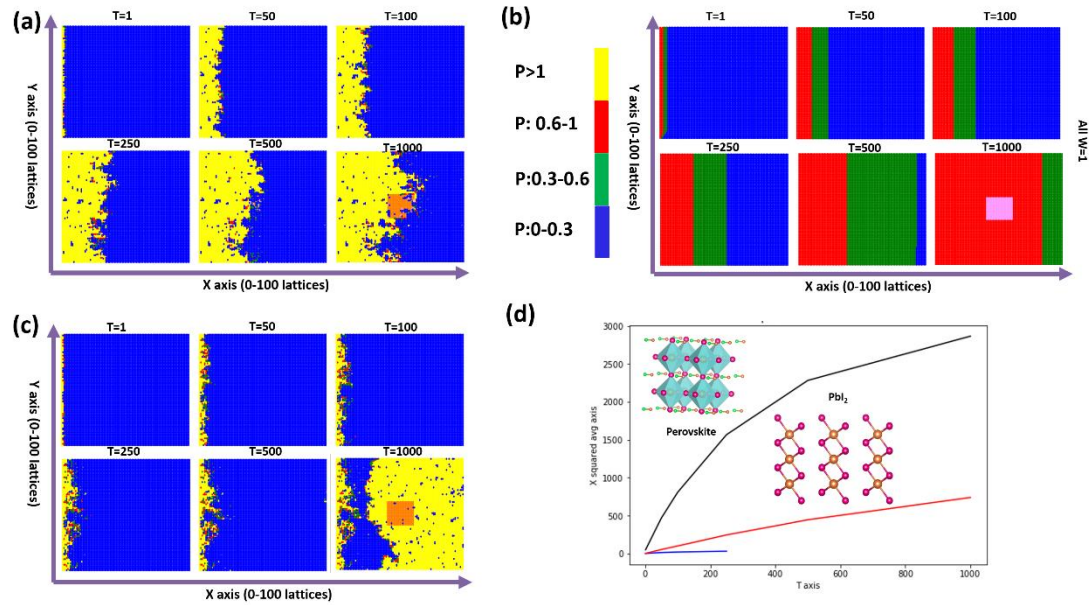
Figure 5. 1. Three types of forward diffusion are shown, where the forward diffusion means initializing all P values to be 0 with the exception of the left boundary, which is assigned a fixed number such as unity. In the first set of snapshots **(a)**, the W values were constantly updated based on the changes to the P values, which also had some randomly assigned nonzero values initially. The second set of snapshots is for the comparison to the usual Fickian diffusion **(b)**, where P values were initialized just as in the previous case, but all W values were fixed at 1 throughout the entire process. The final set of snapshots represents a similar process to the first, but the W does not get updated **(c)**, where some unexpected results were found when the iteration number grew higher. Lastly the graph shows the variation of the average value of x^2 with the number of iterations **(d)**, where the red line corresponds to the first set of snapshots, the black to the second, and the blue to the final set. The time steps are; 1, 50, 100, 250, 500, and 1000, for each consecutive panels, and the colour code for P values: 0~0.3, blue; 0.3~0.6, green; 0.6~1.0, red(pink); ≥1.0, yellow(orange) (within the central box). The fine

48

structure in each subplot shows the intermediated states during degradation process.

.
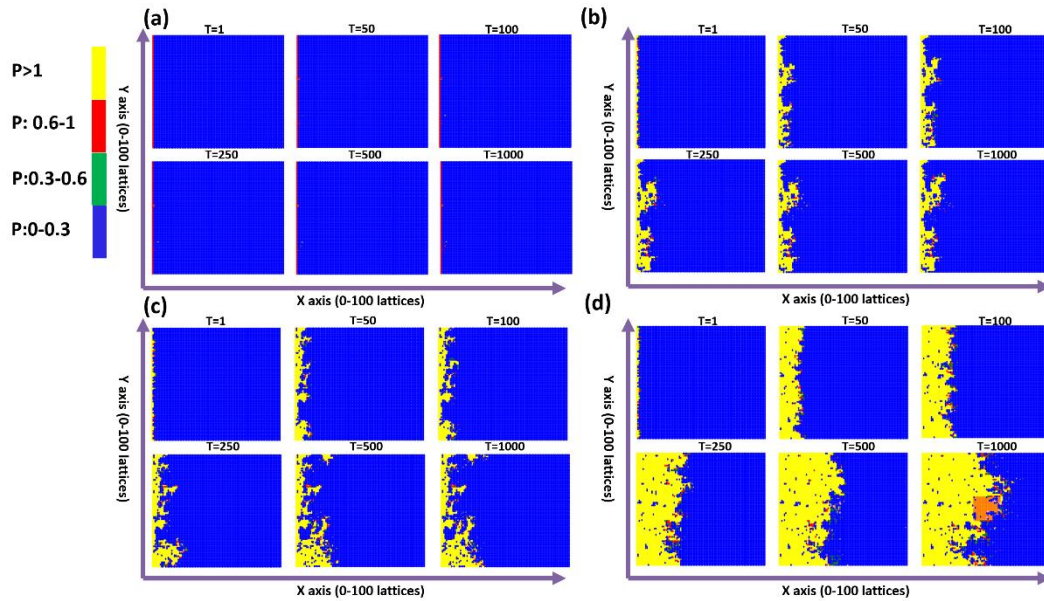
Figure 5. 2. The snapshots of the forward diffusion processes in which W is updated, but the initial percentage assignment of W values is varied. The probability of a given W being non-zero is varied from **(a)** 25%, **(b)** 49%, **(c)** 51%, and **(d)** 65%, respectively, in the figures. The results clearly show the percolation threshold in two-dimensional lattice persists, when it has to be greater than 50%, in order to sustain the diffusion process. The time steps are; 1, 50, 100, 250, 500, and 1000, for each consecutive panels, and the colour code for P values: 0~0.3, blue; 0.3~0.6, green; 0.6~1.0, red(pink); ≥1.0, yellow(orange) (within the central box).
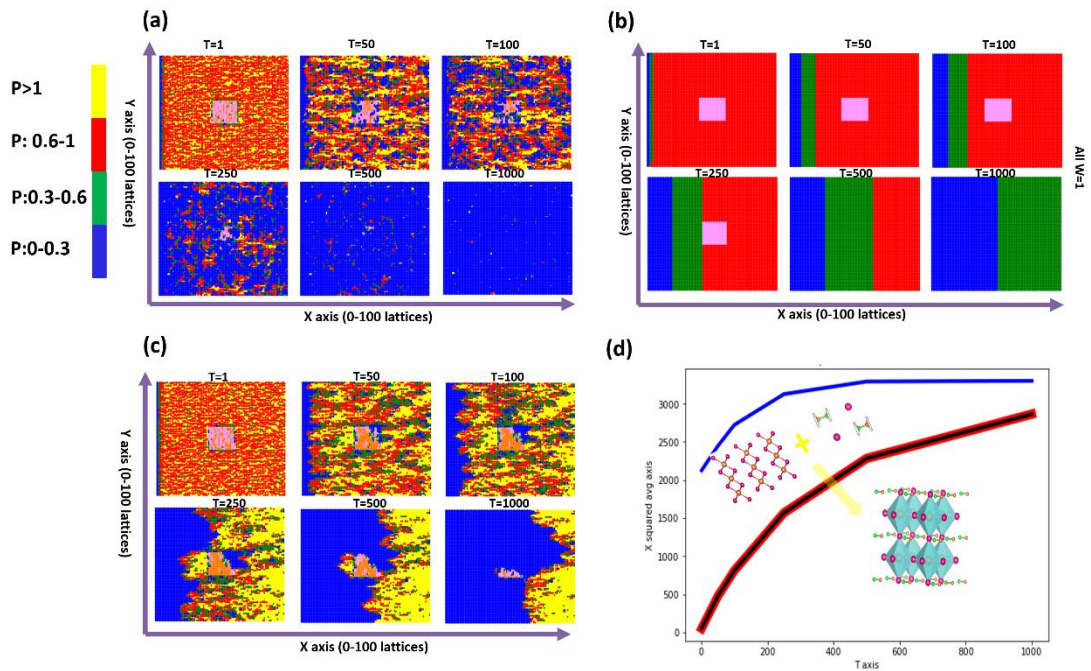
Figure 5. 3. The snapshots for the backwards diffusion processes, which are driven by P being initialized to 1 for all the points except the boundary, which is fixed at 0. The standard W and P update processes are run throughout the iteration. The first set shows the backward diffusion with W updates and randomly initialized W values **(a)**. The second set of figures shows the standard Fickian backward diffusion when all W are fixed at 1 **(b)**. The final set shows a process nearly identical to the first, but the W updates are non-random and fixed to certain orientations **(c)**. The graph plots the x^2 with the iteration count, averaged by (1-P) instead of P itself, the time-resolved zoomed-in image is available in Figure S1. **(d)**, in order to compare with that from the forward diffusion, which can be verified by the perfect match between the red and black lines, representing the forward and backward diffusion process for the Fickian process, viz.,

when W is fixed at 1. The blue line represents the back-diffusion scenario where W is updated randomly. The time steps are; 1, 50, 100, 250, 500, and 1000, for each consecutive panels, and the colour code for P values: 0~0.3, blue; 0.3~0.6, green; 0.6~1.0, red(pink); ≥1.0, yellow(orange) (within the central box).
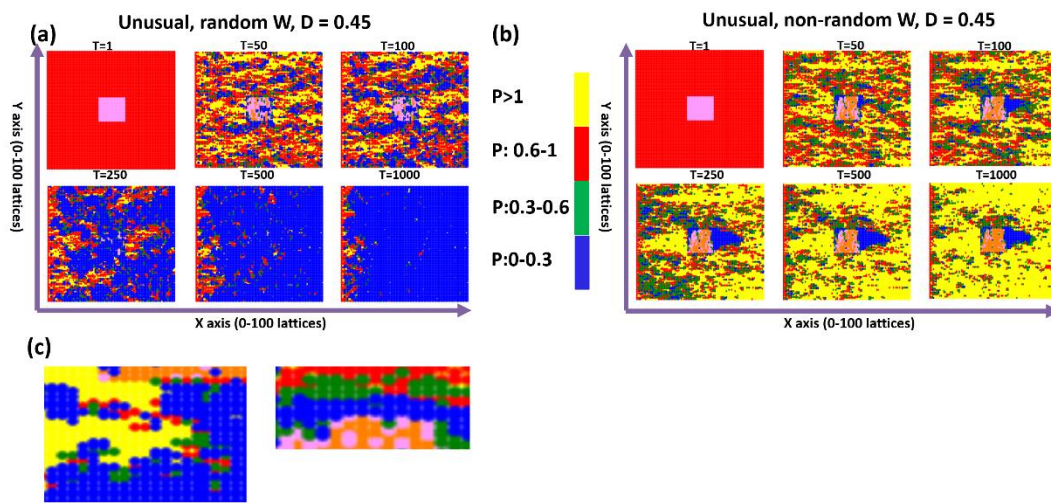
Figure 5. 4. The snapshots of trials, where all P values were initialized to 1, including the boundaries. All W values were then assigned either 0 or 1, to simulate the possible instabilities under the presence of 1D PbI_2 chains. W values were decided based on the orientations of the chains. For horizontally oriented chains (inside the center box), the northern and southern W values were set to 1 while the eastern and western values were set to 0. The vertically oriented chains simply switch the places of the 0s and 1s from the horizontal case. The update rule for (4a) would replace one of the W values equal to 1 with 0 should the P value fall between 0.3 and 0.6. All the horizontal chains would only have their northern or southern value changed from 1 to 0; the choice was uniform

across all points of the same chain type. In (4b), the program would randomly choose the northern or southern value to be changed by equal probability for both. The driving force for water to diffuse out is basic thermodynamic rules, which are to maximise the entropy of the whole system. While inside the central box, the chains are horizontally oriented, everywhere outside the box, the chains are vertically arranged. When the iterations were run with W being updated, surprising results are obtained, viz., water molecules start to diffuse out even under equilibrium **(a)**, or stay inside **(b)**, without any driving force originated from the concentration gradient or difference, except for the possible imbalance of the diffusion paths, the time-resolved zoomed-in image is available in Figure S2. The time steps are; 1, 50, 100, 250, 500, and 1000, for each consecutive panels, and the colour code for P values: 0~0.3, blue; 0.3~0.6, green; 0.6~1.0, red(pink); ≥1.0, yellow(orange) (within the central box). Also included is the evidence of the intermediate states, where the green dotted areas were indeed observed in both forward **(c)** and back diffusion process, signifying the possible kinetic states, which could not be proven otherwise.

SCHEMES

| Initialize P and W values based on the type of diffusion being simulated: One P value is assigned and an array of four W values corresponding to the 4 directions is assigned per point in the lattice. | → | Loop (run for 1000 iterations)

1. Update W values based on the policy for the given type of diffusion

2. Update P values using newly updated W values and master formula

3. At certain stages of the loop (i.e. iteration numbers 50, 100, 250, 500, and 1000), print a color map of the current state of the P values for each point in the lattice. Colors are coded by the ranges in which the P values lie in. | → | After outputting the color map of the state of the lattice at the 1000th iteration, write all the current W and P values to a .csv file

(This was done to get a clearer picture of the exact values at each point rather than just a color representation) |

Scheme 1. The modelling process of water diffusion.

Supporting Information.

Figure S5. 1. Time-resolved image for Figure 5. 4b: All the P values were initialized to 1, including the boundaries. All the W values were then assigned by either 0 or 1, to mimic the potential instabilities under the presence of 1D PbI_2 chains. These diagrams showed the time-resolved water diffusion process, which seemed to be frozen, should such imbalance be regulated towards a certain orientation.

Figure S5. 2. Time-resolved image for Figure 5. 4b: All the P values were initialized to 1, including the boundaries. All the W values were then assigned by either 0 or 1, to mimic the potential instabilities under the presence of 1D PbI_2 chains. These diagrams showed the time-resolved water diffusion process, which seemed to be frozen, should such imbalance be regulated towards a certain orientation.

Reference

(1) National Renewable Energy Laboratory. Best Research-Cell Efficiency Chart | Photovoltaic Research. National Renewable Energy Laboratory. 2019.

(2) Pitchaiya, S.; Natarajan, M.; Santhanam, A.; Asokan, V.; Yuvapragasam, A.; Madurai Ramakrishnan, V.; Palanisamy, S. E.; Sundaram, S.; Velauthapillai, D. A Review on the Classification of Organic/Inorganic/Carbonaceous Hole Transporting Materials for Perovskite Solar Cell Application. Arabian Journal of Chemistry. 2020, pp 2526–2557. https://doi.org/10.1016/j.arabjc.2018.06.006.

(3) Wang, R.; Mujahid, M.; Duan, Y.; Wang, Z. K.; Xue, J.; Yang, Y. A Review of Perovskites Solar Cell Stability. Advanced Functional Materials. 2019, p 1808843. https://doi.org/10.1002/adfm.201808843.

(4) O'keeffe, P., Catone, D., Paladini, A., Toschi, F., Turchini, S., Avaldi, L., Martelli, F., Agresti, A., Pescetelli, S., Del Rio Castillo, A.E. and Bonaccorso, F. Graphene-induced improvements of perovskite solar cell stability: effects on hot-carriers. Nano letters. 2019., 19(2), pp.684-691. https://doi.org/10.1021/acs.nanolett.8b03685.

(5) Long, M., Zhang, T., Zhu, H., Li, G., Wang, F., Guo, W., Chai, Y., Chen, W., Li, Q., Wong, K.S. and Xu, J. Textured CH3NH3PbI3 thin film with enhanced stability for high performance perovskite solar cells. Nano Energy. 2017., 33, pp.485-496.https://doi.org/10.1016/j.nanoen.2017.02.002.

(6) Bahadur, J.; Ghahremani, A. H.; Gupta, S.; Druffel, T.; Sunkara, M. K.; Pal, K. Enhanced Moisture Stability of MAPbI3 Perovskite Solar Cells through Barium Doping. Sol. Energy 2019, 190, 396–404.

https://doi.org/10.1016/j.solener.2019.08.033.

(7) Ava, T. T.; Al Mamun, A.; Marsillac, S.; Namkoong, G. A Review: Thermal Stability of Methylammonium Lead Halide Based Perovskite Solar Cells. Appl. Sci. 2019, 9 (1), 188. https://doi.org/10.3390/app9010188.

(8) Zhou, Y.; Hu, J.; Wu, Y.; Qing, R.; Zhang, C.; Xu, X.; Jiang, M. Review on Methods for Improving the Thermal and Ambient Stability of Perovskite Solar Cells. J. Photonics Energy 2019, 9 (04), 1. https://doi.org/10.1117/1.jpe.9.040901.

(9) Bisquert, J.; Juarez-Perez, E. J. The Causes of Degradation of Perovskite Solar Cells. Journal of Physical Chemistry Letters. 2019, pp 5889–5891. https://doi.org/10.1021/acs.jpclett.9b00613.

(10) Wang, H., Zhao, Y., Wang, Z., Liu, Y., Zhao, Z., Xu, G., Han, T.H., Lee, J.W., Chen, C., Bao, D. and Huang, Y. Hermetic seal for perovskite solar cells: An improved plasma enhanced atomic layer deposition encapsulation. Nano Energy 2020., 69, p.104375. https://doi.org/10.1016/j.nanoen.2019.104375.

(11) Uddin, A.; Upama, M. B.; Yi, H.; Duan, L. Encapsulation of Organic and Perovskite Solar Cells: A Review. Coatings. 2019, pp 9(2), 65. https://doi.org/10.3390/coatings9020065.

(12) Yang, J.; Siempelkamp, B. D.; Liu, D.; Kelly, T. L. Investigation of CH3NH3PbI3degradation Rates and Mechanisms in Controlled Humidity Environments Using in Situ Techniques. ACS Nano 2015, 9 (2), 1955–1963. https://doi.org/10.1021/nn506864k.

(13) Zhu, Z., Hadjiev, V.G., Rong, Y., Guo, R., Cao, B., Tang, Z., Qin, F., Li, Y.,

Wang, Y., Hao, F. and Venkatesan, S., Interaction of organic cation with water molecule in perovskite MAPbI3: from dynamic orientational disorder to hydrogen bonding. Chem. Mater. 2016., 28(20), pp.7385-7393. https://doi.org/10.1021/acs.chemmater.6b02883.

(14) Leguy, A.M., Hu, Y., Campoy-Quiles, M., Alonso, M.I., Weber, O.J., Azarhoosh, P., Van Schilfgaarde, M., Weller, M.T., Bein, T., Nelson, J. and Docampo, P., Reversible hydration of CH3NH3PbI3 in films, single crystals, and solar cells. Chem. Mater. 2015., 27(9), pp.3397-3407. https://doi.org/10.1021/acs.chemmater.5b00660.

(15) Niu, G.; Li, W.; Meng, F.; Wang, L.; Dong, H.; Qiu, Y. Study on the Stability of CH3NH3PbI3 Films and the Effect of Post-Modification by Aluminum Oxide in All-Solid-State Hybrid Solar Cells. J. Mater. Chem. A 2014, 2 (3), 705–710. https://doi.org/10.1039/c3ta13606j.

(16) Christians, J. A.; Miranda Herrera, P. A.; Kamat, P. V. Transformation of the Excited State and Photovoltaic Efficiency of CH3NH3PbI3 Perovskite upon Controlled Exposure to Humidified Air. J. Am. Chem. Soc. 2015, 137 (4), 1530–1538. https://doi.org/10.1021/ja511132a.

(17) Ahn, N.; Kwak, K.; Jang, M. S.; Yoon, H.; Lee, B. Y.; Lee, J. K.; Pikhitsa, P. V.; Byun, J.; Choi, M. Trapped Charge-Driven Degradation of Perovskite Solar Cells. Nat. Commun. 2016, 7 (1), 1–9. https://doi.org/10.1038/ncomms13422.

(18) Christe, K.; Wilson, W.; Sheehy, J.; Boatz, J. N5+: A Novel Homoleptic Polynitrogen Ion as a High Energy Density Material. Angew. Chemie Int. Ed. 2001, 40 (16), 2947–2947. https://doi.org/10.1002/1521-3773(20010817)40:163.0.CO;2-C.

(19)   Rau, A. R. P. The Negative Ion of Hydrogen. Journal of Astrophysics and Astronomy. 1996, pp 113–145. https://doi.org/10.1007/BF02702300.

(20)   Wang, R. T.; Xu, A. F.; Chen, J. Y.; Yang, L. W.; Xu, G.; Jarvis, V.; Britten, J. F. Reversing Organic-Inorganic Hybrid Perovskite Degradation in Water via PH and Hydrogen Bonds. J. Phys. Chem. Lett. 2019, 10 (22), 7245–7250. https://doi.org/10.1021/acs.jpclett.9b02972.

(21)   Yu, C.-J. Advances in Modelling and Simulation of Halide Perovskites for Solar Cell Applications. J. Phys. Energy 2019, 1 (2), 022001. https://doi.org/10.1088/2515-7655/aaf143.

(22)   Tessler, N.; Vaynzof, Y. Insights from Device Modeling of Perovskite Solar Cells. ACS Energy Letters. 2020, pp 1260–1270. https://doi.org/10.1021/acsenergylett.0c00172.

(23)   Battula, R. K.; Veerappan, G.; Bhyrappa, P.; Sudakar, C.; Ramasamy, E. Stability of MAPbI3perovskite Grown on Planar and Mesoporous Electron-Selective Contact by Inverse Temperature Crystallization. RSC Adv. 2020, 10 (51), 30767–30775. https://doi.org/10.1039/d0ra05590e.

(24)   M, P.; Predeep, P. Hybrid Perovskite Single Crystal with Extended Absorption Edge and Environmental Stability: Towards a Simple and Easy Synthesis Procedure. Mater. Chem. Phys. 2020, 239. https://doi.org/10.1016/j.matchemphys.2019.122084.

(25)   Schlipf, J.; Bießmann, L.; Oesinghaus, L.; Berger, E.; Metwalli, E.; Lercher, J. A.; Porcar, L.; Müller-Buschbaum, P. In Situ Monitoring the Uptake of Moisture into Hybrid Perovskite Thin Films. J. Phys. Chem. Lett. 2018.

https://doi.org/10.1021/acs.jpclett.8b00687.

(26)   Zhou, H.; Wang, J.; Wang, M.; Lin, S. Competing Dissolution Pathways and Ligand Passivation-Enhanced Interfacial Stability of Hybrid Perovskites with Liquid Water. ACS Appl. Mater. Interfaces 2020, 12 (20), 23584–23594. https://doi.org/10.1021/acsami.0c03532.

(27)   Caddeo, C.; Saba, M. I.; Meloni, S.; Filippetti, A.; Mattoni, A. Collective Molecular Mechanisms in the CH3NH3PbI3 Dissolution by Liquid Water. ACS Nano 2017, 11 (9), 9183–9190. https://doi.org/10.1021/acsnano.7b04116.

(28)   Chang, J.; Chen, H.; Yuan, H.; Wang, B.; Chen, X. The Mixing Effect of Organic Cations on the Structural, Electronic and Optical Properties of FAxMA1-XPbI3 Perovskites. Phys. Chem. Chem. Phys. 2018, 20 (2), 941–950. https://doi.org/10.1039/c7cp06608b.

(29)   Kim, H. S.; Hagfeldt, A.; Park, N. G. Morphological and Compositional Progress in Halide Perovskite Solar Cells. Chem. Commun. 2019, 55 (9), 1192–1200. https://doi.org/10.1039/c8cc08653b.

(30)   Chang, W.; Xu, G. Simulation of Ionic Diffusion in Solid Polymer Electrolytes with Correlated Chain Motion. J. Chem. Phys. 1993, 99 (3), 2001–2003.

(31)   Yoo, T. Y.; Tran, J.; Stahlheber, S. P.; Kaainoa, C. E.; Djepang, K.; Small, A. R. Site Percolation on Lattices with Low Average Coordination Numbers. J. Stat. Mech. Theory Exp. 2014, 2014 (6). https://doi.org/10.1088/1742-5468/2014/06/P06014.

(32)   Tran, J.; Yoo, T.; Stahlheber, S.; Small, A. Percolation Thresholds on Three-Dimensional Lattices with Three Nearest Neighbors. J. Stat. Mech. Theory Exp. 2013,

2013 (5). https://doi.org/10.1088/1742-5468/2013/05/P05014.

(33)   Stankovich, S.; Dikin, D. A.; Dommett, G. H. B.; Kohlhaas, K. M.; Zimney, E. J.; Stach, E. A.; Piner, R. D.; Nguyen, S. B. T.; Ruoff, R. S. Graphene-Based Composite Materials. Nature 2006, 442 (7100), 282–286. https://doi.org/10.1038/nature04969.

(34)   Chen, D., Pang, S., Zhu, W., Zhang, H., Zhou, L., He, F., Chang, J., Lin, Z., Xi, H., Zhang, J. and Zhang, C. Efficient Semitransparent Perovskite Solar Cells Using a Transparent Silver Electrode and Four-Terminal Perovskite/Silicon Tandem Device Exploration. Journal of Nanomaterials, 2018. https://doi.org/10.1155/2018/4012850.

(35)   Sarkar, A.; Rahaman, A. Bin; Chakraborty, K.; Pal, T.; Ghosh, S.; Banerjee, D. Organic Heterojunctions of Phthalocyanine-Reduced Graphene Oxide above Percolation Threshold for Photovoltaic Application. Mater. Chem. Phys. 2020, 253. https://doi.org/10.1016/j.matchemphys.2020.123418.

(36)   Schlipf, J.; Hu, Y.; Pratap, S.; Bießmann, L.; Hohn, N.; Porcar, L.; Bein, T.; Docampo, P.; Müller-Buschbaum, P. Shedding Light on the Moisture Stability of 3D/2D Hybrid Perovskite Heterojunction Thin Films. ACS Appl. Energy Mater. 2019, 2 (2), 1011–1018. https://doi.org/10.1021/acsaem.9b00005.

(37)   Zheng, C.; Rubel, O. Unraveling the Water Degradation Mechanism of CH3NH3PbI3. J. Phys. Chem. C 2019, 123 (32), 19385–19394. https://doi.org/10.1021/acs.jpcc.9b05516.

(38)   Yun, J. S.; Kim, J.; Young, T.; Patterson, R. J.; Kim, D.; Seidel, J.; Lim, S.; Green, M. A.; Huang, S.; Ho-Baillie, A. Humidity-Induced Degradation via Grain Boundaries of HC(NH2)2PbI3 Planar Perovskite Solar Cells. Adv. Funct. Mater. 2018,

28 (11), 1705363. https://doi.org/10.1002/adfm.201705363.

(39)   Tai, E. G.; Wang, R. T.; Chen, J. Y.; Xu, G. A Water-Stable Organic-Inorganic Hybrid Perovskite for Solar Cells by Inorganic Passivation. Crystals 2019, 9 (2), 83. https://doi.org/10.3390/cryst9020083.

Chapter 6 A KMnF₃ perovskite structure with improved stability, low bandgap and high transport properties

Here, a new promising perovskite structure of $KMnF_3$ has been fabricated and characterized, which yields bandgap of 1.6 eV with fascinating moisture-resistance and phase stability. Investigation of structural, optical, stability and transport properties have done by XRD, SEM, UV–vis–NIR spectroscopy, photoluminescence and electrical conductivity test. Such examination indicated the high carrier mobility (18 cm^2/V s) and density (10^{14}/cm^3) even after a long interval between each excitation. These transport properties are comparable to that of the organic perovskite, indicating the importance of $KMnF_3$ for solar device applications.

Introduction

Organic-inorganic hybrid perovskites, such as methylammonium lead iodide ($MAPbI_3$), have attracted much attention recently as light harvesting materials in photovoltaic devices due to its high-power conversion efficiency (PCE) (exceeding 22% in 2016) [1]. While such structure demonstrated great potential in practical applications, there are still challenges remaining which block the commercialization. Since the MAPbI3 firstly reported by Miyasaka, the stability of such structure has been extremely disappointing, especially under moisture attack [2], [3]. The major cause of the problem has been found to be the presence of methylammonium, which reacts with moisture and decomposes into HI and CH_3NH_2 [4]. Although various attempts have been made to improve the stability of the organic perovskite structure, including controlling the perovskite films morphology [5] encapsulation [6], [7], etc., none of these enhances successfully the lifetime beyond 1000 h. It is thus evident that, the organic ion A on the

ABX_3 is intrinsically unstable, and it seems very unlikely to apply organic perovskite in practice.

On the other hand, despite the stable performance in the moist environment (95% humidity), inorganic perovskite structures, such as $CsPbI_3$ by Liang et al., were found to phase transform at room temperature [8], which lower the PCE by enhancing the bandgap. Phase transformation could be eliminated using $CsPbBr_3$ [9], but its bandgap (2.3 eV) is still too large for practical application. This results in the challenge of reducing the bandgap, to improve the commercialization of inorganic perovskites.

To achieve the goal of a reducing bandgap, numerous structures have been tested by doping A, B and X ions, including Rb/$MAPbI_3$ [10], $FA_xMA_{1-x}PbI_3$ [11], $FASn/PbI_3$ [12], $CsPbI_2Br$ [13] etc. However, so far none of them offers a reduced bandgap to an appropriate level. This is simply caused by the fact that, people are only focusing by convention on the Groups of IA-IVA-VIIA elements or mixing between organics and Group IA-IVA-VIIA elements. This brings no intrinsic change to the structure and retains the inherent problem.

It is, therefore, the purpose of the current letter, to synthesize and characterize an optimal inorganic perovskite with reduced bandgap, by breaking off the convention and introducing $KMnF_3$. The same structure was studied before, for optical and magnetic properties [14], [15], [16], and its potential applications, on imaging and

sensing [17], [18], [19], [20], [21], but bearing little relevance to photovoltaics. Our results show that the chosen candidate of $KMnF_3$ presents great stability and excellent bandgap. The transport properties tests reveal surprisingly excellent carrier density and mobility. All this is successfully verified by experimental results, showing that $KMnF_3$ has excellent moisture resistance, a favorable bandgap of about 1.6 eV, and superb transport properties, 18 cm^2/V s in mobility and 10^{14}/cm^3 in density, ending hopefully the decade long-challenge.

Experimental

All the raw materials were purchased from Sigma-Aldrich™, including potassium fluoride (ACS reagent, $> = 99.0\%$) and Manganese(II) chloride (beads, 98%). One gram of $MnCl_2$ was ground into fine powders and then dissolved in 50 ml of DI water. Subsequently 5 ml of saturated KF water solution was added into the MnCl2 solution, then pink precipitate of $KMnF_3$ formed immediately. After 12 h of stirring, the precipitate was separated from the solution by suction filtration. The collected precipitate was then washed by 95% ethanol and dried in an oven at 60 °C for half an hour.

The sample was then subject to powder XRD, scanning electron microscope (SEM) and absorption spectrum bandgap test. A Bruker D8 DISCOVER diffractometer was used for Powder X-ray diffraction. Measurements were taken from 2θ values of 8–76° with a step length of 0.02°. A thin film sample coated on Fluorine-doped-Tin-Oxide glass

(composition: SiO_2/F; film thickness: 500 nm; bought from Huanan-Xiangcheng Tech LtD) was made by drop casting and annealing. The $KMnF_3$ powder is dissolved in Dimethylformamide first, and then the solution is drop casted on the surface of FTO glass, after which the glass is subject to annealing at 200 °C for 30 min. A comparison thin film sample was made using the same process at 320 °C and annealed for 1 h. The thin film of $KMnF_3$ is characterized by, FEI Magellan 400 XHR SEM, and then the thin film optical absorption measurements by Cary 5000 UV–vis–NIR Spectrophotometer, from 1200 nm to 200 nm. The bandgap was obtained by extrapolation of corresponding $(A*hv)2$ vs. energy (hv) curve of $KMnF_3$ film as described by Liang et al. [8].

The photoluminescence test is conducted by a tunable Ar-ion laser from Melles Griot (35LAP431208) at a power of 130 mW with a repetition rate of 50 Hz. Carrier density is calculated from the PL result using the method reported by Ref. [33]. The electrical conductivity is tested by Keithley 2450 Sourcemeter using a thin film sample, the film is coated on a non-conducting normal glass substrate, copper electrodes are used. And carrier mobility is given by electrical conductivity divided by the product of electron charge and carrier density.

Results and discussion

Based on the new strategy, a much better bandgap value has been obtained from $KMnF_3$, the contribution from the substrate is automatically subtracted by the spectrometer, and the absorption peak locates in 800 nm, as shown in Fig. 6. 1. $KMnF_3$ has an indirect

bandgap [22], a straightforward approach can be applied to estimate the bandgap via extrapolation of the (A * hv)2 vs. energy (hv) curve, yielding exciting interception at around 1.6 eV.
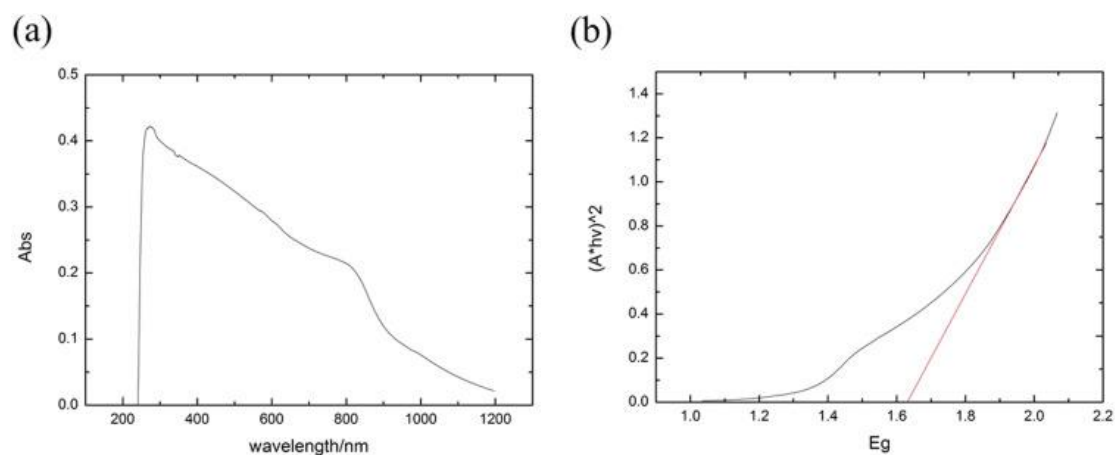
Figure 6. 1. (a) The absorbance spectrum of KMnF$_3$ solid thin film, and (b) the corresponding (A * hv)2 vs energy curve with the linear fit and extrapolation draw by Origin.

The bandgap result from absorption test is in line with the photoluminescence result as shown in Fig. 6. 2, which peaks in 700 nm. The charge carrier concentration is estimated by the method reported in Ref. [33]. The estimated charge carrier density is on the scale of 10^{14}/cm3. Although this result is lower than that reported in Ref. [33] which is on the scale of 10^{16}–10^{18}/cm^3, the low value of KMnF$_3$ sample is largely attributed to the low scanning rate and long interval between each scan, the scanning rate of our apparatus is 20 nm/s with 5 s interval, a large number of excited holes and electrons would be recombined within such a long period; while others are on the scale of mini, or even microseconds. Based on the measured carrier density and electrical resistance, the calculated carrier mobility is found to be around 18 cm^2/V s.

This is comparative to other types of perovskite, as indicated in the table below (Table 6.1, Table 6.2, Table 6.3, Table 6.4).
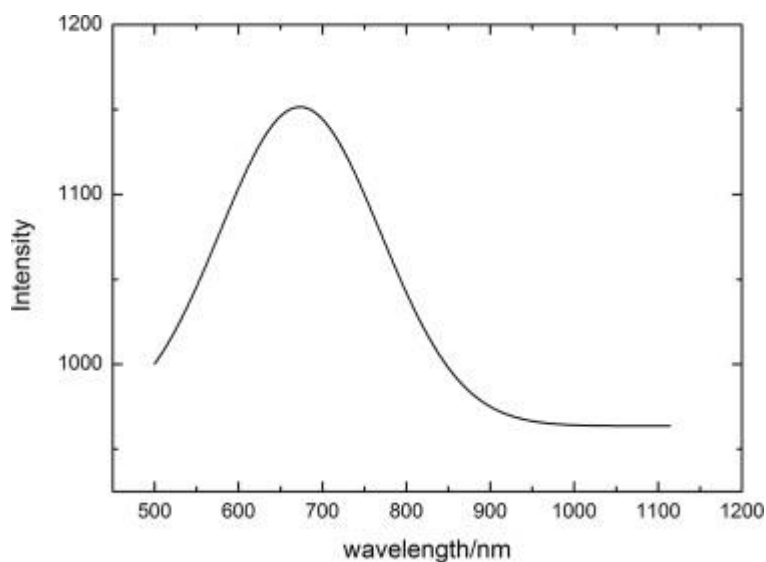
Figure 6. 2.   PL test curve.

Table 6. 1. Comparison of carrier mobility in various references

Sample	Architecture	Electron, hole, sum	Mobility $cm^2/(V\,s)$
MAPbI$_3$ [34]	film	Σ	71
MAPbI$_3$ [35]	film	Σ	20
MAPbI$_3$ [36]	film	e	1.4
MAPbI$_3$ [36]	film	h	0.9
MAPbI$_3$ [37]	film	Σ	9
KMnF$_3$	film	Σ	18

Table 6. 2. Crystal data for $KMnF_3$.

Chemical formula	$KMnF_3$
Crystal System	Cubic
Space group	$P3mm$
a (Å)	4.19

Table 6. 3. Comparison of TF between $KMnF_3$ and $MAPbI_3$.

Sample	TF
$KMnF_3$	0.972
$MAPbI_3$	0.912
Optimum range	0.812–1.106

Table 6. 4. Comparison of the octahedral factor between $KMnF_3$ and $MAPbI_3$.

Sample	OF
$KMnF_3$	0.624
$MAPbI_3$	0.541
Optimum range	0.441–0.894

In the meantime, XRD has to be employed to study the structural and compositional

change under the influence of water, as has been done by many others [4], [7], [8], [38].

Following the practice of the literature for perovskite stability study [8], [9], [25], the

water immersion test has been conducted. The organic perovskite structure reported by

others generated new peaks in XRD pattern after being placed in the humid

environment for several hours, indicating the decomposition of the perovskite. However,

our sample kept its original crystal structure, a simple cubic with space group *P3mm*,

even after water immersion for 12 h, as shown in Fig. 6. 3, demonstrating that our

structure is much more moisture-resistant. All this verifies not only the chemical

stability but also the phase stability of $KMnF_3$, which has not been achieved by

previously reported perovskite structure, such as $MAPbI_3$ or $CsPbI_3$ [7], [8], [23].
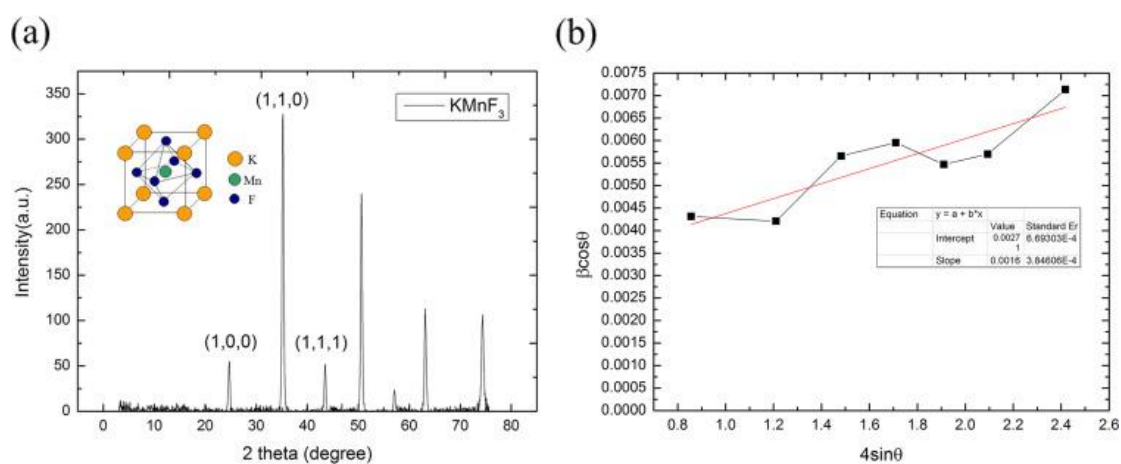
Figure 6. 3. (a) XRD results of $KMnF_3$ after immersing in water for more than 12 h; (b) Williamson-Hall plot.

The average crystallite size of the as-synthesized sample powder was estimated by the

XRD pattern. The Williamson-Hall equation was used:

$\beta_{hkl}=(K\lambda/d)+(4\epsilon\sin\theta)$

where λ is wavelength of the incident X-ray, d is the crystallite size, β_{hkl} is half peak width of corresponding (*hkl*) plane, K is a constant which often equals to 0.94, ϵ is strain and θ is brag angle. The average crystallite size of the as-synthesized powder obtained from the Williamson-Hall plot is 62.3 nm. A film was manufactured by drop casting and annealing and subjected to SEM characterization. From the observation of SEM, the size of the particles after 30 min annealing varies from 0.1 to 1 µm. It shows aggregating large cubic morphology with some larger particles devouring small ones. When annealing at a higher temperature (320 °C) and longer time (1 h), the size distribution gets homogenized, most of the cubes are sized at about 0.1 µm (Fig. 6. 4, Fig. 6. 5).
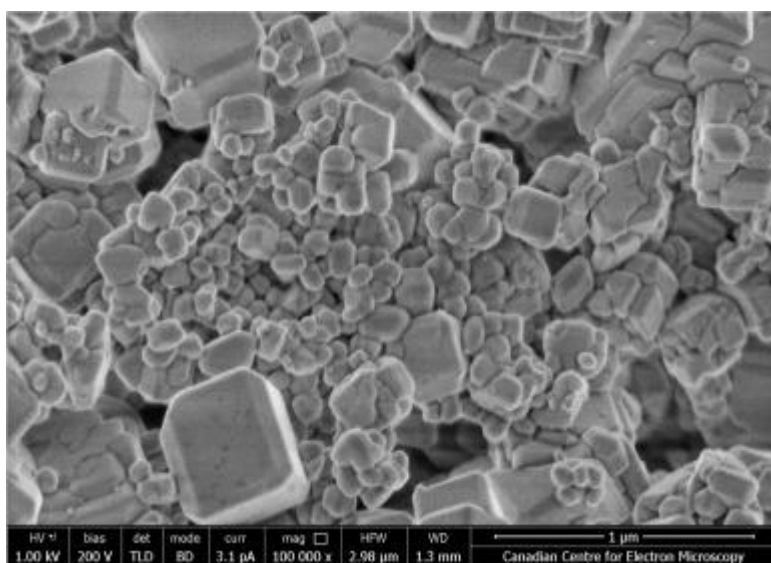
Figure 6. 4. SEM image shows larger crystals dispersed on the surface (200 °C, 30 min annealing time).
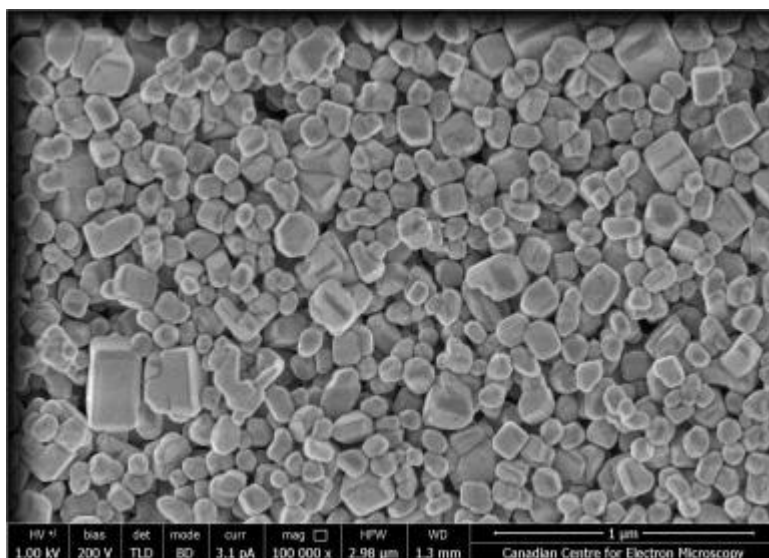
Figure 6. 5. SEM image shows homogenized crystals dispersed on the surface (320 °C, 1 h annealing time).

This seemingly trivial step beyond the conventional IA-IVA-VIIA group elements for the inorganic perovskite for solar cell can be traced back to the days when organic perovskite was firstly reported. In the original ABX_3 structure, B and X sites are occupied by IVA-VIIA group elements, such as Pb/Sn, and I/Br. Greatly influenced by these works, the inorganic solar cell perovskite has also been using IVA-VIIA group elements to fill B and X sites, an understandable psychological inertia. However, not much improvement has been achieved, even though almost all IVA-VIIA group element combinations have already been exhausted. The unsuccessful attempts prompt us to give up on the IVA-VIIA group elements in solar cell design, as they may not work for our purposes. Inspired by the original structure of inorganic perovskite ore, we found that, it is possible to employ other group elements to fit B and X sites. Instead of focusing on the organic or organic-inorganic hybrid, we searched beyond the solar cell

literature, and eventually reached the structure of having K, Mn, and F to fit A, B, and X sites of perovskite, respectively, which offers a reduced bandgap.

The choice of the elements has profound materials implications, not least of which is the large difference in the electronegativity among K, Mn, and F ions, which favors the chemical stability. Another important facet is the relative size differences among K, Mn and F ions. Such a relationship has been described by tolerance factor (TF). The TF values of $KMnF_3$ predictably located in the optimum range, which contributes to the stability of the perovskite structure [24], [25], [28].

The importance of TF values can be judged by the fact that, it is correlated directly to the physical stability, which influences the structural lifetime. Ideally, the TF should be found within 0.812–1.106 [26]. For perovskite with TF < 0.8, the structure would be transformed into NH_4CdCl_3-type, which implies that A ion size is too small to hold the PbX_6 octahedral, so the structure collapses; for the perovskite of TF > 1, the 3D structure is no longer in favor, 1D or 2D structure will then be formed instead [29]. Overall, a large A cation will favor a stable perovskite structure; but an oversized A cation will crumble the perovskite structure, transformed to 1D or 2D structure and hence increases the bandgap of such perovskite structure. The relative sizes of K, Mn and F ions decide whether K+ can be fitted into MnF6 octahedral, thus gives excellent stability.

Although $KMnF_3$ was once synthesized as an antiferromagnetic material [24], which

was perhaps why it has been distinguished from other inorganic perovskites, its antiferromagnetic properties may not be related to its photoluminescence, as the latter is determined by the bandgap. A more related point, however, could be the structure of $KMnF_3$ itself, where both B and X sites are modified to accommodate the smaller size of inorganic A ion. This gives $KMnF_3$ an outstanding octahedral factor value, which is given by the ratio of effective ionic radii of B and X ions, which is directly reflected in the bandgap engineering [24], [29], [30].

More specifically, among the 4 factors that affect bandgap, including effective electronegativity difference between the B cations and X anions; electronegativity of X site anions; dimensionality of the BX_6 network (influenced by TF); and the angle of the B–X–B bonds (influenced by OF), the last one has the biggest effect which can be directly tuned by OF [31]. The usual alkaline metal lead halide perovskite has a small OF which tilts the BX_6 network, and increases the B-X-B angle, resulting in a larger bandgap. In our case, however, the selected $KMnF_3$ has a larger OF to increase the B-X-B bond angle, leading to a much smaller bandgap than all other inorganic perovskite structure reported in photovoltaics, a direct application of the bandgap engineering strategy. All this has indeed been verified by the experiments, when we have successfully achieved the low bandgap, while maintaining the stability at the same time.

Summary

To summarize, we have found an inorganic perovskite structure with both great stability, reduced bandgap value and high transport properties. The formation and characteristics

of such structure are theoretically studied, using a simple solution processing method followed by an investigation of structural, optical, stability and transport properties. XRD and SEM results prove the powder synthesized is in the form of nanoparticles with an average crystallite size of around 60 nm. Powder XRD pattern shows the resulting $KMnF_3$ is moisture-resistant. The absorption spectrum shows its bandgap of around 1.6 eV. Photoluminescence and electrical conductivity test indicates a comparable transport property to the highly-efficient organic perovskite structure. With the possible further development, KMnF3 will be of great potential to replace the existing perovskite structures for solar cell application, with both the required stability and desired PCE, and to form the solution to the renewable energy soon.

References

[1] M. Saliba, et al. Incorporation of rubidium cations into perovskite solar cells improves photovoltaic performance Science, 354 (6309) (2016), pp. 206-209

[2] A. Kojima, K. Teshima, Y. Shirai, T. Miyasaka Organometal halide perovskites as visible-light sensitizers for photovoltaic cells J. Am. Chem. Soc., 131 (17) (2009), pp. 6050-6051

[3] G. Tang, et al. Revealing the role of thiocyanate anion in layered hybrid halide perovskite (CH3NH3)2Pb (SCN)2I2 J. Chem. Phys., 146 (22) (2017), p. 224702

[4] F. Jafarzadeh, S. Javadpour, M.H. Shariat Fabrication and investigation of a new highly humidity stable nanocrystalline perovskite, tetramethylammonium-lead-triiodide to be used in solar cells Ceram. Int., 43 (15) (2017), pp. 11552-11555

[5] S. Wang, et al. Construction of nanowire CH3NH3PbI3-based solar cells with 17.62% efficiency by solvent etching technique Sol. Energy Mater. Sol. Cells, 167 (2017), pp. 173-177

[6] A.L. Palma, et al. Reduced graphene oxide as efficient and stable hole transporting material in mesoscopic perovskite solar cells Nano Energy, 22 (2016), pp. 349-360

[7] N.H. Tiep, Z. Ku, H.J. Fan Recent advances in improving the stability of perovskite solar cells Adv. Energy Mater., 6 (2016), p. 3

[8] J. Liang, et al. All-inorganic perovskite solar cells J. Am. Chem. Soc., 138 (49) (2016), pp. 15829-15832

[9] X. Chang, et al. Carbon-based CsPbBr3 perovskite solar cells: all-ambient processes and high thermal stability ACS Appl. Mater. Interfaces, 8 (49) (2016), pp. 33649-33655

[10] X. Bai, et al. Effect of Rb doping on modulating grain shape and semiconductor properties of MAPbI3 perovskite layer Mater. Lett., 211 (2018), pp. 328-330

[11] J. Chang, et al. The mixing effect of organic cations on the structural, electronic and optical properties of FAxMA1− x PbI3 perovskites Phys. Chem. Chem. Phys., 20 (2) (2018), pp. 941-950

[12] S. Shao, et al. Highly reproducible Sn-based hybrid perovskite solar cells with 9% efficiency Adv. Energy Mater. (2017)

[13] S. Mariotti, et al. Stability and performance of CsPbI2Br thin films and solar cell devices ACS Appl. Mater. Interfaces (2018)

[14] Z. Celinski, et al. Exchange biasing in ferromagnet/antiferromagnet Fe/KMnF3 J. Magn. Magn. Mater., 202 (2–3) (1999), pp. 480-484

[15] L.-N. Hao, K. Liu, S. Cheng, Y. Wang, Y.-J. Xu, H.-S. Qian KMnF3 nanowires and nanoparticles: selected synthesis, characterization and magnetic properties Mater. Lett., 196 (2017), pp. 145-148

[16] S.A. Kizhaev, L.A. Markova Structural and magnetic phase transitions in KMnF3 Phys. Solid State, 53 (9) (2011), p. 1851

[17] M. Carpenter, E. Salje, C.J. Howard Magnetoelastic coupling and multiferroic ferroelastic/magnetic phase transitions in the perovskite KMnF3 Phys. Rev. B, 85 (22) (2012), p. 224430

[18] M. Ding, M. Xu, C. Lu, J. Xi, Z. Ji, D. Chen 808 nm NIR light excited single-band red upconversion emission in lanthanide-doped KMnF3 nanocrystals J. Alloy. Compd., 721 (2017), pp. 531-537

[19] Z. Huang, M. Yi, H. Gao, Z. Zhang, Y. Mao Enhancing single red band upconversion luminescence of KMnF3: Yb 3+/Er 3+ nanocrystals by Mg 2+ doping J. Alloy. Compd., 694 (2017), pp. 241-245

[20] S. Shi, L.-D. Sun, Y.-X. Xue, H. Dong, K. Wu, S.-C. Guo, C.-H. Yan Scalable direct writing of lanthanide-doped KMnF3 perovskite nanowires into aligned arrays with polarized up-conversion emission Nano Lett., 18 (5) (2018), pp. 2964-2969

[21] B. Zhou, B. Shi, D. Jin, X. Liu Controlling upconversion nanocrystals for emerging applications Nat. Nanotechnol., 10 (11) (2015), p. 924

[22] G. Murtaza, et al. Structural, chemical bonding, electronic and magnetic properties of KMF3 (M= Mn, Fe, Co, Ni) compounds Comput. Mater. Sci., 85 (2014), pp. 402-408

[23] A. Guerrero, et al. Interfacial degradation of planar lead halide perovskite solar cells ACS Nano, 10 (1) (2015), pp. 218-224

[24] C. Li, et al. Formability of ABX3 (X= F, Cl, Br, I) halide perovskites Acta Crystallogr. Sect. B: Struct. Sci., 64 (6) (2008), pp. 702-707

[25] S.R. Pering, et al. Azetidinium lead iodide for perovskite solar cells J. Mater. Chem. A, 5 (39) (2017), pp. 20658-20665 CrossRefView Record in ScopusGoogle Scholar

[28] H.S. Kim, S.H. Im, N.G. Park Organolead halide perovskite: new horizons in solar cell research J. Phys. Chem. C, 118 (11) (2014), pp. 5615-5625

[29] A. Kaltzoglou, et al. Trimethylsulfonium lead triiodide: an air-stable hybrid halide perovskite Inorg. Chem., 56 (11) (2017), pp. 6302-6309

[30] A. Sánchez-Coronilla, et al. Hybrid perovskite, CH3NH3PbI3, for solar applications: an experimental and theoretical analysis of substitution in A and B sites J. Nanomater. (2017)

[31] W. Wang, et al. Research progress of perovskite materials in photocatalysis-and photovoltaics-related energy conversion and environmental treatment Chem. Soc. Rev., 44 (15) (2015), pp. 5371-5408

[33] Johannes M. Richter, et al. Enhancing photoluminescence yields in lead halide perovskites by photon recycling and light out-coupling Nat. Commun., 7 (2016), p. 13941

[34] Dong Hoe Kim, et al. 300% Enhancement of carrier mobility in uniaxial-oriented perovskite films formed by topotactic-oriented attachment Adv. Mater., 29 (2017), p. 23

[35] Carlito S. Ponseca Jr, et al. Organometal halide perovskite solar cell materials rationalized: ultrafast charge generation, high and microsecond-long balanced mobilities, and slow recombination J. Am. Chem. Soc., 136.14 (2014), pp. 5189-5192

[36] Guichuan Xing, et al. Long-range balanced electron-and hole-transport lengths in organic-inorganic CH3NH3PbI3 Science, 342.6156 (2013), pp. 344-347

[37] Eline M. Hutter, et al. Charge carriers in planar and meso-structured organic–inorganic perovskites: mobilities, lifetimes, and concentrations of trap states J. Phys. Chem. Lett., 6.15 (2015), pp. 3082-3090

[38] H.S. Kim, J.Y. Seo, N.G. Park Material and device stability in perovskite solar cells ChemSusChem, 9 (18) (2016), pp. 2528-2540

Chapter 7 Magnetic-field-induced energy bandgap reduction of perovskite KMnF₃

Author contributions: Ryan T. Wang proposed the idea and conducted the experiments. Alex F Xu, Lory W Yang and Jason Y Chen assisted the experiment. Dr. Adrian Kitai helped the PVD experiments. Dr. Gu Xu provided overall supervision and the funding. This chapter is published in Journal of Materials Chemistry C, 2020.

Broad impact may be anticipated when an energy bandgap is varied substantially by a small change of the physical environment. Such possibility has now been discovered by the example of perovskite structure of $KMnF_3$ in this paper, where the photoluminescence, X-ray diffraction, scanning electron microscope and conductivity measurements were conducted, and the bandgap reduced up to 20% when a small magnet was placed beneath the substrate. It was also found that the electrical conductivity increased in the meantime by more than 15 folds under the 0.6 Tesla field strength. Such reduction in perovskite bandgap and enhancement in the transport properties were also observed by us in other structures, such as $CH_3NH_3PbI_3$ and $CsPbBr_3$. These discoveries are expected to improve device performance and accelerate the commercialization.

Introduction

The ability to control bandgap is critical for many semiconductor applications yet challenging in materials science and engineering, in particular in inorganic semiconductors, due to their wide applications in almost every part of our life, such as integrated circuits [7], light emitting devices [8] and photovoltaics [9,10], where the performance can be enhanced greatly by adjusting the bandgap energy. One such challenge comes from perovskite structures, which have been actively studied recently for solar cell applications [11], where the energy efficiency is largely influenced by their bandgap, such as $CsPbI_3$ and $CsPbBr_3$ [12,13], originally introduced to remove the moisture instability of organic perovskites. However, the energy efficiency of these

inorganic perovskites is much lower than the organic counterpart, due to their high bandgaps at room temperature, which calls for an answer to the challenge of adjusting the bandgap of existing semiconducting perovskites in general.

Although a number of "bandgap engineering" methods have been proposed for perovskites, such as replacing the A, B and X elements, for example, $RbPbI_3$ [14], $KPbI_3$ [15], and $CsPbBr_3$ [16], none offers a reduced bandgap to the needed level thus far. On the other hand, lowering bandgap through dopants, such as $Rb/MAPbI_3$ [17], $FA_xMA_{1-x}PbI_3$ [18], $FASn/PbI_3$ [19], often results in the compromise of other materials properties, such as chemical stability, equally critical to the practical applications.

It is therefore the purpose of the current letter, to search for the bandgap alteration without compromising other properties. Transition metal elements were chosen here due to their unique electromagnetic properties contributed by the 3d orbital structure, which was overlooked before. We unexpectedly discovered that, under the presence of a modest magnetic field strength of 0.6T, $KMnF_3$ perovskite exhibits both bandgap reduction from 1.77eV to 1.47eV as well as electrical conductivity enhancement by a factor of 15. Similar but less dramatic results were also obtained in other perovskites, such as $MAPbI_3$ and $CsPbBr_3$. These observations seem to be contradictory to the usual understanding of electron orbitals affected by magnetic field described by Landau levels, where the bandgap change is negligible at room temperature [2]. Neither could

it be attributed to the electromagnetic interactions of ions, formulated by Maxwell's equations and Lorentz formula [3], where the magnetic field effect is ignorable, as confirmed by the experimental results of the crystal growth under magnetic fields [3,20]. Although some have investigated the possibility of modifying the bandgap energy of metal and ferromagnets by magnetic field, such as the modulation of the Aharonov–Bohm phase by an axial magnetic field which changes the electron wavefunction by an electromagnetic potential [4], multiwall nanotube tuned by 33T magnetic field [5], and Stoner model for the ferromagnetic materials in which the influence on band structure depends on the magnetic polarization [6], little effect has been demonstrated. Therefore, our discoveries open a new channel, not only of bandgap energy tuning in particular, but also of nanostructure tailoring in general.

Experimental

$CsPbBr_3$ (99.999%), N, N-Dimethylformamide (>99%), CH_3NH_3I (>99.98%, anhydrous) and PbI_2 (>99.98%) were bought from Xi'an Polymer Light Technology Corp. KF (ACS reagent, > = 99.0%), $ZnCl_2$ (99.999%), and $MnCl_2$ (beads, 98%) were bought from Sigma-Aldrich. $KMnF_3$ perovskite was discovered using tolerance factor and octahedral factor criteria [21]. It possesses both reduced bandgap and great stability [22]. $KMnF_3$ and $MAPbI_3$ were synthesised using the method described in reference [22–24]. $MnCl_2$ (1g) was ground into fine powders and then dissolved in DI water (50ml). Subsequently saturated KF water solution (5ml) was added into the

MnCl$_2$ solution, pink precipitate of KMnF$_3$ formed immediately. After 12 h of stirring, the precipitate was separated from the solution by suction filtration. The collected precipitate was washed next by 95% ethanol and dried in an oven at 60 °C for half an hour. ZnCl$_2$ (1g) was dissolved in DI water (50ml). Subsequently, saturated KF water solution (5ml) was added into the solution, white precipitate of KZnF$_3$ formed immediately. After 6 h of stirring, the precipitate was separated from the solution by suction filtration. Next, the collected precipitate was washed by 95% ethanol and dried in an oven at 60 °C for half an hour.

A uniform KMnF$_3$ thin film was made through PVD sputtering method. A radio frequency (RF) method was adopted. Ar was used as carrier gas, and the deposition process was done in 10 mTorr condition. The thin film was deposited on Fluorine-doped-Tin-Oxide glass substrate (composition: SiO$_2$/F; film thickness: 500 nm; purchased from Huanan-Xiangcheng Tech Ltd). The KMnF$_3$ thin film has a thickness of 300nm, which was measured by KLA-Tencor D-100 Alphastep Profilometer. Such a thickness would not affect the bandgap and conductivity measurements. Based on the trials of the KMnF$_3$ film made by drop-casting (several microns in thickness), which showed almost the same results compared with the thin film; therefore, no difference between thin film and the bulk KMnF$_3$ was expected.

Powder XRD was conducted with a Bruker D8 DISCOVER diffractometer; measurements were taken in the 2θ range of 10 to 76°. Small magnetic cube was placed beneath the sample film when conducting the XRD measurements to investigate the

influence of magnetic field on the crystal structure. SEM was done by FEI Magellan 400 XHRSEM. All diagrams were drawn in Origin 9.0. Magnetic field was provided by Magnets Block Cube Rare Earth Neodymium Magnet N52/N42/N42SH (1cm*1cm*1cm in size), and the strength of magnetic field was measured by SJ200 Gauss Meter (shown in **Figure S1&S2**). Photoluminescence (PL) measurements of $CsPbBr_3$, $MAPbI_3$, $KMnF_3$ was conducted before and after a magnetic field was applied. The photoluminescence experiment was conducted by a tunable Ar-ion laser from Melles Griot (35LAP431208) at a power of 130 mW with a repetition rate of 50 Hz. The bandgap of $KZnF_3$ was measured by the Cary 5000 UV–vis–NIR Spectrophotometer, from 800 nm to 300 nm. The conductivity and carrier mobility of perovskites were measured through I-V curve measurements on CMS100 electrochemical workstation (purchased from The Illinois Department of Central Management Services), as reported in the literature [25,26].

Results & Discussion

Under the presence of external magnetic field of 0.6 Tesla, a more favorable bandgap energy for solar cell applications has been obtained from $KMnF_3$, as shown in **Figure 7. 1(a)**. The photoluminescence spectrum of $KMnF_3$ peaks at 700 nm in the absence of the magnetic field; while this peak redshifts to 850 nm gradually with the increasing magnetic field, which corresponds to 0.3 eV (17%) change in bandgap. Moreover, the transport properties also demonstrated a significant increase under the magnetic field, as can be confirmed in **Figure 7. 1(b) & (c)**, where the electrical

conductivity increased more than 15 times at 0.6T magnetic field. This enhancement on the conductivity is apparently attributed to the carrier mobility, as can be confirmed in **Figure 7. 1(d)**, whose value was raised by more than 20 times at 0.6T magnetic field, which accelerated the motion of 3d electron in Mn. Thus, it is clear that $KMnF_3$ shows a strong response to magnetic field, which not only lowers the bandgap, but also raises the electrical conductivity. From the results of bandgap reduction under magnetic field, there seems to exist a positive trend with increasing magnetic field strength, which is definitely worth further investigation. An SEM measurement has also been conducted to observe the morphology of the sputtered $KMnF_3$ film, which indicated a nanosized grain with clear grain boundary area, as shown in Figure 7. 2.
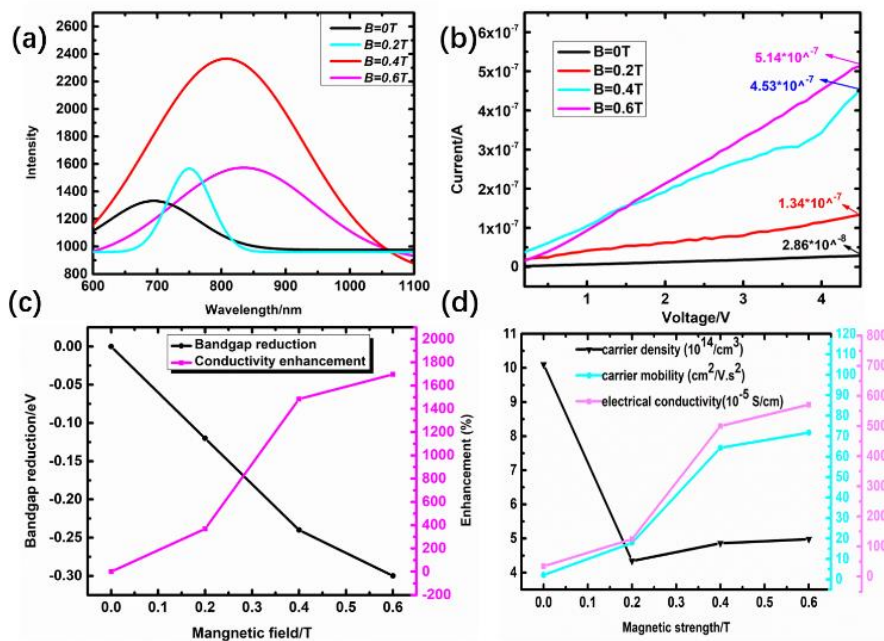
Figure 7. 1. (a)PL measurements of $KMnF_3$ under various magnetic fields. Information about the magnetic strength and PL measurement equipment is given in support

information **Figure S7. 1**; (b) electrical conductivity measurements of $KMnF_3$ thin film under various magnetic fields; (c) bandgap reduction and conductivity enhancement of $KMnF_3$ under various magnetic fields; (d) carrier density/mobility and electrical conductivity vs magnetic field.
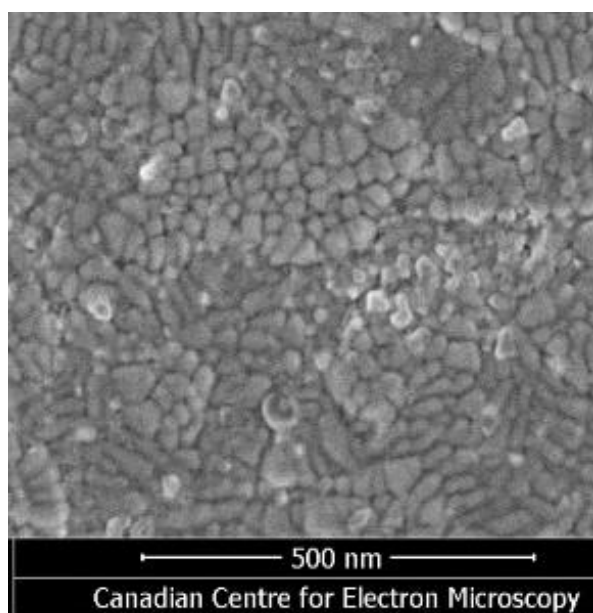
Figure 7. 2. Nanosized grain of $KMnF_3$ film deposited by sputtering.

To confirm our finding, Cyclic Voltammetry (CV) has been conducted to determine the bandgap reduction. As shown in Figure 7. 3, the bandgap of $KMnF_3$ extracted from the figure was around 1eV when no magnetic field was adopted [28]; while such bandgap reduced by 0.35eV under a 0.6T magnetic field, as opposed to the optical data of 0.3eV. The difference is attributed to the fact that bandgap measured by CV is normally smaller than optical data, as reported before [28–30], which is usually affected by the electrolyte.
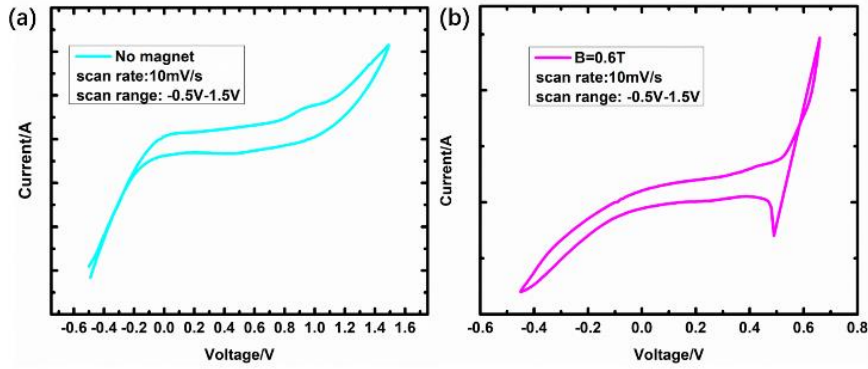
Figure 7. 3. CV measurements on the bandgap reduction of $KMnF_3$ under magnetic field (extrapolated by Origin 9.0).

It is apparent from the results above, applying magnetic field to the perovskite reduces its bandgap, and enhances its transport properties by more than 15 folds, which is in sharp contrast to the literature of attempting to raise the performance by magnetic field during the film formation, but resulted in only 1% improvement [20]. Such huge difference may be attributed to the presence of Mn in our case, which is a transition metal with unpaired 3d electron. To further verify this, other non-Mn perovskite structures have been investigated, including $MAPbI_3$, $CsPbBr_3$ and $KZnF_3$. The property of $KZnF_3$ is unique, as Zn element is also a transition metal that has a fully filled 3d shell which forms sharp contrast with $KMnF_3$. The bandgap of $KZnF_3$ was measured by UV-vis absorption spectroscopy, as shown in **Figure 7. 4(a)&(b)**, which shows almost no bandgap reduction at all magnetic fields, and the bandgap remained the same at around 3.0 eV in both measurements. This can be attributed to the fully filled 3d shell of Zn, which has little magnetic response; while Mn has a half filled 3d shell, the five 3d electrons are all aligned in the same direction, which produces a strong

magnetic response. An XRD and SEM measurements were also conducted to detect the structure of KZnF3, which showed a cubic structure with Pm3m space group, as demonstrated in **Figure 7. 4(c)&(d)**.
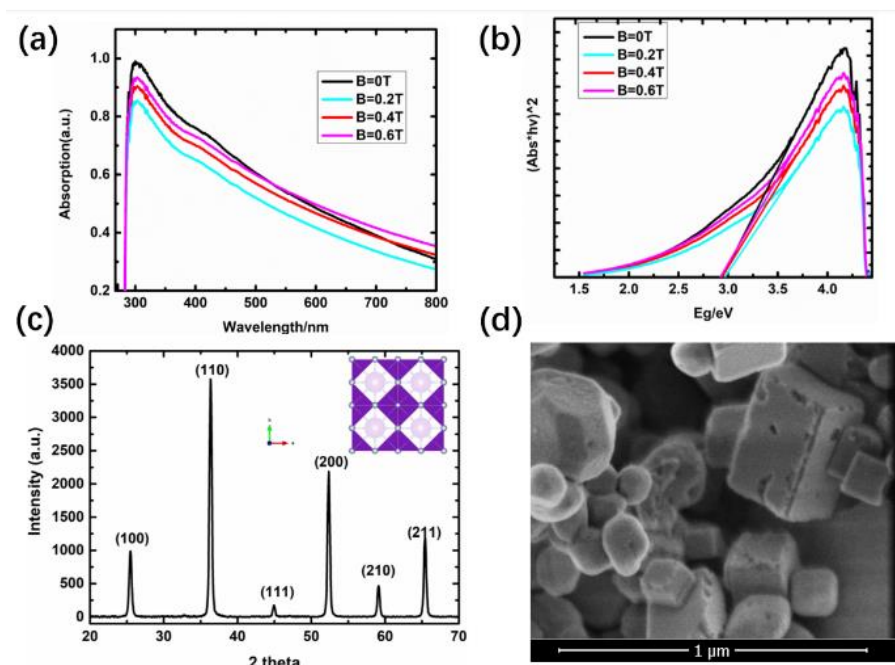
Figure 7. 4. (a)UV-vis absorption of KZnF$_3$ at various magnetic field; (b)corresponding Eg vs (abs*hv)^2 plot and the Tauc plot. Absorption measurement was applied due to the large bandgap of KZnF$_3$ exceeded the measurement range of PL equipment; (c) the XRD pattern and crystal structure of KZnF$_3$; (d) the morphology of KZnF$_3$ film under SEM.

On the other hand, MAPbI$_3$ and CsPbBr$_3$ exhibited a similar trend as KMnF$_3$ under magnetic field, but not as large in terms of the bandgap reduction and transport properties enhancement. The PL experimental results are shown in **Figure 7. 5&7. 6 (a)&(b)**, where the bandgap of MAPbI$_3$ and CsPbBr$_3$ is reduced by 0.07 eV and 0.08

eV at 0.6T magnetic field, respectively, much smaller than that of the KMnF$_3$. Neither has the transport properties been increased significantly; the largest raise in transport properties were only 130% for MAPbI$_3$ and 120% for CsPbBr$_3$, as proved in **Figure 7. 5&7. 6 (c)&(d)**.
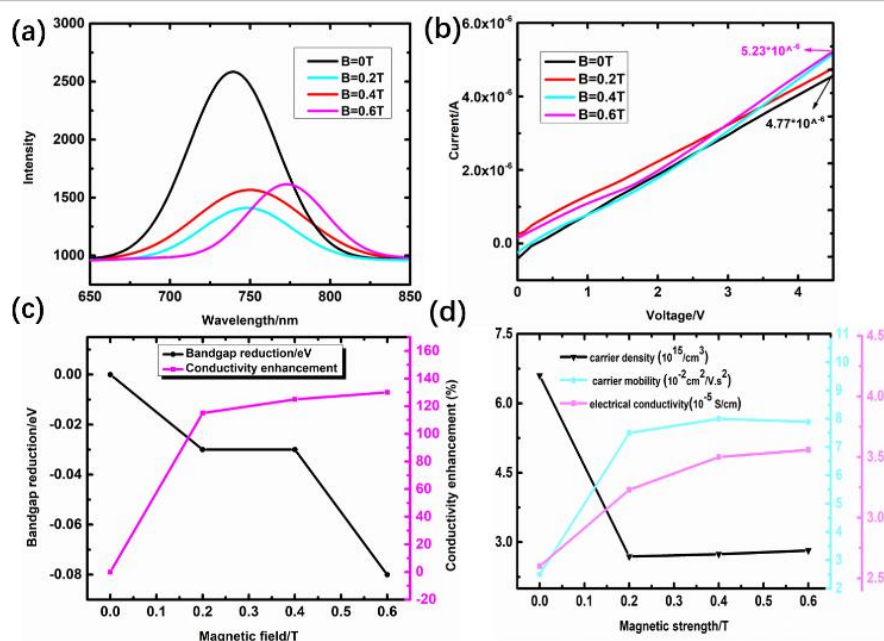
Figure 7. 5. (a)PL measurements of MAPbI$_3$ under various magnetic fields; (b) electrical conductivity measurements of MAPbI$_3$ thin film under various magnetic fields; (c) bandgap reduction and conductivity enhancement of MAPbI$_3$ under various magnetic fields; (d) carrier density/mobility and electrical conductivity vs magnetic field.
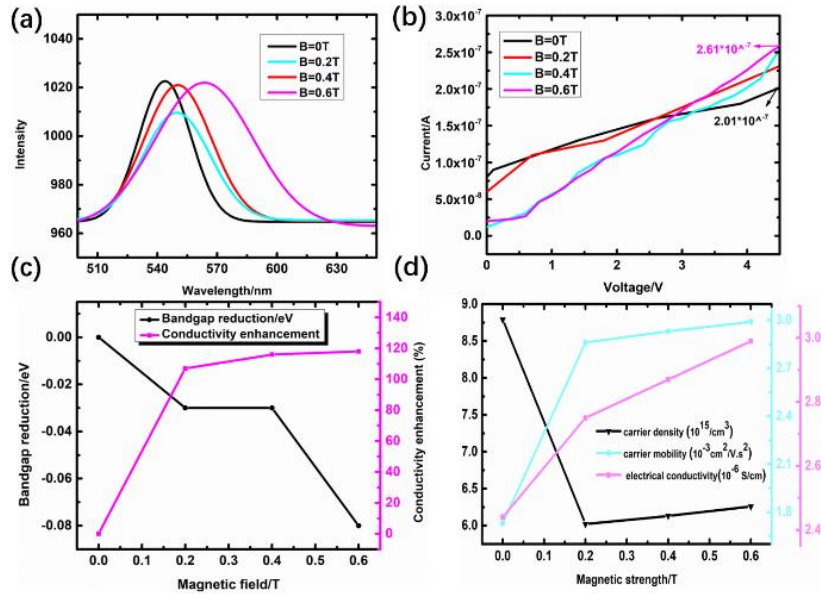
Figure 7. 6. (a)PL measurements of CsPbBr$_3$ under various magnetic fields; (b) electrical conductivity measurements of CsPbBr$_3$ thin film under various magnetic fields; (c) bandgap reduction and conductivity enhancement of CsPbBr$_3$ under various magnetic fields; (d) carrier density/mobility and electrical conductivity vs magnetic field.

Such surprising results may only be attributed to the change in electron orbitals instead of that in the lattice parameter under the magnetic field, as confirmed by **Figure 7. 7**. The diffraction patterns of the materials with and without magnetic field are identical, which proves that the lattice parameters remained the same in all measurements.
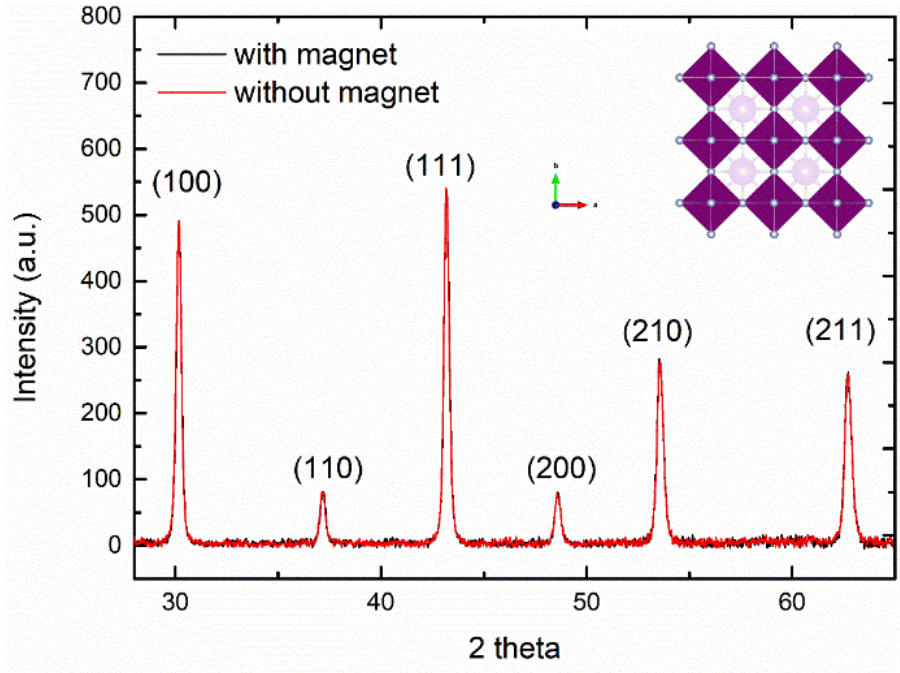
Figure 7. 7. XRD experiments of KMnF$_3$ with and without the application of magnetic field.

Obviously, much better results have been obtained from our experiments, compared with similar attempts of others, where the conclusions were often based on predictions and bandgap reduction was very small (0.07 eV at 33 T). Although magnetic field was also applied before, the reduction was confined to some specific materials, including graphene based nanotubes [4,5] and ferromagnets [6]. In our case, however, bandgap reduction was observed at several different types of perovskites with the Mn-containing structure shows the largest reduction. The influence of Mn comes from its contribution to the band structure formation of KMnF$_3$. As can be found in the literature, the valence band maximum (VBM) of KMnF$_3$ is attributed to the Mn 3d-eg orbitals, and the conduction band minimum (CBM) is attributed to the Mn 3d-t2g orbitals [31–

121

33]. When the magnetic field is applied, the bandgap is changed because the spin-orbit coupling between the spin of the 3d electrons and the VBM/CBM orbitals is influenced by the alteration in the 3d electron spin by the magnetic field. This change in the spin-orbit coupling is large, because all the 3d electrons in Mn are unpaired and align in the same direction, which react strongly to the external magnetic field. And the unpaired 3d electron motion can be accelerated by the external magnetic field, which in turn increases the electrical conductivity.

On the other hand, the VBM of $KZnF_3$ is contributed by the interaction between Zn-3d and F-2p orbitals, and the CBM is contributed by the interaction between Zn 4s and F 2p orbitals [34]. Although 3d orbitals are involved in the band structure formation, the 3d shell of Zn is fully filled. Therefore, all the 3d electrons are paired, and thus their magnetic responses are cancelled out. As for $MAPbI_3$, its VBM consists of the hybridizations of the atomic 5p orbitals of iodine and 6s orbitals of lead, and the CBM is mainly formed of empty 6p orbitals of lead [35,36]. There are no d orbitals involved in its band structure. Although no magnetic response is expected theoretically, the heavy nature of the lead and iodine ions results in significant spin–orbital coupling which may exhibit a certain magnetic field response [35,36], but certainly noncomparable to that of Mn-containing perovskite.

Conclusions

In conclusion, a surprising bandgap tuning method has been found. By the

presence of a modest magnetic field of only 0.6T, the bandgap changes up to 0.3 eV and transport properties increase by more than 15 folds, presumably through the spin-orbit coupling of the perovskite structure. The method is effective to most of the perovskites, especially to those perovskites containing transition metal elements with unpaired d electrons. In addition, it has also been discovered that the carrier mobility of perovskite semiconductors can be enhanced by magnetic field. Those discoveries are expected to offer immediate impact on the rapid development of perovskite solar cells, as they open a new channel of tuning the bandgap and enhancing transport properties of perovskite structure in general.

Notes and References

1   D. Kang, A. Anirban and A. S. Helmy, *Opt. Express*, 2016, **24**, 15160.

2   C. Wang, H. Dong, L. Jiang and W. Hu, *Chem. Soc. Rev.*, 2018, **47**, 422–500.

3   E. G. Tai, R. T. Wang, J. Y. Chen and G. Xu, *Crystals*, 2019, **9**, 83.

4   A. F. Xu, R. T. Wang, L. W. Yang, N. Liu, Q. Chen, R. Lapierre, N. Isik Goktas and G. Xu, *J. Mater. Chem. C*, 2019, **7**, 11104–11108.

5   A. F. Xu, R. T. Wang, L. W. Yang, V. Jarvis, J. F. Britten and G. Xu, *Chem. Commun.*, 2019, **55**, 3251–3253.

6   X. Chang, W. Li, L. Zhu, H. Liu, H. Geng, S. Xiang, J. Liu and H. Chen, *ACS Appl. Mater. Interfaces*, 2016, **8**, 33649–33655.

7   J. Liang, C. Wang, Y. Wang, Z. Xu, Z. Lu, Y. Ma, H. Zhu, Y. Hu, C. Xiao and X. Yi, *J. Am. Chem. Soc.*, 2016, **138**, 15829–15832.

8   M. H. Jung, S. H. Rhim and D. Moon, *Sol. Energy Mater. Sol. Cells*, 2017, **172**, 44–54.

9   D. N. Dirin, S. Dreyfuss, M. I. Bodnarchuk, G. Nedelcu, P. Papagiorgis, G. Itskos and M. V. Kovalenko, *J. Am. Chem. Soc.*, 2014, **136**, 6550–6553.

10   M. Kulbak, D. Cahen and G. Hodes, *J. Phys. Chem. Lett.*, 2015, **6**, 2452–2456.

11   X. Bai, X. Zou, J. Zhu, Y. Pei, Y. Yang, W. Jin and D. Chen, *Mater. Lett.*, 2018, **211**, 328–330.

12   J. Chang, H. Chen, H. Yuan, B. Wang and X. Chen, *Phys. Chem. Chem. Phys.*, 2018, **20**, 941–950.

13   S. Shao, J. Liu, G. Portale, H. H. Fang, G. R. Blake, G. H. ten Brink, L. J. A. Koster and M. A. Loi, *Adv. Energy Mater.*, 2018, **8**, 1702019.

14   G. Gulyamov, U. I. Erkaboev, G. N. Majidova, M. O. Qosimova and A. B. Davlatov, *Open J. Appl. Sci.*, 2015, **05**, 771–775.

15   D. J. Griffiths and A. Reeves, *Introd. to Electrodyn. 3rd ed., Prentice Hall, Up. Saddle River, New Jersey*, 2005, **301**, 574–574.

16   H. Wang, J. Lei, F. Gao, Z. Yang, D. Yang, J. Jiang, J. Li, X. Hu, X. Ren, B. Liu, J. Liu, H. Lei, Z. Liu and S. Liu, *ACS Appl. Mater. Interfaces*, 2017, **9**, 21756–21762.

17   H. Ajiki and T. Ando, *J. Phys. Soc. Japan*, 1993, **62**, 1255–1266.

18   G. Fedorov, P. Barbara, D. Smirnov, D. Jiḿnez and S. Roche, *Appl. Phys. Lett.*, 2010, **96**, 132101.

19   C. M. Teodorescu and G. A. Lungu, *J. Optoelectron. Adv. Mater.*, 2008, **10**,

3058–3068.

20   C. Li, X. Lu, W. Ding, L. Feng, Y. Gao and Z. Guo, *Acta Crystallogr. Sect. B Struct. Sci.*, 2008, **64**, 702–707.

21   R. T. Wang, E. G. Tai, J. Y. Chen, G. Xu, R. LaPierre, N. I. Goktas and N. Hu, *Ceram. Int.*, 2019, **45**, 64–68.

22   U. G. Jong, C. J. Yu, G. C. Ri, A. P. McMahon, N. M. Harrison, P. R. F. Barnes and A. Walsh, *J. Mater. Chem. A*, 2018, **6**, 1067–1074.

23   R. T. Wang, A. F. Xu, J. Y. Chen, L. W. Yang, G. Xu, V. Jarvis and J. F. Britten, *J. Phys. Chem. Lett.*, 2019, **10**, 7245–7250.

24   D. Yu, C. Wang, B. L. Wehrenberg and P. Guyot-Sionnest, *Phys. Rev. Lett.*, 2004, **92**, 216802.

25   E. L. Unger, E. T. Hoke, C. D. Bailie, W. H. Nguyen, A. R. Bowring, T. Heumüller, M. G. Christoforo and M. D. McGehee, *Energy Environ. Sci.*, 2014, **7**, 3690–3698.

26   J. M. Richter, M. Abdi-Jalebi, A. Sadhanala, M. Tabachnyk, J. P. H. Rivett, L. M. Pazos-Outón, K. C. Gödel, M. Price, F. Deschler and R. H. Friend, *Nat. Commun.*, 2016, **7**, 1–8.

27   M. L. Gross and M. A. Hickner, *Electrochem. Solid-State Lett.*, 2010, **13**, K5–K7.

28   S. N. Inamdar, P. P. Ingole and S. K. Haram, *ChemPhysChem*, 2008, **9**, 2574–2579.

29   D. Baran, A. Balan, S. Celebi, B. Meana Esteban, H. Neugebauer, N. S. Sariciftci

and L. Toppare, *Chem. Mater.*, 2010, **22**, 2978–2987.

30   S. Berri, *J. Sci. Adv. Mater. Devices*, 2016, **1**, 286–289.

31   Hayatullah, G. Murtaza, R. Khenata, S. Muhammad, A. H. Reshak, K. M. Wong, S. Bin Omran and Z. A. Alahmed, *Comput. Mater. Sci.*, 2014, **85**, 402–408.

32   S. L. Wang, W. L. Li, G. F. Wang, D. Y. Dong, J. J. Shi, X. Y. Li, P. G. Li and W. H. Tang, *Powder Diffr.*, 2013, **28**, S3–S6.

33   T. Hu, H. Lin, F. Lin, Y. Gao, Y. Cheng, J. Xu and Y. Wang, *J. Mater. Chem. C*, 2018, **6**, 10845–10854.

34   Y. S. Jung, K. Hwang, Y. J. Heo, J. E. Kim, D. Vak and D. Y. Kim, *Adv. Opt. Mater.*, 2018, 6.

35   X. Qi, Y. Zhang, Q. Ou, S. T. Ha, C. W. Qiu, H. Zhang, Y. B. Cheng, Q. Xiong and Q. Bao, *Small*, 2018, 14, 1800682.

Chapter 8 Conclusions

This thesis aims to advance the understanding of the degradation, performance, structural stability, and phase transition in both organic and inorganic perovskites. In the first stage, we investigated the degradation mechanism of the organic perovskites, which was attributed to the H bonds. The perovskite structure was reconstructed when annealed at 90°C, providing an effective strategy to fight against moisture degradation. Following this work, we developed a structural manipulation method, which enabled us to artificially design the materials property. Based on the discovery, the hydrate of FAPbI$_3$ was synthesized, which showed a reduced bandgap of 1.6eV. The thermodynamic calculation showed that the new phase has a lower Gibbs free energy of 0.12eV compared to the δ phase. Thus, the new phase will remain stable in the air, as can be confirmed in the experiment work, where the device lifetime was enhanced from 2 days to more than 20 days. In the simulation work, the water diffusion process was modelled in the perovskite structure. It was found that the diffusion was initiated by the surface imperfection, where the diffusion activation energy can be compensated by the surface energy. The evaporation of water was smiluated by the back diffusion, which demonstrated a non-linear diffusional profile.

In the next step, a fresh inorganic structure was proposed by thinking beyond the psychological inertia. The stable inorganics of comparable bandgap to the organic counterparts have been reported. KMnF$_3$ exhibited excellent moisture and thermal stability, and showed a suitable bandgap value of 1.7eV, which not only leads to good

transport property, but also opens an avenue in magnetic research, which was studied in the following stage. The unique properties of $KMnF_3$ were attributed to the magnetic behaviour of the Mn element. To verify this hypothesis, extensive experiments were conducted under low to moderate magnetic fields. The bandgap of $KMnF_3$ reduced up to 20% when a small magnet was placed beneath the substrate. In addition, the electrical conductivity increased in the meantime by more than 15 folds under the 0.6 Tesla field strength. A similar effect was also observed in other structures, such as $MAPbI_3$ and $CsPbBr_3$, providing effective strategies to enhance the device performance and accelerate the commercialization.

Overall, our work attracted much attention in the perovskite community. The low bandgap inorganic perovskite was widely recognized by other literatures (Physical Review B, 101(6), p.064401.; Ceramics International, 45(7), pp.8669-8676.). In addition, the degradation mechanism of the organic perovskite provided immediate help to the community (Advanced Energy Materials 10, no. 22 (2020): 2000691.; Advanced Science. 2020 May;7(10):1903250.; Journal of Power Sources, 454, p.227938.; Journal of Energy Chemistry, 48, pp.293-298.). Hopefully, our discoveries will attract more attention in this field in the future.

Appendix: Supporting materials

Supporting information for Chapter 2

Reversing Organic-inorganic Hybrid Perovskite Degradation in Water via pH and Hydrogen Bonds

Ryan Taoran Wang[a], Alex Fan Xu[a], Jason Yuanzhe Chen[a], Lory Wenjuan Yang[a], Gu Xu*[a], Victoria Jarvis[b], and James F. Britten[b]

^a Department of Materials Science and Engineering, McMaster University, 1280 Main St. W, Hamilton, ON, L8S 4L8, Canada

^b MAX Diffraction Facility, Department of Chemistry, McMaster University, 1280 Main St. W, Hamilton, ON, L8S 4M1, Canada

E-mail: xugu@mcmaster.ca

Phone: +1 905-525-9140 ext. 27341

Lists of the contents of material supplied

Figure S2. 1. (a)Schematic illustration of the in-situ XRD measurement chamber; (b) the actual picture of the in-situ XRD chamber.

Figure S2. 2. (a)Crystal structure of CH_3NH_3I; (b) calculated powder XRD pattern of CH_3NH_3I based on single crystal data.

Figure S2. 3. (a)Fibrous (spectrum 1) and cubic area (spectrum 2) chosen for EDS analysis; (b) EDS peaks for spectrum 1; (c) EDS peaks for spectrum 2; (d) weight percent distribution of elements in spectrum 1&2, carbon in spectrum 1 comes from the surface carbon coating instead of CH_3NH_3I as no nitrogen was detected (the EDS is useful as a qualitative analysis, but certainly not for a quantitative one, as its accuracy is limited [1] [2]).

Table S1. Crystal data and structure refinement for CH_3NH_3I.

Figure S2. 1. (a)Schematic illustration of the in-situ XRD measurement chamber; (b) the actual picture of the in-situ XRD chamber.

Figure S2. 2. (a)Crystal structure of CH₃NH₃I; (b) calculated powder XRD pattern of CH₃NH₃I based on single crystal data.

	Elements	Wt%
Spectrum 1	C	1.8
	N	0
	Pb	45.1
	I	53.1
Spectrum 2	C	6.7
	N	7.1
	Pb	36.1
	I	50.1

Figure S2. 3. (a)Fibrous (spectrum 1) and cubic area (spectrum 2) chosen for EDS analysis; (b) EDS peaks for spectrum 1; (c) EDS peaks for spectrum 2; (d) weight percent distribution of elements in spectrum 1&2, carbon in spectrum 1 comes from the surface carbon coating instead of CH₃NH₃I as no nitrogen was detected (the EDS is useful as a qualitative analysis, but certainly not for a quantitative one, as its accuracy is limited [1][2]).

Figure S2. 2. (a)Crystal structure of CH_3NH_3I; (b) calculated powder XRD pattern of CH_3NH_3I based on single crystal data.

	Elements	Wt%
Spectrum 1	C	1.8
	N	0
	Pb	45.1
	I	53.1
Spectrum 2	C	6.7
	N	7.1
	Pb	36.1
	I	50.1

Figure S2. 3. (a)Fibrous (spectrum 1) and cubic area (spectrum 2) chosen for EDS analysis; (b) EDS peaks for spectrum 1; (c) EDS peaks for spectrum 2; (d) weight percent distribution of elements in spectrum 1&2, carbon in spectrum 1 comes from the surface carbon coating instead of CH_3NH_3I as no nitrogen was detected (the EDS is useful as a qualitative analysis, but certainly not for a quantitative one, as its accuracy is limited [1][2]).

Table S. 1. Crystal data and structure refinement for CH_3NH_3I.

Compound	CH_3NH_3I
Empirical formula	CH_6NI
Weight	158.97g/mol
Temperature	295K
Wavelength	0.71073 Å
Crystal system	tetragonal
Space group	P4/nmm (No. 129)
Unit cell dimensions	a=b=5.124 Å; c=9.039 Å
Volume	237.3 $Å^3$
Z	2
Absorption coefficient	6.543/mm
Absorption (exp) Tmin, Tmax	0.4388, 0.7461
F(000)	144
Crystal size	0.29cm*0.284cm*0.088cm
θ range for data collection	2.253°-30.737°
index ranges	-7<h<7 -5<k<7 -13<l<11
Reflections collected	1917

Reference

[1] M. S. Adaramola, M. Agelin-Chaab, and S. S. Paul, Analysis of Hybrid Energy Systems for Application in Southern Ghana, Energy Convers. Manag. 88, 284 (2014).

[2] G. Gulyamov, U. I. Erkaboev, G. N. Majidova, M. O. Qosimova, and A. B. Davlatov, New Method of Determining the Landau Levels in Narrow-Gap Semiconductors, Open J. Appl. Sci. 05, 771 (2015).

Supporting information for Chapter 3

FAPbI$_3$ perovskite property maneuvered via atomic structure negotiation

Ryan Taoran Wang[a§]; Alex Fan Xu[a§]; Wuqi, Li[b]; Yuning, Li[b]; and Gu Xu[a*]

[a] Department of Materials Science and Engineering, McMaster University, 1280 Main St. W, Hamilton, ON, L8S

4L8, Canada

[b] Department of Chemical Engineering and Waterloo Institute for Nanotechnology (WIN), University of Waterloo,

200 University Avenue West, Waterloo, Ontario N2L 3G1, Canada

§ First author; * Corresponding author, E-mail: xugu@mcmaster.ca

Phone: +1 905-525-9140 ext. 27341

Materials

All the materials were used as received without any further purification, including SnO$_2$

(15% in H$_2$O colloidal dispersion, Alfa Aesar), ethanol (AR Beijing Chemical Works),

FAI (CH$_5$N$_2$I) (>99.98%, anhydrous Xi'an Polymer Light Technology Corp.), HBr (48

wt.% in water, Sigma-Aldrich), HI (57 wt.% in water, Sigma-Aldrich), PbO (99.999%,

Sigma-Aldrich), PbI$_2$ (99.999%, Sigma-Aldrich), chlorobenzene (99.9%, Sigma-

Aldrich), isopropanol (IPA, 99.99%, Sigma-Aldrich), N,N-dimethylformamide (DMF,

99.99%, Sigma-Aldrich), Dimethyl sulfoxide (DMSO, 99.9%, Sigma-Aldrich), Spiro-OMeTAD (Xi'an Polymer Light Technology Corp.), bis(trifluoromethane)sulfonimide lithium salt (99.95%, Aldrich), 4- tertbutylpyridine (99.9%, Sigma-Aldrich), and ITO substrates.

Film formation and device fabrication

The FTO substrate was sequentially washed by distilled water and ethanol in the ultrasonicator, with two times each. The SnO_2 colloidal solutions (15% in H_2O) were further diluted by H_2O to 2.67%. After 20 mins of UV–O_3 treatments, the diluted SnO_2 solutions were spin-coated at 3000 rpm for 30 s on FTO substrates and annealed on a hot plate at the displayed temperature of 150 °C for 30 min in ambient air. For the $FAPbI_3$ metal halide perovskite layer, two-step spin coating method was adopted following previous report. In detail, 30 μL of lead iodide solutions were first spin-coated at 2300 rpm for 30 s and annealed at 70 °C for 1 min. Next, 80 μL of FAI precursor solutions were spin coated at 2000 rpm for 30 s. The as fabricated films were annealed at 150 °C for 45 min in air. For the synthesis of the ε phase, the substrate was left in the humid environment of 80RH% for 7 days. The XRD measurement was conducted to confirm the formation of the ε phase. The SEM measurement should be conducted at this stage to investigate the film morphology. Next, 30 μL Spiro-OMeTAD solution doped with LiTFSI and tBP was deposited at 3000 rpm for 30 s. The hole transport material (HTM) solution was prepared by dissolving 60 mg spiro- OMeTAD, 30 μL 4-tert-butylpyridine and 35 μL Li-TFSI/acetonitrile (260 mg mL^{-1}) in 1mL

chlorobenzene. Finally, 100 nm Ag was thermally evaporated as counter electrode under a pressure of 5×10^{-5} Pa on top of the hole transport layer to form the metal contact.

Synthesis of ε, θ, and μ phases

$FAPbI_3$ monohydrate, dihydrate, and trihydrate were synthesized by adding water into the thin film of $FAPbI_3$ by the molar ratio of 1:1, 1:2, and 1:3 respectively. A uniform $FAPbI_3$ thin film was synthesised first by drop casting using syringe. The amount of $FAPbI_3$ contained in such thin film can be given by the multiplication of the volume and the concentration of $FAPbI_3$ solution. The amount of water to be transferred to the thin film could thus be determined. The micropipette was adopted to transfer the water. In the following step, single crystal needles of ε were synthesized via commonly adopted antisolvent vapor-assisted crystallization (AVC) method. Acetone as anti-solvent was added to the thin film of ε. After two weeks, the yellow needle-like single crystal of ε can be obtained. The single crystal needle was picked up under optical microscope and measured by Bruker APEX-II diffractometer at room temperature. The data was processed in APEX2 V2014.9.0, and structure solution and refinement were processed in SHELXT and SHELXL (Sheldrick, 2015).

Thermodynamic calculation

The transform diffraction is determined by the relative peak height of each phases. For $\delta \rightarrow \varepsilon$ transformation, the peak at 13.2° and 38.8° were adopted, which represented the

characteristic peak of ε and δ phases. The ratio of the 2 peak heights gives the transformation fraction, which should equal to exp(-ΔG/RT). The ΔG of (δ-ε) could thus be determined. Similarly, for $\varepsilon \rightarrow \theta$ transformation, the peak at 16.8° and 58.5° were adopted, which represented the characteristic peak of θ and ε phases. The ratio of the 2 peak heights gives the transformation fraction. For $\theta \rightarrow \mu$ transformation, the peak at 9.2° and 16.8° were adopted, which represented the characteristic peak of μ and θ phases. The ratio of the 2 peak heights gives the transformation fraction.
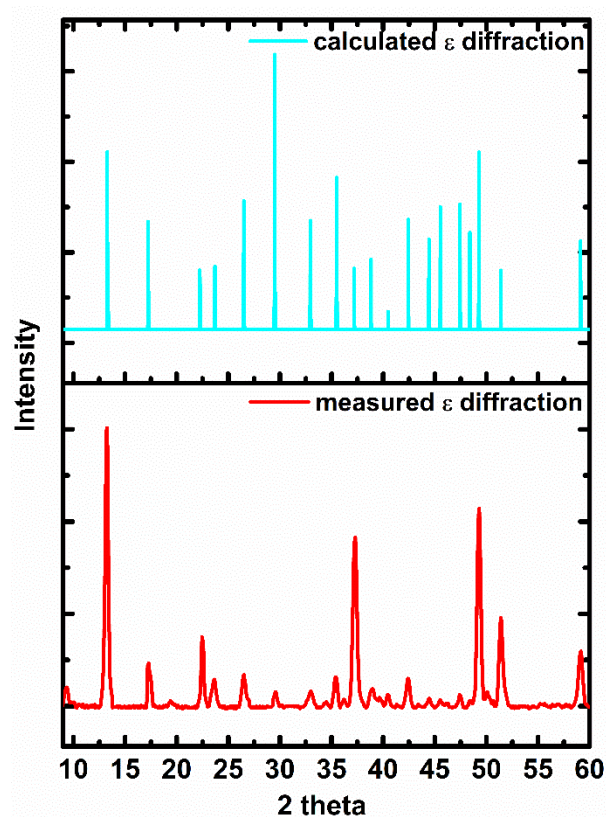
Figure S7. 1. The comparison of the measured and calculated XRD data of ε phase. The calculated data was extrapolated from the single crystal XRD measurement.

Supporting information for Chapter 5

Hysteresis and instability predicted in moisture degradation of perovskite solar cells

Kelvin J. Xu[a], Ryan T. Wang[b], Alex F. Xu[b], Jason Y. Chen[b] and Gu Xu[b*]

a Fu Foundation School of Engineering and Applied Science, Columbia University, New York, 10027, USA

b Department of Materials Science and Engineering, McMaster University, Hamilton, ON, L8S4L8, Canada

*corresponding author, E-mail: xugu@mcmaster.ca
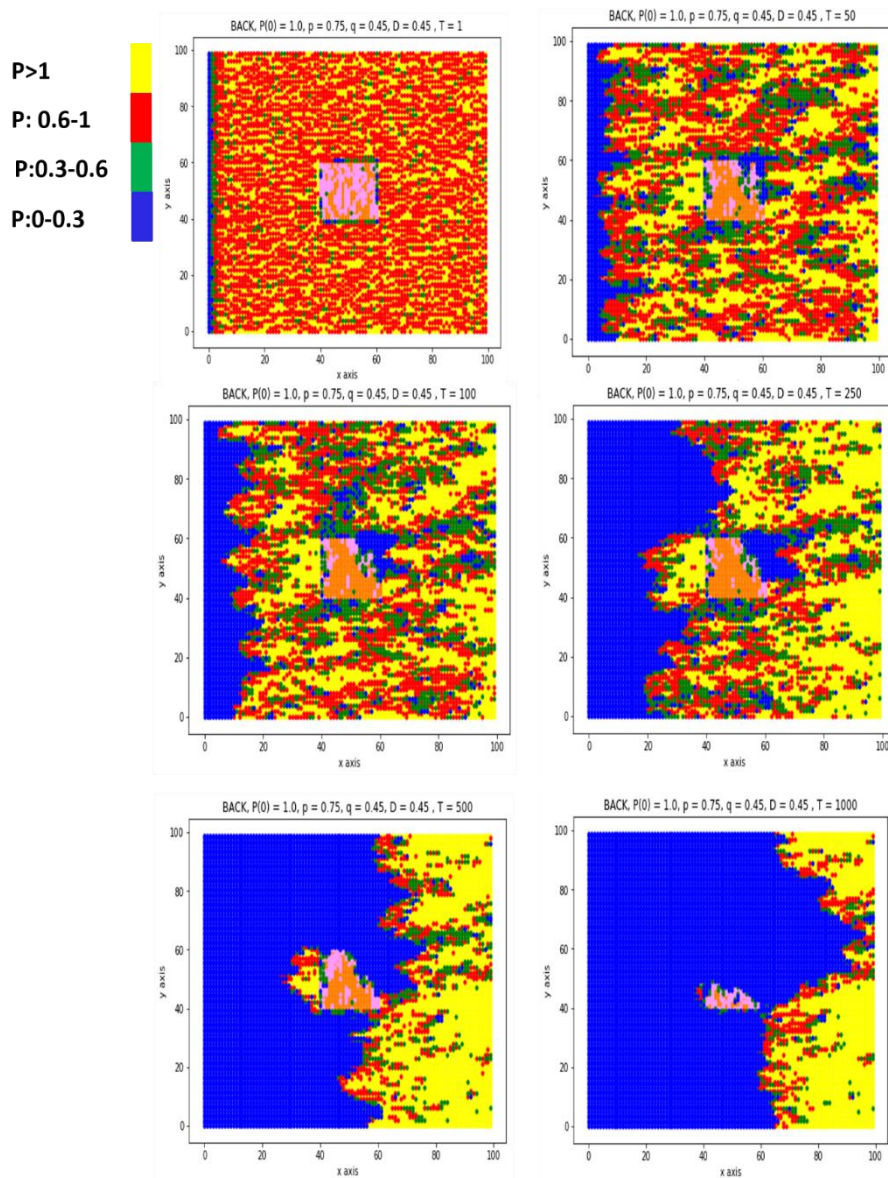
Figure S5. 1. Time-resolved image for Figure 3c: the possibility of water back diffusion has been simulated, when the left boundary of the lattice was set to zero, after the complete saturation of all the Ps (=1.0). Only the P value were updated throughout the time iteration to simulate the back diffusion. These diagrams showed the time-resolved water diffusion process. Eventually, it was discovered that the diffusion seems to be localized within some area, or even become trapped in the area far away from the

draining boundary.
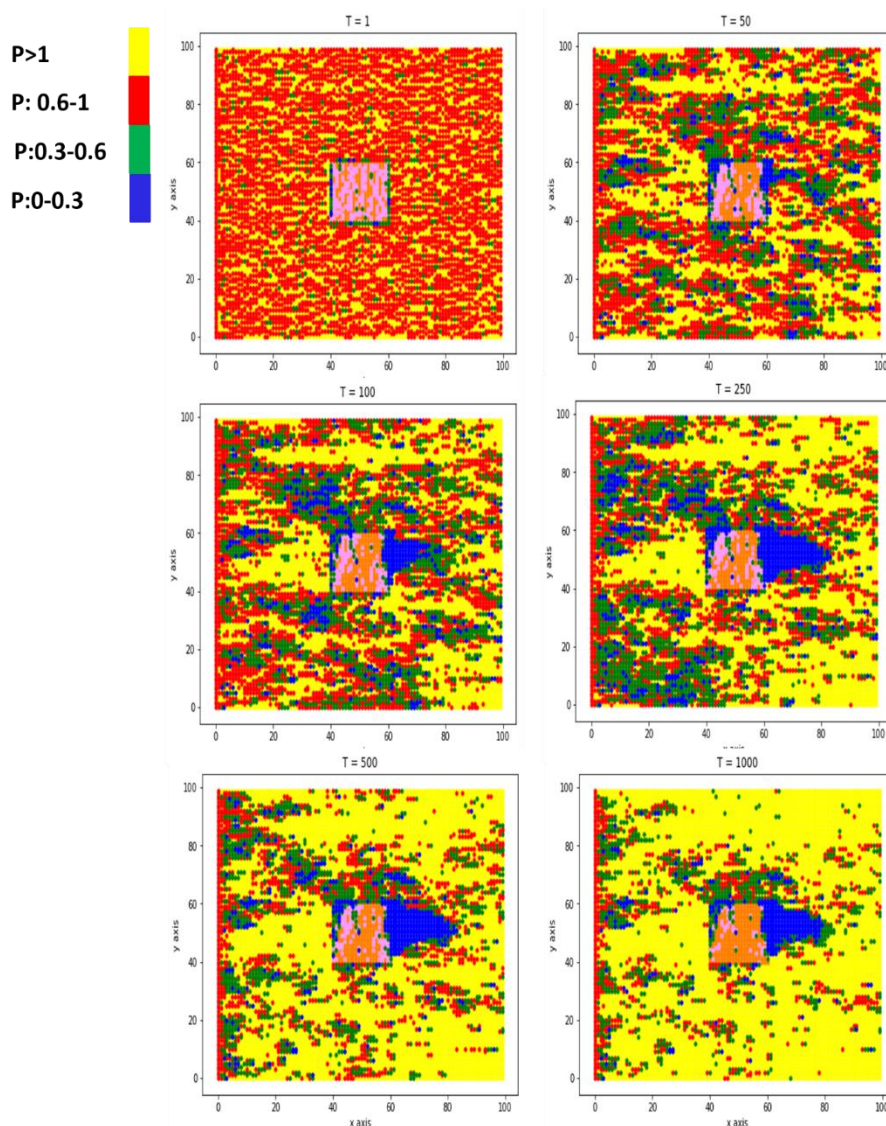
Figure S5. 2. Time-resolved image for Figure 4b: All the P values were initialized to 1, including the boundaries. All the W values were then assigned by either 0 or 1, to mimic the potential instabilities under the presence of 1D PbI_2 chains. These diagrams showed the time-resolved water diffusion process, which seemed to be frozen, should such imbalance be regulated towards a certain orientation.